Technische Universität München

Physik Department

MPQ

Two-Photon Gate and Creation of Optical Cat States using One Atom in a Cavity

Bastian Hacker

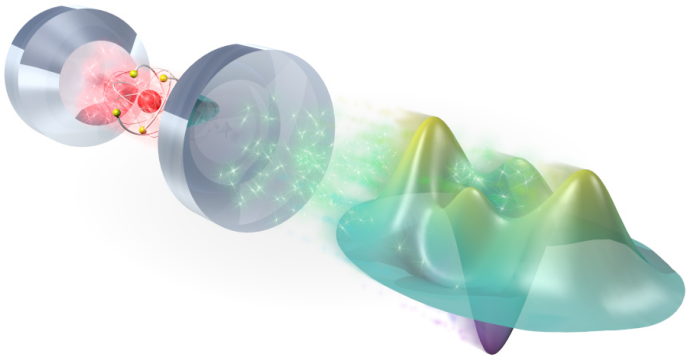

Dissertation

Max-Planck-Institut für Quantenoptik, Garching

and Physik Department, Technische Universität München

May 14, 2019

Cover illustration: The title cover displays the Wigner function of an experimentally created Schrödinger-cat state, flying away from a cavity that contains a single atom.

Max-Planck-Institut für Quantenoptik

Technische Universität München

Two-Photon Gate and Creation of Optical Cat States using One Atom in a Cavity

Bastian Hacker

Vollständiger Abdruck der von der Fakultät für Physik der Technischen Universität München zur Erlangung des akademischen Grades eines

Doktors der Naturwissenschaften (Dr. rer. nat.)

genehmigten Dissertation.

Vorsitzender :		Prof. Dr. Michael Knap
Prüfer der Dissertation :	1.	Hon.-Prof. Dr. Gerhard Rempe
	2.	Prof. Dr. Alexander Holleitner

Die Dissertation wurde am 14. 5. 2019 bei der Technischen Universität München eingereicht und durch die Fakultät für Physik am 10. 9. 2019 angenommen.

Abstract

This thesis reports on two novel optical quantum information processing experiments with a single rubidium atom trapped in a high-finesse cavity. The atom in the cavity can exchange information with light pulses reflected from the cavity, and enables the full coherent control of optical states.

In the first part, a universal quantum logic gate between polarization qubits of two photons in distinct temporal modes was implemented. It was the first realization of such a gate that is based on a deterministic protocol without a fundamental limit on its success probability. The implemented controlled-NOT (CNOT) gate was shown to invert the state of each photon conditioned on the state of the other one, and allowed to put two separable incoming photons into an entangled state.

In the second part of this work, the atom was deterministically entangled with coherent states of light, which contained a variable number of photons. This hybrid entangled state was used to prepare freely propagating optical pulses in coherent superposition states, also known as cat states. The resulting states were characterized in optical phase space and exhibited a number of genuine quantum features. The pioneered techniques could become the foundation of deterministic optical quantum information processing with numerous applications in future quantum networks.

Zusammenfassung

Die vorliegende Arbeit berichtet über zwei neuartige Experimente zur optischen Quanteninformationsverarbeitung mit einem einzelnen Rubidiumatom, das in einem Hohlraumresonator hoher Güte gefangen wird. Das Atom im Resonator kann Information mit Lichtpulsen, die am Resonator reflektiert werden, austauschen und ermöglicht die vollständige kohärente Kontrolle von optischen Zuständen.

Im ersten Teil wurde ein universelles Quantenlogikgatter zwischen den Polarisationsqubits zweier Photonen in verschiedenen zeitlichen Moden verwirklicht. Es war die erste Realisierung eines solchen Gatters, die auf einem deterministischen Verfahren basiert, dessen Erfolgswahrscheinlichkeit also nicht fundamental begrenzt ist. Es wurde gezeigt, dass das ausgeführte Kontrollierte-NOT (CNOT) Gatter den Zustand beider Photonen in Abhängigkeit des jeweils anderen invertieren und zwei separable einlaufende Photonen miteinander verschränken kann.

Im zweiten Teil der Arbeit wurde das Atom deterministisch mit kohärenten Lichtzuständen verschränkt, die eine variable Anzahl an Photonen enthielten. Ein solcher hybrider verschränkter Zustand wurde dazu verwendet, frei fliegende Superpositionszustände kohärenter Pulse herzustellen, die auch als Katzenzustände bekannt sind. Die erzeugten Zustände wurden im optischen Phasenraum charakterisiert und wiesen eine Reihe eindeutiger Quanteneigenschaften auf. Die erforschten Techniken könnten zur Grundlage deterministischer optischer Quanteninformationsverarbeitung werden mit zahlreichen Anwendungen in zukünftigen Quantennetzwerken.

Acknowledgments

This work would not have been possible without the invaluable support of a number of people. First and most of all I want to thank my advisor, Professor Gerhard Rempe. He has not only supported and guided me through all stages of this research; The experiment was only possible due to his vision and endurance, starting long before I even had an idea of what an atom was. Gerhard granted the freedom, patience and confidence to explore my ideas in the laboratory. With his passion and wisdom for discussing physics, he always spotted the problem that would then lead to a new discovery. I could not have asked for a better supervisor; Thank you Gerhard!

I want to express my sincere gratitude to Stephan Ritter, senior scientist and supervisor during the first years of this work, where he made a huge impact on the research in our team. He has been an exceptional manager, scientist and friend, and I'm deeply grateful for his wide support.

Soon after I had started out, Stephan Welte joined the experiment and became my lab companion for the past couple of years. Stephan and I shared much of the load to successfully operate the highly complex setup and to solve quite a number of intriguing research questions and mysteries, no matter the challenges and obstacles. Stephan is much valued for his modesty, diligence and the sense of culture he brought to the group. His subtle changes of conversation topics and his DJ skills are absolutely legendary. Thank you Stephan, working with you was a great pleasure!

I'm much indebted to all the former QGate members, who created a magnificent research apparatus with seemingly unlimited potential. In particular, I want to thank Andreas Reiserer and Norbert Kalb, who handed over the laboratory, taught me essential experimental techniques and physics and pioneered some truly remarkable research works.

I highly appreciate the precious work by the students who later joined the experiment. With Severin Daiss and Lukas Hartung, my PhD successors, the machine is in very good hands. Big thanks to Severin, who was not only a driving force in the laboratory, but also in the nightlife of Munich. I want to thank all our undergraduate and visiting students, Christoph Lienhard, Armin Shaukat, Pau Farrera and Tobias Nadolny, who brought fresh ideas to the lab and helped us move forward. A big thank you goes to our excellent post-docs Lin Li and Emanuele Distante. It was great fun to have you in the lab and learn from your experience! Lin, Armin and Severin invested substantial efforts to develop the homodyne detector to a stage where we could witness the extremely fragile quantum features of our optical states. Your contributions are highly appreciated. To Lin, all the best with your own newly founded research group!

Thanks to all the scientists in the Quantum Dynamics group for the highly pleasant and stimulating atmosphere! I much enjoyed our daily lunchtime discussions, table soccer sessions and group events. A big thanks goes to Stephan Dürr for providing answers to virtually any (physics) question. Special thanks to Matthias, Andi, Olivier, the Manuels, Dominik, Joe, Maria, Nico, Bo, Jonas, Josef, Steffen and Thomas for all the help, discussions and collaboration during the past few years. It was an honor working with you!

I owe sincere and earnest thankfulness to our superb technicians Tom, Tobi, Florian and Johannes, who were of important help in the laboratory. The experiment has greatly benefited from their ability to build essentially anything one can draw on a sheet of paper. I want to thank them in particular for their assistance with our often unconventional requirements.

I want to show my gratitude to all the administrative support at MPQ, who make workday life of the PhD students a whole lot easier. Foremost I want to thank Iris, who supported me from day one in the group. She did a remarkable job, taking care of countless matters well ahead of time and keeping everything running.

Finally, I want to thank my parents, who supported me always and unconditionally. You have kindled my passion for science from my childhood on, and encouraged me to dream big and follow these dreams. I am deeply grateful for all that. Without you, this work would not exist.

Thank You!

List of Publications

- **A photon-photon quantum gate based on a single atom in an optical resonator**.
  B. Hacker, S. Welte, G. Rempe, and S. Ritter. *Nature* **536**(7615), 193–196 (2016)
- **Recheneinheit für zwei Photonen**.
  S. Ritter, B. Hacker, S. Welte, and G. Rempe. *Physik in Unserer Zeit* **47**(6), 268–269 (2016)
- **Cavity Carving of Atomic Bell States**.
  S. Welte, B. Hacker, S. Daiss, S. Ritter, and G. Rempe. *Physical Reviev Letters* **118**(21), 210503 (2017)
- **Photon-Mediated Quantum Gate between Two Neutral Atoms in an Optical Cavity**.
  S. Welte, B. Hacker, S. Daiss, S. Ritter, and G. Rempe. *Physical Review X* **8**(1), 011018 (2018)
- **Deterministic creation of entangled atom-light Schödinger-cat states**.
  B. Hacker, S. Welte, S. Daiss, A. Shaukat, S. Ritter, L. Li and G. Rempe. *Nature Photonics* **13**(2), 110–115 (2019)
- **Single-Photon Distillation via a Photonic Parity Measurement Using Cavity QED**.
  S. Daiss, S. Welte, B. Hacker, L. Li and G. Rempe. *Physical Review Letters* **122**(13), 133603 (2019)

Contents

1. Introduction

The question about the nature of light is probably as old as humankind. Since the first philosophical models, science has led us a long way. In the 17th century, when many optical effects were still unknown, light was imagined – most prominently by Isaac Newton – to consist of tiny particles, emitted from light sources in straight lines. It propagates at a fast, but finite speed, which is known since Ole Rømer. When Christiaan Huygens came up with a modern wave theory of light in 1678, it was not yet widely accepted. This view however changed dramatically at the beginning of the 19th century, when experiments of Thomas Young, Augustin-Jean Fresnel and others demonstrated diffraction effects, such as the Poisson spot, that could only be explained by waves. The extensive study of electromagnetic effects by Michael Faraday, and their mathematical formulation by James Clerk Maxwell in 1864 finally established light as an electromagnetic wave [1]. This is known as the *classical* theory of light, and has tremendous explanatory power [2].

This perfect view was shattered at the beginning of the 20th century, when Max Planck discovered the law of black-body radiation. It involved the quantization of light-matter interaction in discrete packets of energy $E = hf$, proportional to the light frequency f with Planck's constant h. Albert Einstein, in spite of strong resistance from the physics community, took this idea of light quanta serious and explained the photoelectric effect in 1905 [3], assuming that light really does consist of particles, then called *photons*. The strange co-existence of wave and particle properties of light is since known as the *wave-particle duality*, and has been extended to other fundamental particles by Louis de Broglie. A consistent description is given by quantum mechanics, which was developed in the early 20th century by Werner Heisenberg, Erwin Schrödinger, Niels Bohr and many others. In *quantum optics*, light is described in terms of a so-called *wave function*. The dynamics are given by the *quantum harmonic oscillator* Hamiltonian and the outcome of a measurement is determined by respective measurement operators, both for wave- and particle properties. More details of the quantum theory of light were developed by Paul Dirac, Enrico Fermi and Richard Feynman (amongst many) in *quantum electrodynamics* as well as George Sudarshan, Roy Glauber and Leonard Mandel, who developed the concept of optical coherence in quantum optics. Today, these theoretical foundations are well confirmed by a plethora of laboratory experiments. Single photons are routinely created and detected, as are coherent light waves [4].

Quantum mechanics has not only brought a more accurate description of nature, but also some entirely new features, which have no counterpart in classical physics. A few examples are the disturbance of states upon measurement, the uncertainty principle, the existence of superpositions of states and the entanglement of spatially separate systems [5]. Discovered as a putative shortcoming of quantum theory in 1935 [6], these properties make the interpretation of quantum mechanics challenging ever since. Since the 1970s, however, the same properties have been realized as features [7] to implement a new type of information processing, now known as *quantum information* processing. Scientists like Yuri Manin, Richard Feynman [8] and David Deutsch realized that quantum systems could at least in principle perform certain computations more efficiently than classical computers. This includes the simulation of other quantum systems as well as classical tasks like the factorization of integer numbers. Another possibility is the implementation of information-theoretically secure cryptography, where the laws of quantum mechanics guarantee that

some transmitted information cannot be copied by an eavesdropper. The breakthrough of this *quantum cryptography* [9] came with the BB84 protocol for *quantum key distribution* in 1984, and is now commercially available with a number of implementations [10].

The basis of quantum information processing is the control over an isolated quantum system. Still in 1952 this was deemed impossible. Back then, Erwin Schrödinger stated, that "[...] we never experiment with just one electron or atom or (small) molecule. In thought-experiments we sometimes assume that we do; this invariably entails ridiculous consequences [...]" [11]. Only seven years later, Hans Georg Dehmelt built a Penning trap and used it to catch and store a single electron. In the following decades, ion traps have allowed to trap various species of single ions [12] and gain control over all their degrees of freedom. The strong trapping potential allows to store an ion continuously for years. With the advent of quantum information and the invention of the Cirac-Zoller [13] and the Mølmer-Sørensen gate [14] in the 1990s, atomic ions became a popular platform for the realization of small-scale quantum computers, with dozens of qubits and hundreds of subsequent gate operations today [15].

Neutral atoms have been more difficult to trap than ions, because they respond much less to electric and magnetic fields. Nevertheless, in 1985 cold neutral atoms were trapped using a magnetic trap [16]. The following years brought the inventions of laser cooling and the magneto-optical trap (MOT), which comfortably captures room-temperature atoms as a cold stationary cloud [17–19]. The laser, first realized in 1960, has since become the single most important experimental tool in quantum optics. In fact, a single focused laser beam alone is enough to trap an atom in vacuum. This so-called *dipole trap* uses the dynamic polarizability of the atomic ground state to create a small attractive potential.

But laser light itself is not only a tool, it also exhibits quantum properties that are required for quantum information processing. Light can encode quantum information in a variety of ways, such as in the amplitude, photon number, time-bins, orbital angular momentum or polarization. There are several appealing properties: Long coherence times (at least in vacuum), simple single-qubit processing devices (such as waveplates) and – most importantly – the possibility to be transmitted over large distances via fibers, which is the basis for *quantum communication* [20]. Single photons can be created at high rates, for instance by spontaneous parametric down-conversion. The key challenge is the lack of a direct interaction between photons. Since the surprising finding in 2001, that linear optical elements and photon detectors can provide an effective interaction between photons [21], linear optics quantum computing (LOQC) has become a thriving field of research [22]. To date, optical quantum technologies have demonstrated entanglement, Bell tests, quantum teleportation, the creation of complex quantum states and even small-scale quantum computations [23, 24]. However, the probabilistic nature of LOQC schemes, and the vast resource overhead necessary to overcome it, has been limiting controllable systems to few qubits. The application of optical quantum information today is mainly in quantum key distribution, where the state is immediately projected after a single transmission step.

To combine the transmission capability of optical systems with the processing capability of matter-based systems, a light-matter interface is required. Since the natural coupling between single light and matter quanta is generally small, such an interface requires a strong amplification of the optical light field, which is provided by small optical resonators (cavities) with a high finesse. Single atoms in cavities were pioneered in the 1980s in the microwave domain, and ground-breaking experiments with strong coupling between atoms and microwave photons were performed in the groups of Herbert Walther [25, 26] and Serge Haroche [27]. In microwave cavities, photons can be long-lived, and atoms, which pass through the cavity, can act as probes for the electromagnetic fields. Most remarkable, those experiments provided evidence for the existence of photons, independent from the

photoelectric effect and without destroying them upon detection [28]. In optical cavity quantum electrodynamics (cavity QED), which became possible with ultralow-loss mirrors in the 1990s [29], the roles of atom and light field are to some extent reversed compared to the microwave domain [30]. Here, the light field can travel and transmit quantum information over long distances, while the atom encodes a stationary, long-lived qubit. A cavity with strong optical light-matter coupling [31, 32] provides an efficient interface between flying optical and stationary matter qubits. The primary application of such a hybrid system [33] is as a node of a quantum network [34, 35]. Quantum networks may be employed to provide remote entanglement, connect small-scale quantum systems to a larger one, and eventually build up a global quantum internet [36, 37]. Single atomic ions, which have been employed to demonstrate much more complex quantum computations than with neutral atoms, have so far not been strongly coupled to optical fields, because ion traps tend to get disturbed by the close-by dielectric cavity mirrors or surface charges therein, but progress is being made [38]. Meanwhile, in the past fifteen years, cavity QED was independently studied with superconducting solid state systems on cryogenic electronic chips in so-called *circuit QED* [39]. Those systems have an overwhelming potential for local quantum information processing [40, 41]. Many techniques and protocols of cavity QED are shared between circuit QED and optical systems.

After decades of successful proof-of-principle quantum devices, quantum information technology today is at the verge of application. While many technologies of the past century, such as transistors, lasers, magnetic resonance imagers and atomic clocks, were enabled by the understanding of quantum physics during the *first quantum revolution*, the current step towards quantum information technology is sometimes called the *second quantum revolution* [42]. Quantum key distribution and cryptography systems are now commercially available, and research already extends to satellite-based systems [43]. Photon sources and detectors are steadily approaching unity efficiency, and complex multiphoton devices are miniaturized and integrated on chips [44]. Nonclassical states of light are finding applications in high-precision atomic clocks and gravitational wave detectors [45]. Meanwhile, laboratories perform quantum simulations with dozens of well-controlled single atoms, and large companies have dedicated themselves to developing universal scalable quantum computers. In Europe, a quantum flagship project has been launched to boost these efforts and unlock an unpredictable number of new applications [46].

The experiments of this thesis explore new ways of processing optical quantum information, harnessing the light-matter interaction with a single atom, mediated by a cavity. Now the atom becomes a tool to deterministically process photonic quantum information, which has so far relied on LOQC. The present setup achieves a maximal interaction between spatially and temporally distinguishable optical photons, performing a photonic quantum logic gate. In that, one photon can fully change the state of another one, for instance routing it to a different output mode while preserving coherence between the two particles. Optical waves with more than one photon can also be processed. This is demonstrated with coherent states of light, where feature-rich optical cat states are created and brought to a gate interaction with the atom. This demonstrates an unprecedented control of optical states, which is at the heart of many quantum network applications [47]. The atom-cavity system constitutes a textbook system to control light, ready for numerous future quantum network experiments.

This thesis is organized as follows: Chapter 2 summarizes the theoretical background of quantum information theory and cavity QED in particular. Chapter 3 describes the experimental setup, highlighting the current status, key features and some of the changes made to enable the presented experiments. Chapter 4 reports on the realization of a quantum gate between two photons, the first one that is not based on linear optics and probabilistic measurements, but on a deterministic protocol. Chapter 5 describes the production and

measurement of optical Schrödinger-cat states, including a detailed examination of their properties. Finally, Chapter 6 discusses the results in a broader context and sketches possible future developments.

2. Theoretical Background

2.1. Quantum Information

In a quantum-mechanical description, physical objects are state vectors $|\psi\rangle$ in a Hilbert space, possibly with an infinite number of dimensions. The bra-ket notation [48] used here is rather informal. Anything can be written inside the ket vector $|\cdot\rangle$ as long as its meaning is sufficiently clear. A system with several basis states $\{|0\rangle, |1\rangle, \ldots\}$ can take several distinct realizations, and thereby encode information. The simplest case of two basis states is called a quantum bit (qubit) [10].

The decisive difference to classical information systems is the *superposition principle*, that any state vector which is a normalized sum of other state vectors

$$|\psi\rangle = c_0|0\rangle + c_1|1\rangle, \qquad c_0, c_1 \in \mathbb{C}, \qquad |c_0|^2 + |c_1|^2 = 1 \tag{2.1}$$

is also a possible state of the system. To have a basis set of discriminable states, one requires them to be mutually orthogonal, i.e. to have a vanishing overlap $\langle 0|1\rangle = 0$, where the bra vector $\langle\cdot|$ is the adjoint of $|\cdot\rangle$ and $\langle\cdot|\cdot\rangle$ is the inner product between two states.

If the state of a system is not perfectly known, but is known to be in each of the states $|\psi_i\rangle$ with statistical probability p_i, the system can be described by a *density matrix*

$$\rho = \sum_i p_i |\psi_i\rangle\langle\psi_i| \; . \tag{2.2}$$

A density matrix with only one non-zero p_i represents a *pure* state, otherwise, if several linearly independent state vectors contribute, the state is *mixed*. The density matrix is a way to express one's knowledge about a system, often suited to represent experimentally measured data.

The physical realization of quantum information requires a system that is sufficiently controlled to prepare it in one defined state which cannot be decomposed further [49]. A prime example is the electronic state of an atom, where a complete set of quantum numbers uniquely defines a quantum state. Two states $|\downarrow\rangle$ and $|\uparrow\rangle$, picked from the large manifold of states, can form the basis for a qubit. The set of pure qubit states from superpositions of those two can be represented on the so-called *Bloch sphere* (Fig. 2.1(a)) [50]. Here, the two basis states $|\downarrow\rangle$ and $|\uparrow\rangle$ form two opposite poles of the sphere, whereas equal superpositions of the two, such as

$$|\rightarrow\rangle = \tfrac{1}{\sqrt{2}}(|\uparrow\rangle + |\downarrow\rangle), \quad |\leftarrow\rangle = \tfrac{1}{\sqrt{2}}(|\uparrow\rangle - |\downarrow\rangle), \tag{2.3}$$

$$|\otimes\rangle = \tfrac{1}{\sqrt{2}}(|\uparrow\rangle + i|\downarrow\rangle), \quad |\bullet\rangle = \tfrac{-1}{\sqrt{2}}(i|\uparrow\rangle + |\downarrow\rangle), \tag{2.4}$$

are located on the equator. All pure states are located at the surface of the sphere, and mixed states are located inside the volume.

Optical light in a defined mode at sufficiently low intensity may also exist in a pure state and encode quantum information. Two such encodings are used in this work. When the

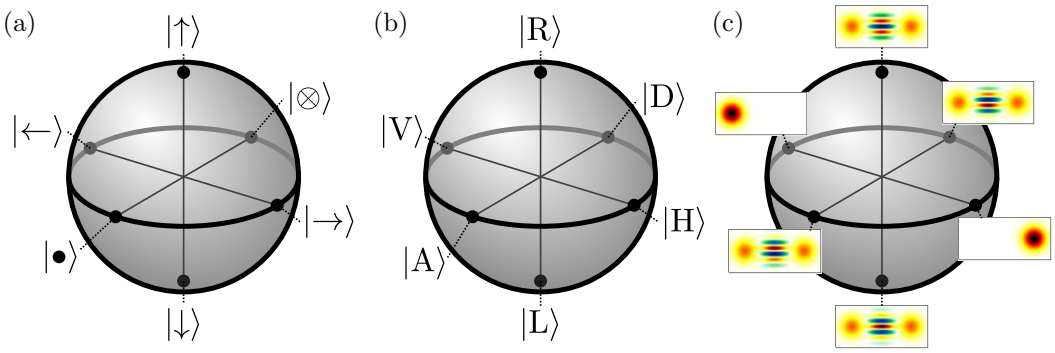

Figure 2.1.: Three qubit representations on the Bloch sphere used in this work. (a) Atomic-spin qubit, based on two spin states $|\uparrow\rangle$ and $|\downarrow\rangle$. (b) Single-photon polarization qubit with circular (R and L) and linear states (H, V, D and A). (c) Continuous-variable cat-state qubit. The insets show phase-space diagrams of two coherent basis states with positive and negative field amplitudes, as well as different superpositions of them with an interference pattern in the center (see Ch. 5).

number of photons is fixed to one, a qubit can be encoded in the polarization, that is the direction in which the electromagnetic field oscillates. This is a popular choice, because it may be preserved over long distances and does not require precise stabilization of optical path lengths. Different qubit states are equivalent to the polarization states on the *Poincaré sphere* of classical optics (Fig. 2.1(b)). With right- $|\mathrm{R}\rangle$ and left-handed $|\mathrm{L}\rangle$ polarization states chosen as the basis, several linearly polarized states can be defined as

$$\begin{aligned} |\mathrm{H}\rangle &= \frac{1}{\sqrt{2}}(|\mathrm{R}\rangle + |\mathrm{L}\rangle), \quad |\mathrm{V}\rangle = \frac{1}{\sqrt{2}}(|\mathrm{R}\rangle - |\mathrm{L}\rangle), \\ |\mathrm{D}\rangle &= \frac{1}{\sqrt{2}}(|\mathrm{R}\rangle + i|\mathrm{L}\rangle), \quad |\mathrm{A}\rangle = \frac{-1}{\sqrt{2}}(i|\mathrm{R}\rangle + |\mathrm{L}\rangle), \end{aligned} \tag{2.5}$$

where the letters stand for Horizontal, Vertical, Diagonal and Antidiagonal spatial directions, respectively.

A second optical encoding is in terms of coherent states of opposite optical field amplitudes $|\alpha\rangle$ and $|-\alpha\rangle$ (Fig. 2.1(c)). It will be explained and applied in Ch. 5. In that case, one fixed polarization ($|\mathrm{R}\rangle$) is used, but the photon number will have contributions of more than just one.

Manipulations of states are described by unitary operators $\hat{U}$, which turn an input state $|\psi\rangle$ into an output state given by the matrix product $\hat{U}|\psi\rangle$. In the context of quantum information [10], an operator may describe a quantum gate operation, for example a controlled-NOT (CNOT)-gate, which is defined by

$$\hat{U}_{\mathrm{CNOT}} = |00\rangle\langle 00| + |01\rangle\langle 01| + |11\rangle\langle 10| + |10\rangle\langle 11| = \begin{pmatrix} 1 & 0 & 0 & 0 \\ 0 & 1 & 0 & 0 \\ 0 & 0 & 0 & 1 \\ 0 & 0 & 1 & 0 \end{pmatrix}. \tag{2.6}$$

Its application will swap the two states $|10\rangle$ and $|11\rangle$.

Physical measurements are also described by operators – called observables – which must be Hermitian, i.e. self-adjoint with real eigenvalues. Any measurement will result in one of the observable's eigenvalues and project the state into the corresponding eigenstate. Given a state $|\psi\rangle$, the probability of measuring an eigenstate $|\psi_i\rangle$ is $|\langle\psi_i|\psi\rangle|^2$, the so-called *Born rule*.

2.2. Interaction of Light and Matter

One of the most fundamental processes in physics is the interaction of an atom with single photons [51]. The experiments of this work employ such an interaction to implement deterministic processing of optical quantum information. In free space, an atom has a maximum scattering cross-section for resonant light, which is $3\lambda^2/(2\pi)$ with the wavelength λ. However, the cross-section of a maximally focussed Gaussian beam with a finite divergence angle is always larger than that, thus keeping the interaction probability below 100%.

To achieve a strong light-matter interaction required for quantum nonlinear optics [52], several routes can be taken. One is to focus light from a large solid angle [53]. Recent experiments in this direction have been performed with large-numerical-aperture lenses [54] and parabolic mirrors [55]. A second, well studied approach is to use atomic ensembles instead of just a single atom, for instance atomic vapor cells or cold atomic clouds [56]. A third possibility is the use of an *optical resonator* – a cavity – where the optical field is resonantly enhanced at the position of the atom. Cavities can be built with very high quality factors and light amplification, such that the interaction between a single atom and a single photon becomes deterministic. The study of atoms in cavities – cavity QED – has produced an extensive body of research, theoretically and experimentally [35].

2.3. Cavity Quantum Electrodynamics

The interaction of an atom with the optical mode of a cavity is described by cavity quantum electrodynamics (QED) [57]. Light and matter can interact via the electric force between the electromagnetic field of light and the electric charge within an atom. Significant interactions at the single-photon level require resonance between the cavity eigenfrequency ω_c and an atomic dipole transition of energy difference $\hbar\omega_a$, at which the atom is well described as a two-level system. Here, $\hbar = h/(2\pi)$ is the reduced Planck constant and $\omega_i = 2\pi\, f_i$ are angular frequencies. The dynamics of atom and light field are captured by the well-studied Jaynes-Cummings (JC) Hamiltonian [58, 59]

$$\hat{H}_{\mathrm{JC}} = \underbrace{\hbar\omega_a\,\hat{\sigma}^+\hat{\sigma}^-}_{\text{atom}} + \underbrace{\hbar\omega_c\,\hat{a}^\dagger\hat{a}}_{\text{cavity field}} + \underbrace{\hbar g\,(\hat{a}\hat{\sigma}^+ + \hat{a}^\dagger\hat{\sigma}^-)}_{\text{dipole coupling}}\,, \tag{2.7}$$

where the three terms describe the energy of the bare atom, the energy of the light field and a coherent coupling of the two with an atom-photon coupling constant g. Here, $\hat{a}$ and $\hat{a}^\dagger$ are the photonic annihilation and creation operators, while $\hat{\sigma}^+ = |\mathrm{e}\rangle\langle\mathrm{g}|$ and $\hat{\sigma}^- = |\mathrm{g}\rangle\langle\mathrm{e}|$ are raising and lowering operators of the atomic state. This model assumes the rotating-wave approximation that rapidly oscillating terms at optical frequencies can be neglected. The JC Hamiltonian has eigenstates with an energy spectrum of

$$E_\pm(n) = n\,\hbar\omega_c + \tfrac{1}{2}\hbar\omega_a \pm \hbar\sqrt{ng^2 + \tfrac{1}{4}(\omega_a - \omega_c)^2}, \quad n \in \mathbb{N}_0\,. \tag{2.8}$$

This means that on resonance ($\omega_c = \omega_a$) the eigenfrequencies of the system are split by $2\sqrt{n}g$, the so-called *vacuum Rabi splitting* into two *normal modes* [31], and in particular $2g$ in the weak field limit with maximally one excitation at a time.

The single-photon coupling strength g is

$$g = \mu_{\mathrm{ge}}\sqrt{\frac{\omega}{2\hbar\epsilon_0 V}}\,, \tag{2.9}$$

determined by the atomic dipole matrix element $\mu_{\mathrm{ge}} = -e\langle \mathrm{g}|x|\mathrm{e}\rangle$ of the respective atomic transition between the states $|\mathrm{g}\rangle$ and $|\mathrm{e}\rangle$, by the light frequency ω and by the optical field configuration, given by the cavity geometry. Here, ϵ_0 is the electric constant and V is the cavity *mode volume*

$$V = \frac{\pi}{4} w_0^2 L \tag{2.10}$$

with mode waist w_0 and cavity length L. Hence, to reach a large coupling strength, both the cavity length and the mode waist have to be as small as possible.

Any real atom-cavity system additionally suffers from losses, namely spontaneous decay of the atomic excitation with a decay rate 2γ and damping of the optical cavity mode through absorption and mirror outcoupling with a total field decay rate κ. Those losses lead to a Lorentzian broadening of the energy spectrum by an atomic linewidth γ and a cavity resonance width κ, while the normal modes are broadened by $(\kappa+\gamma)/2$. To resolve the two eigenmodes in the frequency domain and to observe coherent dynamics in the time domain, one requires $g \gg \kappa, \gamma$, the *strong coupling* condition [60]. A less stringent requirement, relevant for the experiments of this work is a large *cooperativity* $C \gg 1$, where

$$C := \frac{g^2}{2\kappa\gamma} \,. \tag{2.11}$$

These conditions are challenging to reach in an experiment, because one requires both a small mode volume to reach large g and very little optical losses for a small κ. The decay constant γ is, in case of real atoms, given by nature and may be maximized by choosing a suitable transition.

The present experiment has the measured cavity QED parameters

$$g = 2\pi\, 7.8\,\mathrm{MHz}\,, \quad \kappa = 2\pi\, 2.5\,\mathrm{MHz}\,, \quad \gamma = 2\pi\, 3.0\,\mathrm{MHz}\,, \tag{2.12}$$

under the chosen experimental conditions, well within the strong coupling regime, which result in

$$C = 4.1\,. \tag{2.13}$$

2.4. Input-Output Theory of the Atom-Cavity System

The present experiment is based on a Fabry-Pérot cavity with two opposing mirrors (details in Sec. 3.7) and an atom trapped inside the cavity mode. The cavity is designed to be single-sided such that its optical losses are dominated by the transmission of one mirror (the outcoupling mirror), given by the rate κ_r, where light can enter and exit into a freely

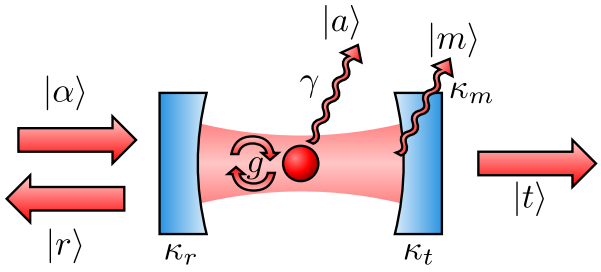

Figure 2.2.: Relevant optical modes of the atom-cavity system. Impinging mode $|\alpha\rangle$, reflected mode $|r\rangle$, transmission mode $|t\rangle$, light scattered by the atom $|a\rangle$ and by the mirrors $|m\rangle$.

propagating light mode. The second mirror has a much lower transmission rate κ_t, and with additional mirror absorption and scattering losses κ_m, the total cavity loss rate is $\kappa = \kappa_r + \kappa_t + \kappa_m$. In this setting, the atom-cavity system can be driven by a light pulse, impinging from outside along the axis of the cavity mode. In case of a light pulse with slowly varying envelope (compared to the dynamical time scales set by g, κ and γ), the system will take a steady-state, described by input-output theory [61–63]. Here, we consider the impinging optical mode $|\alpha\rangle$, reflected mode $|r\rangle$, the transmission mode $|t\rangle$, light scattered by the atom $|a\rangle$ and by the mirrors $|m\rangle$ (Fig. 2.2). The amplitudes in each of the output modes are obtained from a Heisenberg-Langevin equation for the steady-state [64–66]. The input light may have a detuning with respect to the cavity $\Delta_c = \omega - \omega_c$ and with respect to the atom $\Delta_a = \omega - \omega_a$.

The amplitudes for reflection r, transmission t, mirror losses m and scattering via the atom a with complex phase are:

$$r_{\downarrow/\uparrow} = \left(1 - \frac{2\kappa_r(\gamma + i\Delta_a)}{Ng^2 + (\kappa + i\Delta_c)(\gamma + i\Delta_a)}\right)\alpha \tag{2.14}$$

$$t_{\downarrow/\uparrow} = \frac{2\sqrt{\kappa_r\kappa_t}(\gamma + i\Delta_a)}{Ng^2 + (\kappa + i\Delta_c)(\gamma + i\Delta_a)}\alpha \tag{2.15}$$

$$m_{\downarrow/\uparrow} = \frac{2\sqrt{\kappa_r\kappa_m}(\gamma + i\Delta_a)}{Ng^2 + (\kappa + i\Delta_c)(\gamma + i\Delta_a)}\alpha \tag{2.16}$$

$$a_{\downarrow/\uparrow} = \frac{2\sqrt{\kappa_r\gamma}\sqrt{N}g}{Ng^2 + (\kappa + i\Delta_c)(\gamma + i\Delta_a)}\alpha \tag{2.17}$$

where $N = 1$ for the atom in a state $|\uparrow\rangle$ that couples to the light field ($|\uparrow\rangle \equiv |\mathrm{g}\rangle$ in the previous section), and $N = 0$ for the atom in a non-coupling state $|\downarrow\rangle$ such that the light field encounters an effectively empty cavity. Here, reflection $|r\rangle$ and transmission $|t\rangle$ modes have a well-defined phase with respect to the input light $|\alpha\rangle$. $|m\rangle$ and $|a\rangle$, however, are lost via incoherent scattering and may have an arbitrary phase.

2.5. Spectrum of the Atom-Cavity System

In the experiment, atom and cavity are usually tuned into resonance $\omega_c = \omega_a$. In this case, the light intensities in each mode, depending on the input detuning $\Delta = \Delta_c = \Delta_a$, become

$$R_{\downarrow/\uparrow}(\Delta) = |r_{\downarrow/\uparrow}(\Delta)|^2 = \left(1 - \frac{4\kappa_r(Ng^2\gamma + (\kappa - \kappa_r)(\gamma^2 + \Delta^2))}{(Ng^2 + \kappa\gamma - \Delta^2)^2 + (\kappa + \gamma)^2\Delta^2}\right)|\alpha|^2 \tag{2.18}$$

$$T_{\downarrow/\uparrow}(\Delta) = |t_{\downarrow/\uparrow}(\Delta)|^2 = \frac{4\kappa_r\kappa_t(\gamma^2 + \Delta^2)}{(Ng^2 + \kappa\gamma - \Delta^2)^2 + (\kappa + \gamma)^2\Delta^2}|\alpha|^2 \tag{2.19}$$

$$M_{\downarrow/\uparrow}(\Delta) = |m_{\downarrow/\uparrow}(\Delta)|^2 = \frac{4\kappa_r\kappa_m(\gamma^2 + \Delta^2)}{(Ng^2 + \kappa\gamma - \Delta^2)^2 + (\kappa + \gamma)^2\Delta^2}|\alpha|^2 \tag{2.20}$$

$$A_{\downarrow/\uparrow}(\Delta) = |a_{\downarrow/\uparrow}(\Delta)|^2 = \frac{4Ng^2\gamma\kappa_r}{(Ng^2 + \kappa\gamma - \Delta^2)^2 + (\kappa + \gamma)^2\Delta^2}|\alpha|^2\ . \tag{2.21}$$

In transmission, the empty cavity (without coupling atom, $|\downarrow\rangle$) has a Lorentzian spectrum $T_\downarrow(\Delta)$ and the cavity with a coupling atom has a spectrum of two normal modes $T_\uparrow(\Delta)$ [31, 32], shown in Fig. 2.3 with measured data. On resonance, the transmission is drastically reduced by a factor of $(1 + 2C)^2$ by the coupling atom.

In reflection, the intensities $R_{\downarrow/\uparrow}$ on resonance ($\Delta = 0$) for coupling and non-coupling atom can both be large, when $C \gg 1$. A measured reflection spectrum is shown in Fig. 2.4(a).

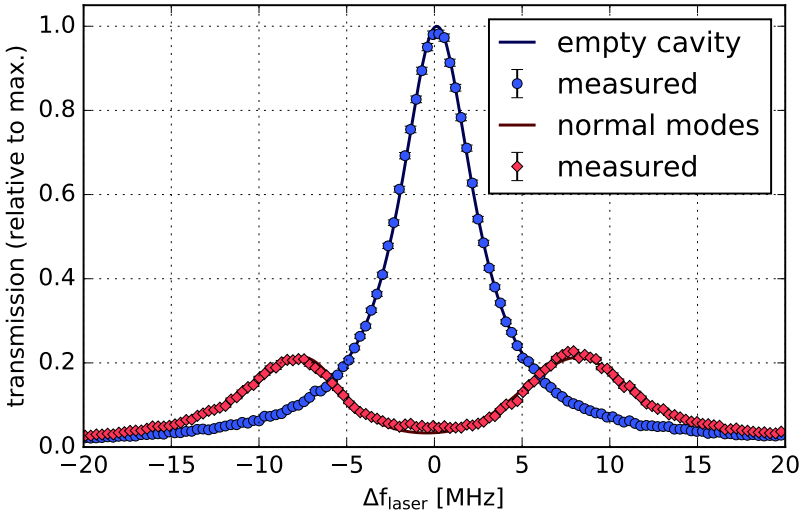

Figure 2.3.: Cavity transmission spectrum $T_{\downarrow/\uparrow}(\Delta)$ with the atom in a non-coupling state $|\downarrow\rangle$ (blue) and in the coupling state $|\uparrow\rangle$ (red). The empty cavity has a Lorentzian transmission profile of half-width $\kappa/(2\pi)$. The transmission spectrum with the coupling atom exhibits two normal modes with a fitted coupling constant of $g = 2\pi \cdot (7.85 \pm 0.02)\,\mathrm{MHz}$. On resonance, the coupling atom suppresses the transmission by 96%. The fit curves are the theoretical model with an broadened distribution of Δ_a due to thermal variations of the atomic energy potential in the trap.

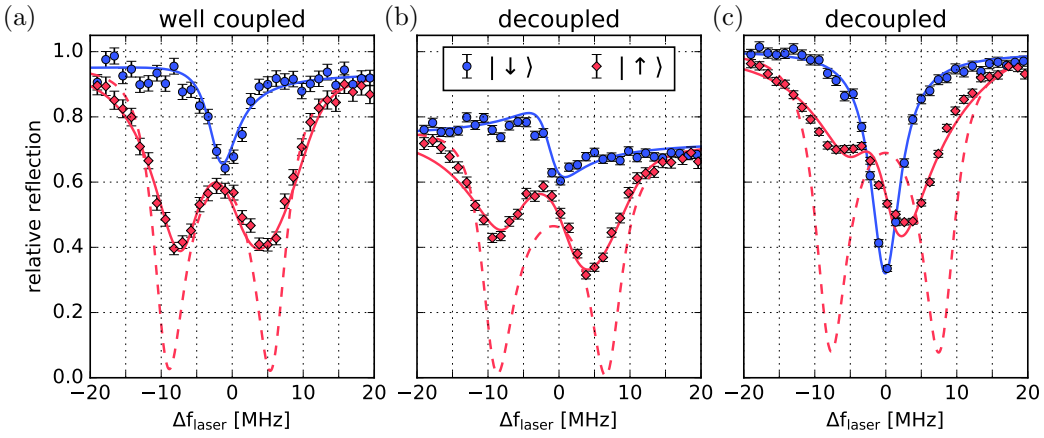

Figure 2.4.: Cavity reflection spectrum. With good mode matching of around 92% (a), the empty cavity reflection spectrum is close to a Lorentzian dip (blue line). The coupled atom-cavity system exhibits a double-dipped structure (red dashed line), which is smoothed out by the thermal distribution of the atom's potential energy in the trap and a resulting shift in its resonance frequency (red solid line). When the incoming optical beam gets decoupled from the cavity mode due to drifts of the beam geometry, the interference between coupled and non-coupled light increases and the reflection spectrum changes. Two examples are given for more constructive interference on resonance (b) and more destructive interference on resonance (c).

One observes a Lorentzian dip on the empty cavity reflection, because the cavity builds up a large intra-cavity field on resonance, which causes transmission and dissipation at the mirrors. With a coupling atom, the reflection is reduced at frequencies of $\Delta = \pm g$, where power is effectively transferred from the optical mode to the atom, which may then decay spontaneously. The measured spectrum in Fig. 2.4(a) (diamond symbols) is less pronounced than the theory of Eq. (2.18) (dashed curve), which is due to continuous fluctuations of the atomic resonance frequency in the trap by several megahertz.

One also observes that the reflection spectrum, which is recorded after a single-mode fiber, changes drastically with the geometric alignment of the cavity-coupled beam. While in Fig. 2.4(a) the modes of the incoming beam and the cavity are around 92% matched, the modes are more decoupled in Figs. 2.4(b),(c). In those cases, light which is in the cavity mode interferes with light that is not in the cavity mode and always reflects from the first cavity mirror. When those two contributions both impinge on a single-mode fiber, which collects the reflected light, they interfere phase-sensitively, so that the absorption spectrum becomes flatter (Fig. 2.4(b)) or steeper (Fig. 2.4(c)). In the experiment, such random interferences decrease the quality of measurements, and must either be avoided by an extremely stable optical setup, or by occasional monitoring and restoration of the mode coupling.

2.6. Cavity Reflection Phase Shift

The reflection amplitudes (Eq. (2.14)) on resonance with and without coupling atom

$$r_{\uparrow}(\Delta_c{=}\Delta_a{=}0) = \left(1 - \frac{2\kappa_r\gamma}{g^2+\kappa\gamma}\right)\alpha \tag{2.22}$$

$$r_{\downarrow}(\Delta_c{=}\Delta_a{=}0) = \left(1 - 2\frac{\kappa_r}{\kappa}\right)\alpha \tag{2.23}$$

have opposite signs if

$$\frac{1}{2} < \frac{\kappa_r}{\kappa} < C + \frac{1}{2}\,, \tag{2.24}$$

where $C = g^2/(2\kappa\gamma)$. Under this condition, the reflected light field obtains a phase flip in case of $|\uparrow\rangle$ with respect to $|\downarrow\rangle$. The empty cavity (with the atom in a non-coupling state) creates a phase shift of π due to a destructive interference condition at the incoupling mirror to build up a resonant field inside the cavity. A coupling atom however blocks the cavity transmission (cf. Fig. 2.3) such that light is directly reflected with zero phase shift. This phase is a common phase of the combined atom-light state, and was employed for the nondestructive detection of an optical photon, where the presence of a photon is witnessed by a phase flip in the state of the atom [67].

In case of a non-zero detuning of the impinging light Δ, the reflected light from the cavity gets phase-shifted by a varying amount (relative to a direct reflection from the incoupling mirror), which can be derived from Eq. (2.14),

$$\begin{aligned}\phi_{\downarrow/\uparrow} &= \arg(r_{\downarrow/\uparrow}/\alpha) = \\ &= \arctan2\big(2\Delta\kappa_r(\gamma^2+\Delta^2-Ng^2),\\ &\qquad (Ng^2+\kappa\gamma-\Delta^2)^2 + (\kappa+\gamma)^2\Delta^2 - 2\kappa_r(Ng^2\gamma+\kappa(\gamma^2+\Delta^2))\big)\,.\end{aligned} \tag{2.25}$$

The behavior of $\phi_{\downarrow}$ for the empty cavity and $\phi_{\uparrow}$ with a coupled atom is plotted in Fig. 2.5. Far off resonance, the phase shift is 0 or 2π in either case, because off-resonant light is always directly reflected from the incoupling mirror surface. The figure also shows phase

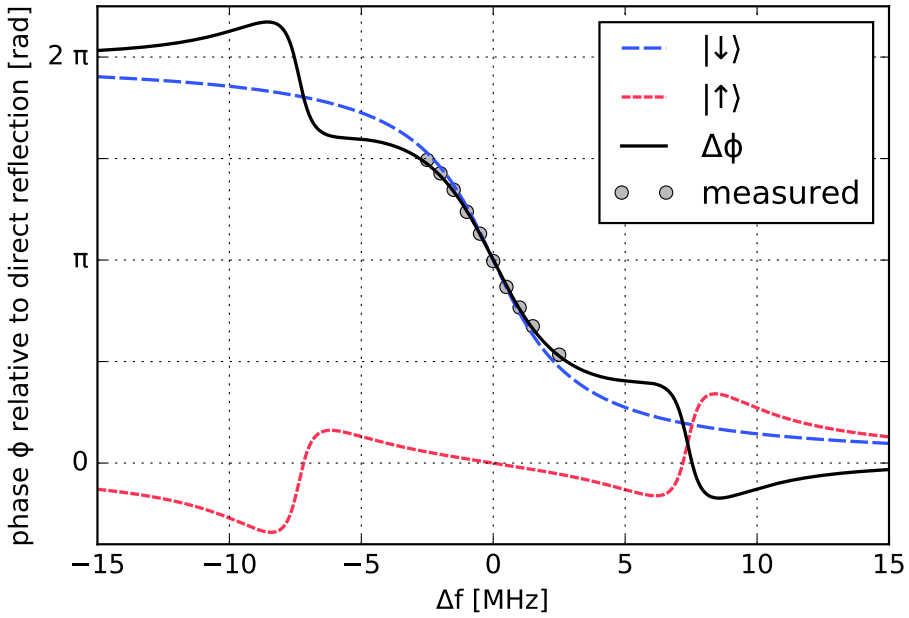

Figure 2.5.: Cavity phase shift in reflection. When the atom is not coupling to the cavity mode ($|\downarrow\rangle$), a reflected coherent light beam can enter the cavity and gets a π phase shift on resonance (dashed blue curve). A coupling atom ($|\uparrow\rangle$) however blocks the cavity and leads to a near-zero phase shift in reflection (dashed red curve). The phase difference $\Delta\phi$ (black solid line) between the two cases has a difference of π on resonance and is well-confirmed by a direct measurement in phase space (grey circles, data from Fig. 5.29).

differences, which were directly measured in phase space from phase-resolved amplitudes (Fig. 5.29).

The phase shift varies with the detunings between light, cavity resonance and atom:

$$\left.\frac{\mathrm{d}\phi_{\downarrow/\uparrow}}{\mathrm{d}\omega}\right|_{\Delta_c=\Delta_a=0} = \frac{2\kappa_r(\gamma^2 - Ng^2)}{(Ng^2+\kappa\gamma)(Ng^2+(\kappa-2\kappa_r)\gamma)} \tag{2.26}$$

$$\left.\frac{\mathrm{d}\phi_{\downarrow/\uparrow}}{\mathrm{d}\omega_c}\right|_{\Delta_c=\Delta_a=0} = \frac{-2\kappa_r\gamma^2}{(Ng^2+\kappa\gamma)(Ng^2+(\kappa-2\kappa_r)\gamma)} \tag{2.27}$$

$$\left.\frac{\mathrm{d}\phi_{\downarrow/\uparrow}}{\mathrm{d}\omega_a}\right|_{\Delta_c=\Delta_a=0} = \frac{2\kappa_r Ng^2}{(Ng^2+\kappa\gamma)(Ng^2+(\kappa-2\kappa_r)\gamma)} \tag{2.28}$$

With the parameters of the experiment, the change of differential shifts between coupling and non-coupling states with detuning are therefore

$$\frac{\mathrm{d}\phi_\downarrow - \mathrm{d}\phi_\uparrow}{\mathrm{d}f} = -0.82\,\mathrm{rad/MHz} \tag{2.29}$$

$$\frac{\mathrm{d}\phi_\downarrow - \mathrm{d}\phi_\uparrow}{\mathrm{d}f_c} = 0.89\,\mathrm{rad/MHz} \tag{2.30}$$

$$\frac{\mathrm{d}\phi_\downarrow - \mathrm{d}\phi_\uparrow}{\mathrm{d}f_a} = -0.07\,\mathrm{rad/MHz}\,. \tag{2.31}$$

A well-defined phase shift $\Delta\phi \ll \pi$ requires a sufficiently small spectral width Δf of the optical pulse. In the limit of large cooperativity C and single-sidedness κ_r/κ, this condition becomes

$$\Delta f \ll \kappa\,. \tag{2.32}$$

2.7. Phase-Shift Operator

In order to describe a quantum light field, the phase shift is expressed by a phase-shift operator [68]

$$\hat{U}(\phi) = e^{-i\phi\hat{n}} = \sum_n e^{-in\phi}|n\rangle\langle n| \tag{2.33}$$

in terms of Fock states $|n\rangle$ that contain exactly n photons. Each Fock component $|n\rangle$ obtains a phase $e^{-in\phi}$,

$$\hat{U}(\phi)|n\rangle = e^{-in\phi}|n\rangle \tag{2.34}$$

which is a phase factor outside of the state vector. A coherent state of light $|\alpha\rangle$, which has a well-defined amplitude $|\alpha|$ and optical phase $\arg(\alpha)$, expressed in a Fock basis is [69]

$$|\alpha\rangle = e^{-\frac{|\alpha|^2}{2}} \sum_{n=0}^{\infty} \frac{\alpha^n}{\sqrt{n!}}|n\rangle \ . \tag{2.35}$$

Thus, the phase-shift operator creates

$$\hat{U}(\phi)|\alpha\rangle = e^{-\frac{|\alpha|^2}{2}} \sum_{n=0}^{\infty} \frac{e^{-in\phi}\alpha^n}{\sqrt{n!}}|n\rangle = |e^{-i\phi}\alpha\rangle \ , \tag{2.36}$$

an optical phase inside the state vector.

In the resonant case of $\phi = \pi$, both types of states obtain respective sign flips:

$$\hat{U}(\pi)|n\rangle = (-1)^n|n\rangle \tag{2.37}$$

$$\hat{U}(\pi)|\alpha\rangle = |-\alpha\rangle \tag{2.38}$$

The sign flip of Eq. (2.37) will be used in Chapter 4 to perform single-photon quantum logic gate operations, whereas the optical phase flip of Eq. (2.38) will be used in Chapter 5 to manipulate coherent states in phase space.

2.8. Photon-Polarization Dependence

The atomic transition $|\uparrow\rangle \leftrightarrow |\mathrm{e}\rangle$, to which the cavity-resonant light field couples, is a σ^+-transition, which corresponds to $|\mathrm{R}\rangle$-polarized light in the cavity reflection mode. $|\mathrm{L}\rangle$-polarized light, however, hardly couples to the atom, because the corresponding transition (Sec. 3.3) is detuned from the cavity resonance by many linewidths, and the transition strength (Clebsch–Gordan coefficient) is much lower. Coupling between atom and light field is thus only achieved for the atom in $|\uparrow\rangle$ and for photons in $|\mathrm{R}\rangle$, whereas all cases with $|\downarrow\rangle$ or $|\mathrm{L}\rangle$ do not couple. The reflection of a photon therefore leads to a state-dependent phase shift

$$\begin{aligned} |\downarrow\rangle|\mathrm{L}\rangle &\to -|\downarrow\rangle|\mathrm{L}\rangle & \qquad |\uparrow\rangle|\mathrm{L}\rangle &\to -|\uparrow\rangle|\mathrm{L}\rangle \\ |\downarrow\rangle|\mathrm{R}\rangle &\to -|\downarrow\rangle|\mathrm{R}\rangle & \qquad |\uparrow\rangle|\mathrm{R}\rangle &\to +|\uparrow\rangle|\mathrm{R}\rangle \ , \end{aligned} \tag{2.39}$$

an atom-photon controlled-phase gate, that was first demonstrated in the present experimental setup [70, 71], following the proposal of [72]. The global phase in the gate is arbitrary and results from a chosen convention.

3. Experimental Setup

The experiments of this work have been conducted at the "QGate" setup in the Quantum Dynamics division of Professor Gerhard Rempe at the Max Planck Institute of Quantum Optics. The core of the experiment is a macroscopic high-finesse Fabry-Pérot cavity in a vacuum chamber. Single rubidium atoms can be trapped optically at the cavity center, controlled by a set of laser beams. The setup enables the conduction of cavity QED experiments under near-ideal conditions.

3.1. Overview

The QGate setup is built on one optical table, which includes five lasers, optics for beam preparation, a vacuum chamber with the cavity inside, and optics for state detection and measurement, such as single-photon detectors and photodiodes. A photograph of the core part of the optical setup is shown in Fig. 3.1 and a combined image of the full setup is depicted in Appendix A. The optical setup is organized in several parts which are connected by optical fibers. Those parts are laser beam preparation, optical state detection and the free-space coupled environment of the cavity. The latter is sketched in Fig. 3.2, including beam paths and all major optical elements.

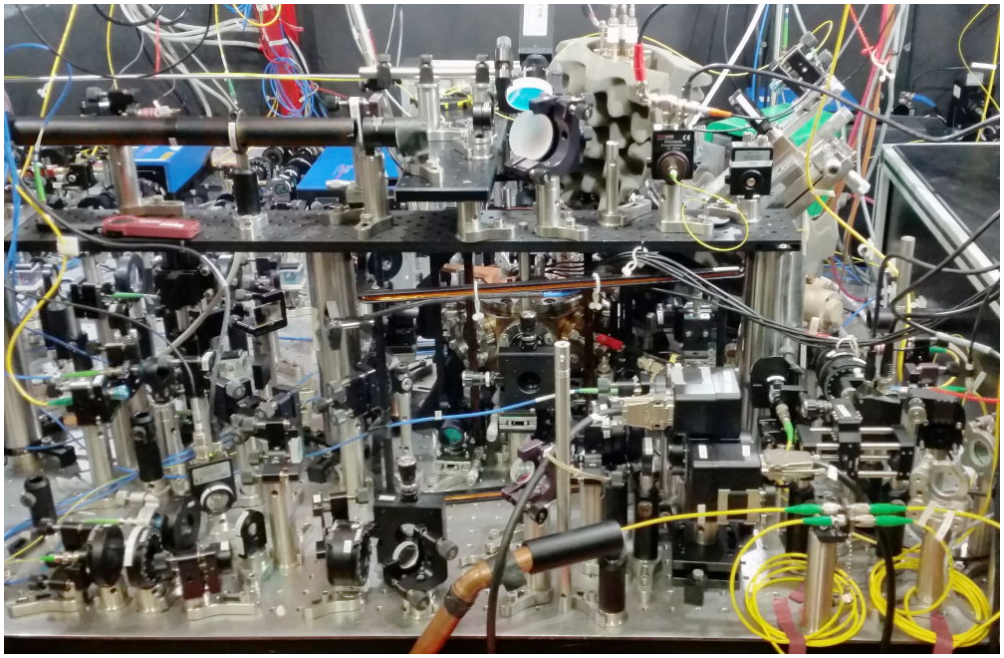

Figure 3.1.: Central part of the QGate experiment during this work. The small octagonal vacuum chamber in the center is surrounded by magnetic coils, free-space optics and optical fibers (blue and yellow). Laser beams are not visible in this picture.

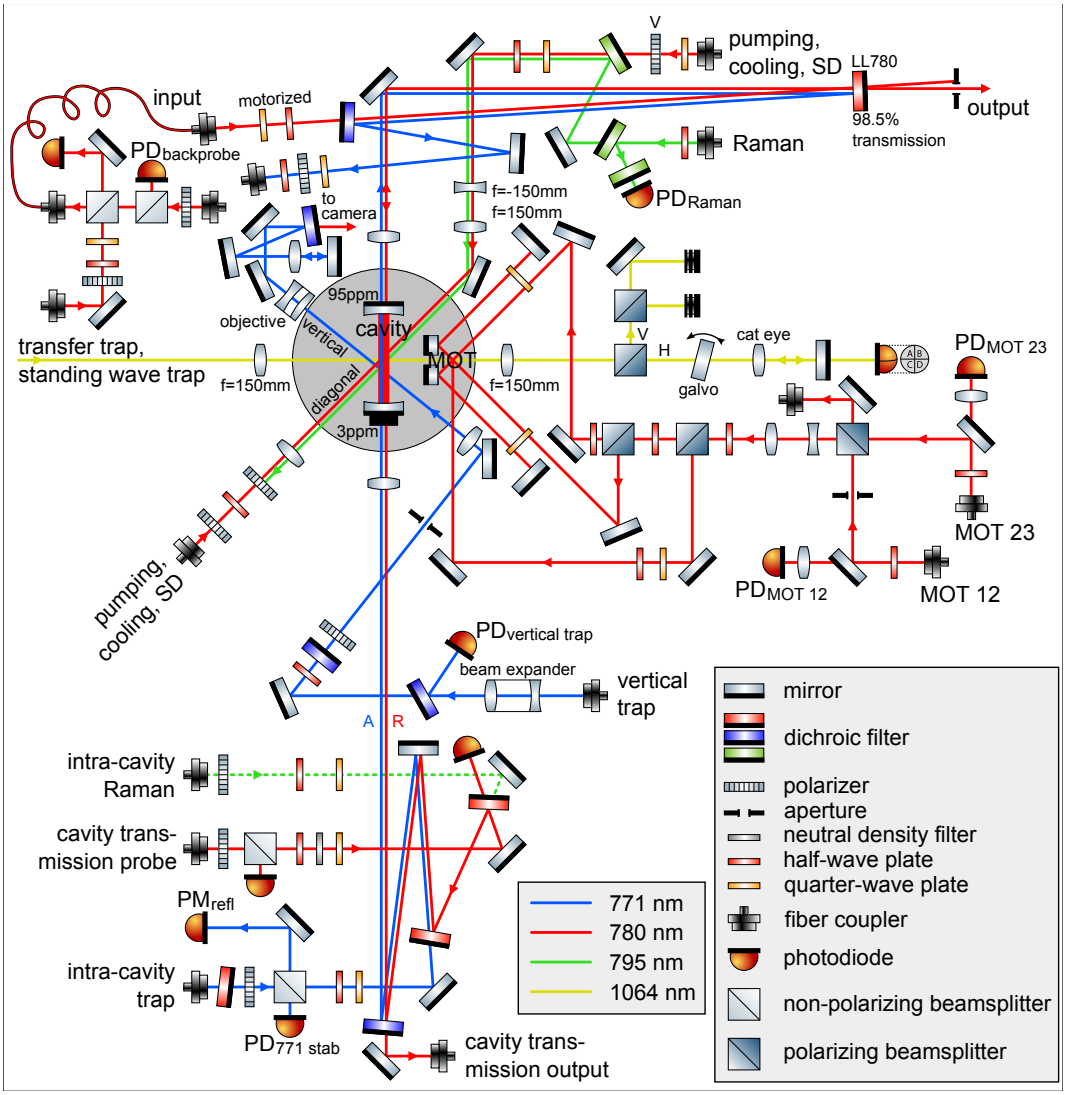

Figure 3.2.: Optical setup around the cavity. The vacuum chamber (grey circle) is surrounded by free-space optics that guide and manipulate the laser beams between fiber couplers and the cavity. The setup consists of various independent parts: MOT (red beams on the right), 1064 nm dipole trap (yellow), 771 nm vertical trap (blue, central), diagonal cavity beam (green top part), cavity low-transmission side (lower part), and cavity high-transmission side (upper part). The input and output of optical pulses that carry quantum information happens on the high-transmission side, with more details in Figures 4.2 and 5.6. The three-dimensional geometry around the cavity (horizontal, diagonal and vertical beams) are projected into the image plane here.

3.2. Precursor Experiments with the QGate setup

Construction of the experiment started in 2000 with the goal to use cavity QED for quantum information processing, a vision that has now become reality. The experiment was set up by Stefan Nußmann [73] with a custom-made vacuum chamber, a MOT of rubidium atoms, a mechanism to transport atoms into the cavity [74], and a high-finesse cavity from two dielectric mirrors that was later replaced. This first cavity [75], in use until 2009, had initially very similar parameters as the current one, but was degraded by a dust grain on its mirror surface. A microscope was added to the experiment [76], which allows to image single atoms with a resolution of 1.3 µm at a numerical aperture of NA = 0.43, sufficient to determine the number of trapped atoms and the lattice site of each atom in a standing-wave optical dipole trap [77]. Additional laser beams that pass between the two cavity mirrors have been employed to control trapped atoms, for instance to induce the emission of single photons [78] and entangled photon pairs [79].

From 2008 to 2010, QGate was overhauled. This included many technological upgrades as well as the exchange of the cavity inside the vacuum chamber, which had been accidentally destroyed by a strong laser beam of the 1064 nm atom trap. The setup was then used to implement a single-atom quantum memory for incoming photons [80]. The installation of a Raman laser pair has since enabled fast coherent manipulation of atomic states [81]. Then, QGate was connected to a second, very similar cavity setup, called "Pistol" [82], through an optical fiber. Together they formed an elementary quantum network [34], which allowed for a remote state transfer between two atoms in distant cavities [83]. The subsequent implementation of a three-dimensional standing-wave dipole trap enabled tight confinement of atoms in the cavity mode [84] and strong coupling between atoms and cavity light. This allowed for the nondestructive detection of photons and the implementation of an atom-photon quantum gate [71] as well as a heralded quantum memory [85].

With this backdrop, QGate is well-suited to explore the rich world of hybrid light-matter quantum information processing. This includes experimental protocols with several atoms, several photons, and several cavities to build up fully-fledged quantum networks. The processing of complex optical states with more than one photon, which is the topic of this work, required us to build a homodyne detection setup, initial progress of which is reported in [86]. Experiments with several atoms [87, 88], which were conducted in the past few years, are the topic of Stephan Welte's thesis [89].

3.3. Rubidium Atoms

The experiments in this work were performed with single trapped rubidium atoms (an alkali metal with atomic number 37). In particular, the ^{87}Rb isotope was used, which has nuclear spin $I = 3/2$, as opposed to the other available ^{85}Rb isotope with $I = 5/2$. Trapping and manipulation of rubidium atoms is well-studied, and applied in numerous quantum optics laboratories around the world [91].

An energy level scheme of ^{87}Rb with the relevant quantum states and energies is shown in Fig. 3.3. Two states in the hyperfine ground-state manifold, $|\downarrow\rangle := |5^2S_{1/2}, F{=}1, m_F{=}1\rangle$ and $|\uparrow\rangle := |5^2S_{1/2}, F{=}2, m_F{=}2\rangle$, are employed as the basis states of a qubit. The cavity is tuned into resonance with the optical D_2 transition between the two states $|\uparrow\rangle$ and $|e\rangle := |5^2P_{3/2}, F{=}3, m_F{=}3\rangle$.

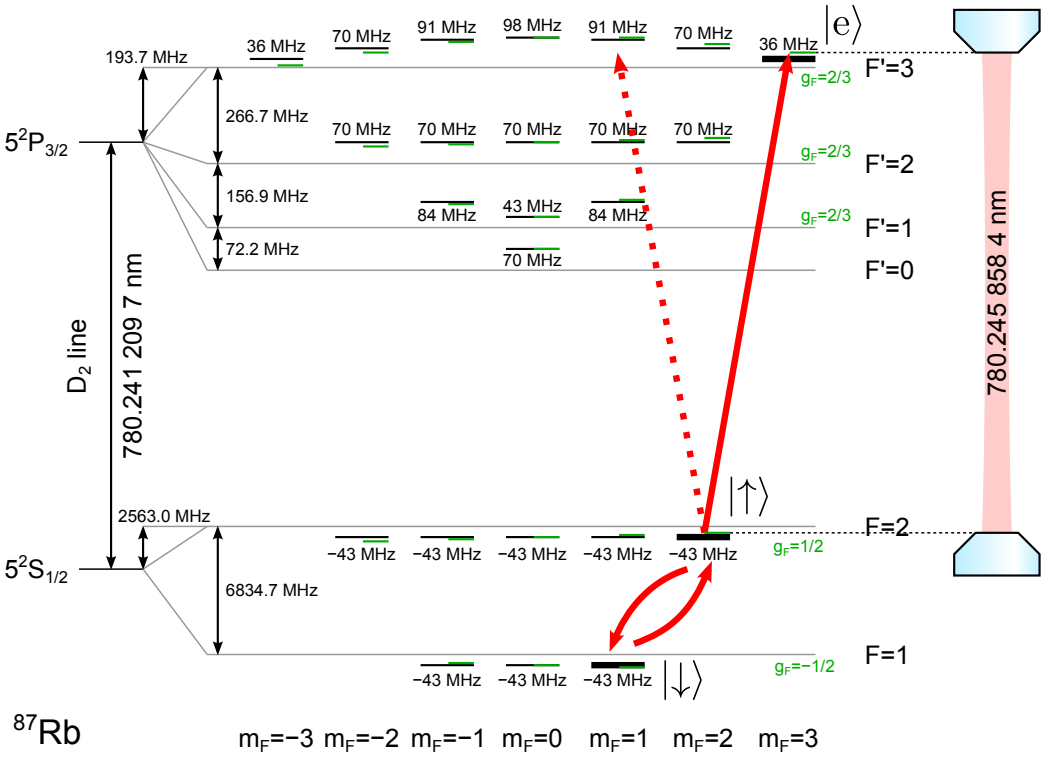

Figure 3.3.: Energy level scheme of ^{87}Rb. The diagram shows the energy levels of the $5^2S_{1/2}$ (ground state) manifold and the $5^2P_{3/2}$ manifold, which are connected by the D_2 line at 780 nm. The grey lines show the hyperfine splitting of various F-states [90]. Additional energy shifts are due to the AC-Stark effect of the 1064 nm dipole trap, which shifts the ground state by a trapping potential of −43 MHz at the given beam geometry and trap intensity of 1.8 W. The degeneracy of the $F' = 1$ and $F' = 3$ levels is lifted by several tens of megahertz due to tensor light shifts [77]. A magnetic guiding field of $B = 71\,\mu$T creates an additional Zeeman shift of $g_F m_F B \cdot 0.014\,\text{MHz}/\mu\text{T}$ (shown in green). The most important levels for the experiment (bold lines) are the two long-lived qubit states $|\downarrow\rangle = |5^2S_{1/2}, F{=}1, m_F{=}1\rangle$ and $|\uparrow\rangle = |5^2S_{1/2}, F{=}2, m_F{=}2\rangle$, as well as the excited state $|e\rangle = |5^2P_{3/2}, F'{=}3, m_F{=}3\rangle$, which is coupled to $|\uparrow\rangle$ by the cavity light field. The cavity-resonant transition $|\uparrow\rangle \leftrightarrow |e\rangle$ is shifted by 79 MHz through the dipole trap and 1 MHz by the constant applied magnetic field.

3.4. Trapping and Cooling

At the beginning of each experiment, an electrically heated dispenser releases hot vapor of rubidium atoms into the ultra-high vacuum. A cloud of $\approx 10^7$ atoms is caught with a magneto-optical trap (MOT) and immediately laser-cooled down to ≈100 µK [73]. The atom cloud is then transferred over a distance of 12 mm into the cavity with an optical running-wave dipole trap that has its focus right between MOT and the cavity center and a Rayleigh-length of 4.6 mm [74]. This transfer trap takes around 180 ms to move the atoms into the cavity. As soon as the cloud arrives, a 3D optical lattice [71, 84] in the cavity is switched on and the camera takes an image of the atomic fluorescence from a cooling laser. On average, one atom arrives at the cavity center through the shallow transfer trap. The whole loading sequence lasts a few seconds, and automatically repeats until exactly one atom in the cavity is found on the camera image.

The 3D optical lattice (see Tab. 3.1 for parameters and Fig. 3.6(a) for a sketch) consists of one far-off-resonance red-detuned dipole trap at 1064 nm, horizontal and orthogonal to

Table 3.1.: Laser beams interacting with the atom. The π-polarization has the electric field oscillating along the cavity (and quantization) axis, wheres all other polarizations oscillate orthogonal to it.

Beam	Wavelength	Waist	Power	Polarization
Transfer trap	1064 nm	43 µm	2 W	V
Standing-wave trap	1064 nm	16 µm	1.8 W	π
Vertical trap	771 nm	8 µm	20 mW	π
Intra-cavity trap	771 nm	29 µm	180 µW	A
Cavity mode	780 nm	29 µm	$\approx$1 pW	arbitrary
Diagonal pump beam	780 nm	34 µm	$\approx$1 µW	π and D
Diagonal Raman beam	795 nm	34 µm	7 mW	π and D

the cavity axis, as well as two blue-detuned traps at 771 nm, along the cavity axis and in vertical direction. The red-detuned trap creates an attractive potential of $h \cdot 43$ MHz (2 mK) for atoms in the ground state, that allows to keep atoms trapped up to a minute, limited by collisions with background gas in the vacuum, and enables precise positioning through an optical conveyor-belt mechanism [73]. The blue-detuned traps are repulsive and keep the atom within an anti-node of their standing-wave structure. This is particularly important in the direction of the cavity axis to ensure the positioning within a node of the standing-wave 780 nm cavity mode, which is used for the interaction of the atom with reflecting photons. The choice of repulsive blue-detuned traps has two particular advantages, as the atoms will be trapped in an intensity minimum: First, the off-resonant scattering of trap-light photons is low and second, the AC-Stark shifts which vary both with the motional state of the atom and with the trap intensity, are kept at a minimum.

In between experiment runs, which last for less than a millisecond, the atom is laser-cooled, in order to stay in the trap with only a few motional quanta. The applied cooling technique is Sisyphus cooling [73, 91] with two diagonal cooling beams in opposite direction in lin$\perp$lin configuration. The cooling laser is 10 MHz red-detuned from the bare (not AC-Stark shifted) $F{=}2 \leftrightarrow F'{=}3$ transition and a repumping laser is 30 MHz blue-detuned from the bare $F{=}1 \leftrightarrow F'{=}2$ transition, highly red-detuned from the AC-Stark shifted transitions. Typical cooling temperatures are on the order of 100 µK. No Raman sideband cooling [84] or cavity cooling schemes were required for the presented experiments.

3.5. Atomic State Control

In thermal equilibrium at 100 µK, the atom effectively only occupies the $5^2S_{1/2}$ ground state manifold. A pure $|F{=}2, m_F{=}2\rangle$ state is reached via optical pumping with circularly polarized (R) light, which impinges on the low-transmission cavity mirror and is partially transmitted as long as the atom is not yet in $|F{=}2, m_F{=}2\rangle$. During the pumping period of 200 µs the m_F quantum number increases successively until the atom reaches the $|F{=}2, m_F{=}2\rangle \leftrightarrow |F'{=}3, m_F{=}3\rangle$ cycling transition (marked in Fig. 3.3), while a repumping laser at the $F{=}1 \leftrightarrow F'{=}2$ transition avoids any population in the $F{=}1$ manifold. Successful pumping is eventually heralded by a decrease of the cavity transmission due to the normal mode splitting (Fig. 2.3). When a very high state preparation fidelity is required, the pumping interval can also be followed by a resonant state detection, which projects the state into or outside the desired initial state $|\uparrow\rangle$.

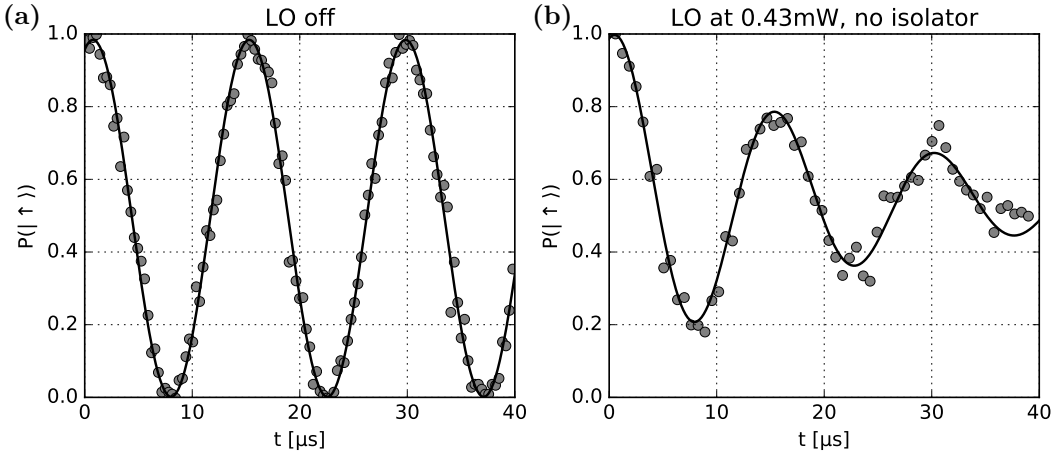

Figure 3.4.: Rabi oscillations. The atom is coherently transferred between the states $|\uparrow\rangle$ and $|\downarrow\rangle$ by a Raman laser pair. The probability $P(\uparrow)$ to find the atom in $|\uparrow\rangle$ oscillates with the pulse length at a period of 15 µs. (a) Undisturbed Rabi oscillation with coherence times far beyond the 40 µs time scale shown here, typically limited by magnetic field fluctuations to around 200 µs. (b) Disturbed by a resonant light field, in this case scattered from a local oscillator (LO) beam at 0.43 mW (described in Sec. 5.8), reduces the coherence time to 24 ± 2 µs. The solid lines are fits of an exponentially damped oscillation.

Once the atom is in a single quantum state, it can be transferred to well-defined superpositions of several long-lived $5^2S_{1/2}$ hyperfine states, in particular with the second chosen qubit state $|\downarrow\rangle$. As the qubit transition $|\downarrow\rangle \leftrightarrow |\uparrow\rangle$ spans a microwave frequency of 6.8 GHz, Rabi oscillations between the states can be driven with a resonant microwave beam or, to achieve fast transition periods on the order of microseconds, with a pair of co-propagating Raman lasers with a frequency difference of 6.8 GHz, operated 131 GHz detuned from the D_1 transition at 795 nm [81]. This way, an arbitrary qubit state of $|\uparrow\rangle$ and $|\downarrow\rangle$ can be prepared, where the laser intensity and pulse length sets the qubit rotation angle and a small two-photon detuning from the transition frequency sets the qubit rotation axis. An example of a coherent qubit rotation is shown in Fig. 3.4(a), where pulses of varying length lead to an oscillation in the probability to measure $|\uparrow\rangle$ or $|\downarrow\rangle$.

The qubit-carrying photons are resonant with both the cavity and the AC-Stark shifted $|\uparrow\rangle \leftrightarrow |e\rangle$ transition. For all experiments described in this thesis, the atom is first prepared in a desired state and then a few-microsecond long signal pulse is reflected from the high-transmission side of the cavity. The linewidth of the applied laser was measured to be 250 kHz, currently limited by the optical frequency comb of 200 kHz linewidth, to which it is phase-locked. These linewidths may be reduced in future experiments by the use of an ultrastable reference-cavity for short-term stability. The optical power of the signal pulses used to undergo significant long-term drifts, and was actively stabilized in the course of this work to obtain well-defined signal photon numbers. Similarly, the beam of the intra-cavity trap was stabilized to the cavity-transmitted power, to create a stable light intensity within the cavity and thereby reduce the parametric heating of atoms.

3.6. Spin-Qubit Coherence

All experiments in this work require the capability to prepare the atom in a superposition state of $|\uparrow\rangle$ and $|\downarrow\rangle$ in the $5^2S_{1/2}$ manifold. The two states have an energy difference of

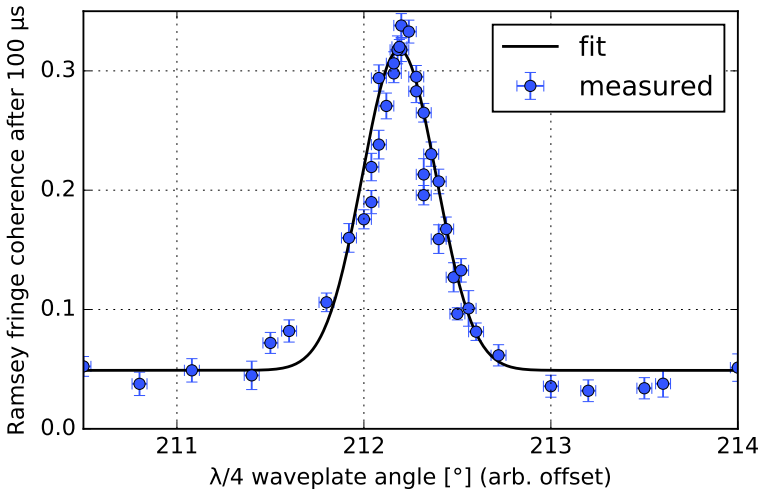

Figure 3.5.: Decoherence effect of circularly-polarized trap components. Oscillation amplitude of Ramsey fringes vs. rotation angle of a $\lambda/4$-waveplate for the 771 nm intra-cavity trap after a 100 µs free evolution time. Ramsey fringes only appear for a very specific setting of the waveplate of $212.19° \pm 0.20°$. This is the point where the trap polarization within the cavity becomes linear, such that no vector light shifts occur. Otherwise those fields induce spin decoherence and the visibility of Ramsey fringes is reduced drastically.

6.834 682 611 GHz [90] when no external magnetic or electric fields are applied. The superposition phase, which evolves at this frequency, can be tracked with our Raman laser pair, which obtains their frequency difference indirectly from a very accurate hydrogen maser clock. In principle the coherence time can exceed hundreds of milliseconds with carefully chosen qubit states, as shown in our research group recently [92].

The challenge is the influence of external magnetic fields, which shift the energy levels of the $|\uparrow\rangle$ and $|\downarrow\rangle$ states in opposite directions. The magnetic field sensitivity of the $|\uparrow\rangle \leftrightarrow |\downarrow\rangle$-transition frequency is $3 \times 7\,\mathrm{kHz/\mu T}$ [90]. Therefore the local earth's magnetic field of around 48 µT with daily fluctuations of about 0.1 µT leads to transition frequency fluctuations on a kHz-scale. Other fluctuating magnetic fields are present in the laboratory environment, such as 50 Hz noise of the electric mains.

An accurate way to measure the coherence time is the Ramsey method, where the spin is brought into an equal superposition of $|\uparrow\rangle$ and $|\downarrow\rangle$ by a $\pi/2$ rotation, then the superposition evolves freely for a time period T, and finally a second $\pi/2$ pulse is applied. If the phase evolution during T is constant during repeated measurements, the mean outcome of a final state detection of the spin will oscillate as a function of the phase of the second pulse and produce so-called Ramsey fringes. If the spin is subject to a varying phase evolution, the fringe visibility is reduced.

In addition to the real magnetic field in the lab, the optical dipole traps may have circular polarization components along the quantization axis, which result in state-dependent vector light shifts that have the same effect on the splitting of m_F states as magnetic fields [93]. The atoms in our experiments are normally not in the motional ground state, and thus experience varying vector light shifts from trap light. For the intra-cavity trap, the effect is aggravated, because tiny fluctuations of the cavity length lead to a fluctuating intensity of incoupled trap light. To avoid vector light shifts, the trap light needs to be strictly linearly polarized inside the cavity. When the trap polarization is tuned by a quarter-wave plate, the Ramsey fringe visibilities of Fig. 3.5 are observed after a free evolution time of $T = 100\,\mu\mathrm{s}$.

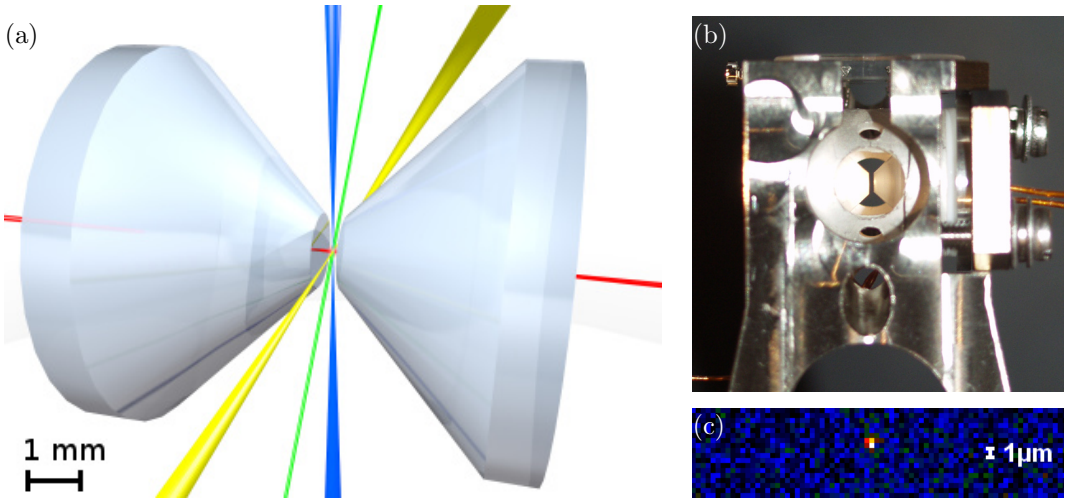

Figure 3.6.: The cavity. (a) Laser beams between the two cavity mirrors (artist's impression, to scale). Depicted beams are the horizontal 1064 nm trap (yellow), the vertical 771 nm trap (blue), pumping, state detection and Raman beams at a 45° angle (green) and the cavity mode (red). (b) Photograph of the mounted cavity with a 0.5 mm mirror gap in the center (from [73]). (c) Microscope image of one single atom trapped in the cavity with diffraction-limited resolution.

Here, coherence times of 100 µs are only reached when the waveplate setting is correct within $\pm 0.2°$ and thus the circularly polarized fraction of the trap light is below 0.5%.

3.7. The Cavity

The cavity, or optical resonator, shown in Fig. 3.6, consists of two dielectric mirrors with high reflectivity and low losses. The mirrors have reflecting surfaces of quarter-wave stacks of SiO_2 and Ta_2O_5 on fused silica substrates [73]. Each mirror has a diameter of 7.67 mm and a thickness of 4 mm with the reflecting side trimmed down to a diameter of 1.5 mm at a 45° angle. The mirror surfaces are concave with a 50 mm radius of curvature, necessary for a small optical mode waist.

The cavity is single-sided, meaning that one mirror has much less transmission than the other one. The mirror transmissions are (3 ± 1) ppm and (92 ± 3) ppm, the combined scattering and absorption losses (7 ± 3) ppm and the total round-trip loss (102 ± 3) ppm [71, 80]. The finesse is therefore $\mathcal{F} = (6.1 \pm 0.2) \cdot 10^4$, a relatively large value.

An ideal Fabry-Pérot cavity with mirror distance L has a discrete transmission spectrum at frequencies $n \cdot \Delta f$ with integer n and a free spectral range $\Delta f = c/(2L)$. At $\lambda_0 = 780$ nm the cavity has a free spectral range of $\Delta f = 309.0$ GHz. Our cavity, however, is made from dielectric mirrors with an optical penetration depth that changes significantly with wavelength and alters the effective cavity length. Thus, L and Δf are not constants, and the resonance frequency f_{res} is not an integer multiple of Δf. With a wavelength-dependent mirror penetration depth, which also depends on the exact thickness of the manufactured quarter-wave layers, the cavity length $L = (485 \pm 1)$ µm is so-far only known to within a few half-wavelengths. The cavity length and mirror radii determine the cavity mode waist $\omega_0 = 29$ µm of the TEM00 mode at λ_0 and the mode volume $V = \pi\omega_0^2 L/4 = 3.3 \cdot 10^5$ µm^3. The total cavity field decay rate is $\kappa = \kappa_r + \kappa_t + \kappa_m = 102\,\mathrm{ppm} \cdot c/(4L) = 2\pi\, 2.51$ MHz, with $\kappa_r = 2\pi\, 2.26$ MHz, $\kappa_t = 2\pi\, 0.07$ MHz and $\kappa_m = 2\pi\, 0.17$ MHz.

Even though the absolute cavity length is not known exactly, the mirror distance needs to match extremely precisely to one resonance length, on the order of $\Delta L = L \cdot 0.15\,\mathrm{MHz}/f_{\mathrm{res}} = 0.2\,\mathrm{pm}$ (for a 0.15 MHz stability of the resonance frequency), much less than the diameter of an atom. Therefore the cavity length is actively stabilized using the intra-cavity trap laser at 771 nm with a Pound-Drever-Hall lock [94] and a length-tunable piezo tube [73]. The locking bandwidth is limited by mechanical resonances to around 10 kHz and residual short-term fluctuations of the resonance frequency are limited by the laser linewidth of 250 kHz. The locking laser impinges on the high-reflection side (blue beam from below in Fig. 3.2) and the cavity-transmitted light is detected on a fiber-coupled avalanche photodiode. The Pound-Drever-Hall error signal is converted into a feedback signal by an anolog PID controller, which is then fed to the piezo tube that controls the cavity length with a displacement of around 5 nm/V. The necessary precision of the cavity length of 0.2 pm requires a piezo voltage precision of 30 µV. A new locking circuit based on SMA components was found to be much more resilient to electromagnetic interference from external devices than the previously used one, based on BNC components. The accuracy of the cavity lock is so far limited to 0.15 MHz root mean square (RMS), mainly by the linewidths of the lasers and the frequency comb they are locked to, as well as a first-order 100 Hz electronic low-pass filter right before the piezo, which protects the cavity from accidental voltage spikes.

3.8. Cavity Frequency Drift

The Pound-Drever-Hall stabilization laser cannot be operated at the atomic resonance wavelength λ_0, because the continuous intensity of several microwatts required for a good signal-to-noise ratio of the lock would strongly excite the atoms and interfere with the experimental light pulses. Therefore, the cavity is locked 15 free spectral ranges above λ_0, at a vacuum wavelength of 770.945 709 nm (blue cavity beam in Fig. 3.2).

When the cavity is stably locked at around 771 nm with a long-term accuracy in the kHz range, we nevertheless found a slow frequency drift of the 780 nm cavity resonance, which is caused by the 1.8 W standing-wave trap laser beam that passes transversally between the cavity mirrors. This behavior is shown in Fig. 3.7(a). When the trap laser is switched on or off, the cavity resonance drifts exponentially with a time constant of 10 minutes and an amplitude of 700 kHz. That is a considerable fraction of the cavity linewidth $\kappa/(2\pi) = 2.5\,\mathrm{MHz}$ and therefore relevant for cavity induced phase shifts. This effect, which has already been a disturbance in earlier experiments, may now be explained as follows: A small fraction of the 1.8 W of trap light (around 50 µW), which is not in a perfect Gaussian mode, hits the cavity mirrors and heats up the dielectric coatings. The coatings expand thermally and change their thickness, as well as their refractive index by a small amount (about 10^{-7}). Therefore, the optical penetration depth of the cavity mode changes, and this effect differs slightly between the locking wavelength at 771 nm and the resonance wavelength at 780 nm. Due to the high finesse, tiny phase differences are considerably amplified. I estimated numerically, that a temperature change of less than 1 K already suffices to explain the observed differential frequency drift of 700 kHz. Such a temperature change is easily produced in the vacuum, and the timescale of ten minutes is compatible with the thermalization of the mirrors.

We also observed that the feedback-regulated piezo voltage of the cavity lock drifts considerably over time when the experiment is running (Fig. 3.7(b)). With a piezoelectric cavity length change of around 5 nm/V, the observed drift of around 100 V translates to 0.5 µm, which is explained by thermal expansion of the piezo tube [73]. Since the differential frequency drift and the piezo voltage drift have a common cause, namely the heat of the trap laser beam, they are correlated (Fig. 3.7(c)). This can be exploited by a feedforward of the piezo voltage to the offset frequency of the locking laser, to reduce the cavity drift amplitude

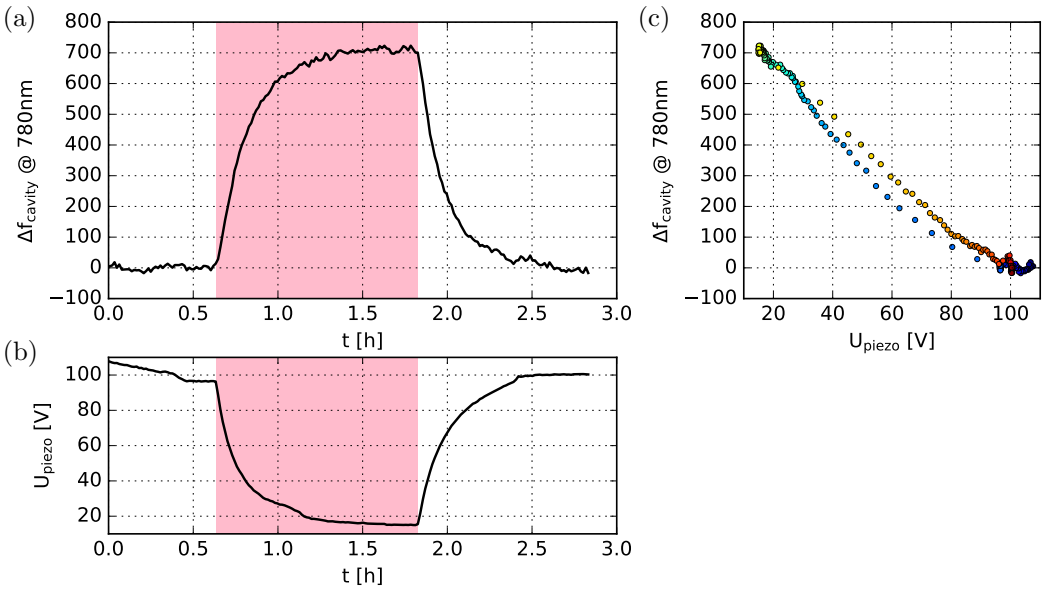

Figure 3.7.: Thermal drift of the 780 nm cavity resonance. Time traces of the optically measured cavity resonance drift (a) and regulated voltage of the cavity lock piezo (b) within three hours. During the red-shaded region, the standing wave trap (Standing-wave trap in Tab. 3.1) was switched on. This causes a drift of the 780 nm cavity resonance by 700 kHz with an exponential time constant of 10 minutes, while the cavity stays locked at 771 nm. (c) Piezo voltage vs. cavity resonance offset, with time encoded as color from blue (= 0 h) to red (= 3 h).

from 700 kHz to around 200 kHz. However, since the thermal drifts are quite unreliable, the absolute frequency still had to be calibrated on a daily basis.

Eventually, we implemented a more robust stabilization of the slow frequency drift: In between subsequent experiments, the cavity transmission is probed 2.5 MHz (one κ) below and 2.5 MHz above the desired resonance frequency, where the slope of the Lorentzian transmission profile (Fig. 2.3) is maximal. The transmission ratio is recorded by a field-programmable gate array (FPGA) and subsequent measurements are averaged over several seconds for a sufficient signal-to-noise ratio. The deviation from a 50/50 transmission ratio quantifies the frequency offset and creates an error signal, that is fed back to the frequency of the locking laser through a PI-controller in the FPGA. This way, slow drifts of the cavity resonance at 780 nm can be compensated with an accuracy down to 10 kHz, much smaller than the cavity linewidth κ and an improvement to a factor of 70 over the previous situation.

3.9. Transverse Optical Mode Matching

Good overlap between the transverse mode profiles of the incoming light and the optical cavity is essential for a deterministic interaction between the light pulse and a trapped atom. To this end, the incoming optical pulses are taken from a single-mode fiber with its mode matched to the cavity. In a characterization measurement it was determined that 92% of probe light emanating from the cavity is coupled into this input fiber. Therefore, 8% of the impinging light may arrive in an orthogonal mode that does not interact with the atom-cavity system. Light in this mode deteriorates the fidelity of the photonic state if it is collected at the output. This problem can be mitigated when the output light is collected by a fiber with its mode well matched to the cavity. However, a small misalignment, e.g.

due to slow temperature drifts, reduces the positive filtering effect described above. Thus, optimal mode matching is essential to perform high-quality operations on photons. In the experiments, reflection spectra of the empty cavity (Fig. 2.4) were constantly monitored and, whenever necessary, data taking was interrupted to reestablish optimal mode overlap.

The achieved mode matching of 92% is however not a fundamental limit. It was found after the experiments of this work, that a suitable telescope with additional degrees of freedom can improve the mode matching between the cavity and a single-mode fiber substantially.

3.10. Cavity Birefringence

An ideal rotationally symmetric optical cavity has discrete frequency eigenmodes, which do not depend on polarization. However, in high-finesse cavities, tiny stress-induced and intrinsic anisotropies in the mirror surface lead to the formation of two distinct orthogonal polarization eigenmodes [95]. Such a birefringence is present in the QGate cavity. The resonance frequency differs maximally between near-diagonally (50° to the horizontal) and anti-diagonally polarized light by $\Delta_b = 410\,\mathrm{kHz}$. This value has remained stable since the cavity was installed in 2010 [80]. For the quantum information experiments in this work the birefringence is an imperfection that causes deviations from the ideal cavity-induced phase shifts of Sec. 2.4. With the frequency splitting being much smaller than the cavity linewidth κ, it can be treated as a perturbation to the ideal behavior, similar than in [85].

A frequency splitting of two polarization eigenmodes results in a detuning Δ_c between incoming light and the cavity resonance at least for some polarization states. This causes a phase change in the reflected light, quantified by Eq. (2.26) without a coupling atom

$$\frac{\mathrm{d}\phi_\downarrow}{\mathrm{d}\omega_c} \cdot 2\pi\Delta_b = \frac{2\kappa_r}{\kappa(2\kappa_r - \kappa)} \cdot 2\pi\Delta_b = 0.12\,\pi =: 2\xi \tag{3.1}$$

and with coupling atom

$$\frac{\mathrm{d}\phi_\uparrow}{\mathrm{d}\omega_c} \cdot 2\pi\Delta_b = \frac{-2\kappa_r\gamma^2}{(g^2+\kappa\gamma)(g^2+(\kappa-2\kappa_r)\gamma)} \cdot 2\pi\Delta_b = -0.0015\,\pi\,. \tag{3.2}$$

Clearly, the birefringence-induced reflection phase shift ξ is strongly suppressed by a coupling atom by an amount of C^2. Therefore, in case of a coupling atom $|\uparrow\rangle$, the mode $|\mathrm{R}\rangle$, which couples to an atomic transition and is effectively blocked from entering the cavity, gets reflected without phase shift and unaffected by the birefringence. $|\mathrm{L}\rangle$-polarized light, which never couples to the atom, gets phase-shifted by a fixed phase ϕ, which is typically set to π. The birefringence only plays a role in case of $|\downarrow\rangle$. Then, the differential phase shift of Eq. (3.1) between the polarizations $|\mathrm{D}\rangle$ and $|\mathrm{A}\rangle$ causes a fixed polarization rotation $R_p(\xi) = e^{i\xi}|\mathrm{D}\rangle\langle\mathrm{D}| + e^{-i\xi}|\mathrm{A}\rangle\langle\mathrm{A}|$ around the polarization eigenaxes of the cavity (D and A). All this together can be described by a combined atom-photon operator U_{ap} in the basis $\{|\downarrow\mathrm{L}\rangle, |\downarrow\mathrm{R}\rangle, |\uparrow\mathrm{L}\rangle, |\uparrow\mathrm{R}\rangle\}$, which then becomes

$$U_{ap} = \begin{pmatrix} & & 0 & 0 \\ \multicolumn{2}{c}{R_p(\xi)} & 0 & 0 \\ 0 & 0 & 1 & 0 \\ 0 & 0 & 0 & e^{-i\phi} \end{pmatrix}. \tag{3.3}$$

This operator describes the cavity-reflection based atom-photon controlled-phase gate (Eq. (2.39)) in the presence of cavity birefringence.

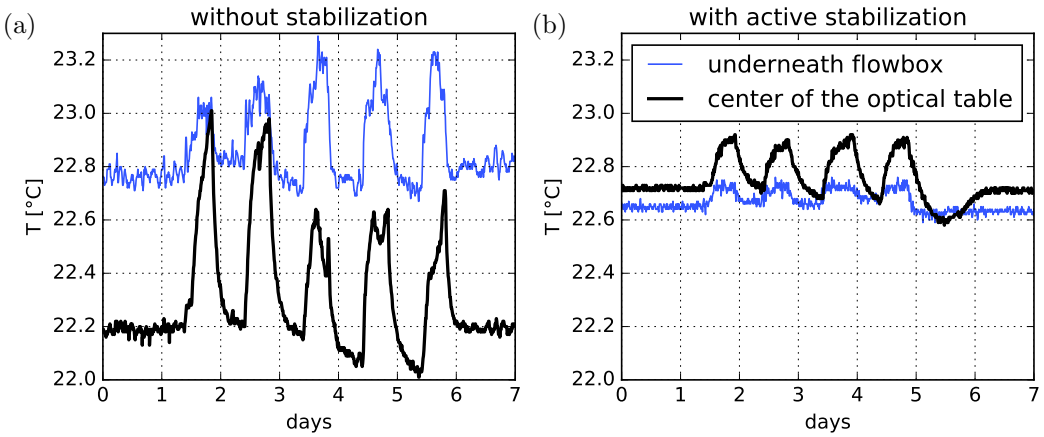

Figure 3.8.: Temperature variation in the lab within one week. Before stabilization (a) and afterwards (b). Underneath the flowbox, close to the stabilization sensor, the span reduced from 0.5 K to 0.1 K. On the optical table, the range reduced from 1.0 K to 0.3 K.

3.11. Temperature Stabilization

For a reliable operation of the experiment, the pointings of laser beams around the vacuum chamber need an accuracy of around a micrometer, even after meters of propagation. However, any change in temperature slightly changes the geometry due to thermal expansion of optical components. The whole laboratory is temperature stabilized by an external air conditioning to a span of 1 K, but the variable emitted heat in the lab prevents a better stability. On the optical table the temperature is additionally influenced by heat emitted from the lasers and electric devices above the experiment. Before the experiments of this thesis, the temperature on the optical table fluctuated by around 1 K within one day (Fig. 3.8(a)). This led to a drift of the atom position inside the cavity by around 10 µm and a significant change of the optical mode matching between cavity and impinging light within few hours. Thus, the setup changed faster than the time it takes to calibrate it, which made it challenging to perform reproducible experiments.

As a solution, we installed a custom-made temperature stabilization for the optical table. The table is surrounded by acrylic glass windows, and a steady downward stream of air is provided by two flowboxes. We added two water-air heat exchangers in front of the flowbox intakes, which keep the air temperature on the optical table constant. The heat exchangers have a thickness of 4 cm and an effective area of 4 m^2 and allow to change the air temperature by around 25% of the water temperature change, at the typical amount of air flow. The air temperature is measured by two PT100 sensors underneath the flowboxes and the temperature error signal is fed to the controllers of two Julabo CF31 water chillers with a cooling power of 0.3 kW. Figure 3.8(b) shows the temperature progression on the optical table after the stabilization was activated. The air flow temperature is now stable to 0.1 K (blue line), limited by spatial temperature variations and an imperfect mixing of air inside the flowbox. On the optical table the temperature has become stable to 0.3 K (black line), limited by local heat sources such as lasers, magnetic coils, the rubidium dispenser and beam dumps. The final achieved temperature stability was sufficient for the experiments of this work.

4. Quantum Gate between two Photons

Some contents of this chapter have been published in [96]: **A photon-photon quantum gate based on a single atom in an optical resonator**. B. Hacker, S. Welte, G. Rempe, and S. Ritter. *Nature* **536**(7615), 193–196 (2016)

Two photons in free space pass each other undisturbed. This is ideal for the faithful transmission of information, but prohibits an interaction between the photons as required for a plethora of applications in optical quantum information processing [97]. The long-standing challenge here is to realize a deterministic photon-photon gate. This requires an interaction so strong that the two photons can shift each other's phase by π radians. For polarization qubits, this amounts to the conditional flipping of one photon's polarization to an orthogonal state.

So far, only probabilistic gates [21] based on linear optics and photon detectors could be realized [98], as "no known or foreseen material has an optical nonlinearity strong enough to implement this conditional phase shift [...]" [99]. Thus, the variety of implemented two-photon quantum gates [98, 100–106] (and many others) were all based on linear optics [22].

Meanwhile, tremendous progress in the development of quantum-nonlinear systems has opened up new possibilities for single-photon experiments [52]. Platforms range from Rydberg blockade in atomic ensembles [107] to single-atom cavity QED [35]. Applications like single-photon switches [108] and transistors [109, 110], extraction of single photons [111], two-photon gateways [112], nondestructive photon detectors [67], photon routers [113] and nonlinear phase shifters [114–118] have been demonstrated, but none of them with the ultimate information carriers, optical qubits in discriminable modes. Here we employ the strong light-matter coupling provided by a single atom in a cavity to realize the Duan-Kimble protocol [72] of a universal controlled phase controlled-phase (CPHASE) photon-photon quantum gate, sometimes also called controlled phase flip (CPF) or controlled-Z (CZ) gate. This is the first implementation of a photon-photon quantum gate that uses a deterministic protocol [96]. The second implementation, based on Rydberg interactions, was also recently demonstrated in the research group of Gerhard Rempe [119]. Other proposals, such as a cavity-based $\sqrt{\text{SWAP}}$-gate [120] still await their implementation.

The perhaps simplest idea to realize a photonic quantum gate is to overlap the two photons in a nonlinear medium. However, it has been argued that this cannot ensure full mutual information transfer between the qubits for locality and causality reasons [121, 122]. Instead, a viable strategy is to keep the two photons separate, change the medium with the first one, use this change to affect the second photon, and, finally, make the first photon interact with the medium again to ensure gate reciprocity. These three subsequent interactions enable full mutual information exchange between the two qubits, as required for a gate, even though the photons never meet directly.

This experimental realization of a CPHASE photon-photon gate builds on the proposal by Duan and Kimble [72]. The medium is the single atom strongly coupled to the cavity and the interactions happen upon reflection of each photon off the atom-cavity system [70]. While the proposal considers three reflections, we replaced the second reflection of the first photon by a measurement of the atomic state and classical phase feedback on the first photon

(analogous to a proposal [123] where the roles of light and matter are interchanged). These steps are equivalent to a second reflection of the first photon, which causes a π phase flip on $|\mathrm{R}\rangle$ in case the atom is in $|\uparrow\rangle$. In practice, this allows us to achieve better fidelities, higher efficiencies and to use a simpler setup compared to that of the proposed scheme.

4.1. Protocol

Figure 4.1(a) depicts the experimental steps of the photon-photon gate as a quantum circuit diagram. In short, the protocol starts with arbitrary photonic input qubits $|p_1\rangle$ and $|p_2\rangle$ and the atom optically pumped to $|\uparrow\rangle$. After this initialization, two consecutive atomic-qubit rotations combined with CZ atom-photon quantum gates (Eq. (2.39)) are performed. The purpose of the rotations is to maximize the effect of the subsequent gates. Up to this point the first photon has the capability to act via the atom onto the second photon. To implement a back-action of the second photon onto the first one, the protocol ends with a measurement of the atomic qubit and feedback onto the first photon. This measurement has the additional advantage that it removes any possible entanglement of the atom with the photons, as required for an ancillary qubit.

The action of the quantum circuit diagram can be computed in the eight-dimensional Hilbert space spanned by the atomic ancilla qubit and the two photonic qubits. The atomic single-qubit rotations by $\pi/2$ and $-\pi/2$ are described by the operators $\frac{1}{\sqrt{2}}\left(\begin{smallmatrix}1 & 1\\ -1 & 1\end{smallmatrix}\right)$ and $\frac{1}{\sqrt{2}}\left(\begin{smallmatrix}1 & -1\\ 1 & 1\end{smallmatrix}\right)$, respectively, in the basis $\{|\downarrow\rangle, |\uparrow\rangle\}$. The atom-photon CZ gate is described

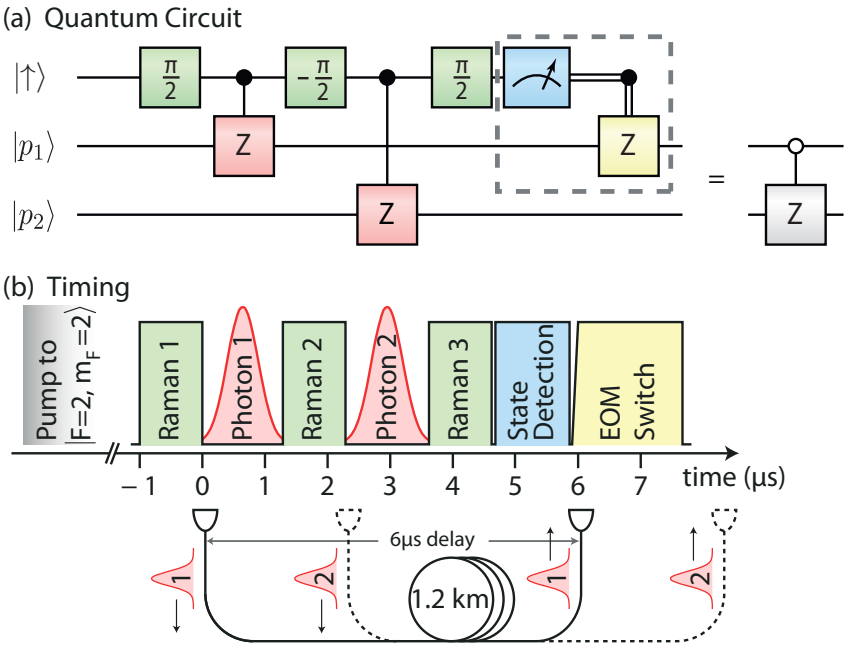

Figure 4.1.: The photon-photon gate mechanism. (a) Quantum circuit diagram. The sequence of CZ gates between the atomic ancilla qubit and the gate photons interleaved with rotations on the atomic qubit acts as a pure CPHASE gate on the input photon state $|p_1 p_2\rangle$. The dashed box is equivalent to the reflection-based quantum CZ gate of the original proposal via the principles of deferred and implicit measurement [10]. (b) Pulse sequence showing the timing of the experimental steps of the gate protocol. A delay fiber of 1.2 km length is used to store the gate photons for 6 µs. (from [96])

by $U_{ap} = \mathrm{diag}(1,1,1,-1)$ in the basis $\{|{\downarrow}\mathrm{L}\rangle, |{\downarrow}\mathrm{R}\rangle, |{\uparrow}\mathrm{L}\rangle, |{\uparrow}\mathrm{R}\rangle\}$. Any input state of the two photonic qubits, including entangled states, can be written as

$$|p_1 p_2\rangle = c_{\mathrm{LL}}|\mathrm{LL}\rangle + c_{\mathrm{LR}}|\mathrm{LR}\rangle + c_{\mathrm{RL}}|\mathrm{RL}\rangle + c_{\mathrm{RR}}|\mathrm{RR}\rangle \ , \tag{4.1}$$

defined by the four complex numbers c_{LL}, c_{LR}, c_{RL} and c_{RR}. Henceforth, we will use the compact notation $|ll\rangle := c_{\mathrm{LL}}|\mathrm{LL}\rangle$, $|lr\rangle := c_{\mathrm{LR}}|\mathrm{LR}\rangle$, $|rl\rangle := c_{\mathrm{RL}}|\mathrm{RL}\rangle$, and $|rr\rangle := c_{\mathrm{RR}}|\mathrm{RR}\rangle$. Therefore, any photon-photon gate operation starts in the collective initial state

$$|{\uparrow}\rangle(|ll\rangle + |lr\rangle + |rl\rangle + |rr\rangle) \ . \tag{4.2}$$

The first $\pi/2$ rotation brings the atom into a superposition

$$\tfrac{1}{\sqrt{2}}(|{\downarrow}\rangle + |{\uparrow}\rangle)(|ll\rangle + |lr\rangle + |rl\rangle + |rr\rangle) \ , \tag{4.3}$$

followed by a CZ-interaction between the atom and the first photon, which flips the sign of all states with the atom in $|{\uparrow}\rangle$ and the first photon in $|\mathrm{R}\rangle$:

$$\tfrac{1}{\sqrt{2}}\big((|{\downarrow}\rangle + |{\uparrow}\rangle)(|ll\rangle + |lr\rangle) + (|{\downarrow}\rangle - |{\uparrow}\rangle)(|rl\rangle + |rr\rangle)\big) \ . \tag{4.4}$$

Subsequent rotation of the atom by $-\pi/2$ creates the state

$$|{\uparrow}\rangle(|ll\rangle + |lr\rangle) + |{\downarrow}\rangle(|rl\rangle + |rr\rangle) \ . \tag{4.5}$$

Reflection of the second photon flips the sign of all states with the atom in $|{\uparrow}\rangle$ and the second photon in $|\mathrm{R}\rangle$:

$$|{\uparrow}\rangle(|ll\rangle - |lr\rangle) + |{\downarrow}\rangle(|rl\rangle + |rr\rangle) \ . \tag{4.6}$$

The final rotation of the atom by $\pi/2$ yields

$$\tfrac{1}{\sqrt{2}}\big((|{\uparrow}\rangle + |{\downarrow}\rangle)(|ll\rangle - |lr\rangle) \ + \ (|{\downarrow}\rangle - |{\uparrow}\rangle)(|rl\rangle + |rr\rangle)\big) \ . \tag{4.7}$$

At this point the state of the atom is measured. There are two equally probable outcomes projecting the two-photon state accordingly:

$$\begin{aligned} |{\downarrow}\rangle\text{:} \quad & |ll\rangle - |lr\rangle + |rl\rangle + |rr\rangle \ , \\ |{\uparrow}\rangle\text{:} \quad & |ll\rangle - |lr\rangle - |rl\rangle - |rr\rangle \ . \end{aligned}$$

Following detection of the atom in $|{\uparrow}\rangle$, an additional π phase is imprinted on the $|\mathrm{R}\rangle$-part of the first photon by applying the feedback, i.e. a sign flip on $|rl\rangle$ and $|rr\rangle$, whereas the photonic state is left unaltered upon detection of $|{\downarrow}\rangle$. Thereby, the final photonic state becomes

$$|ll\rangle - |lr\rangle + |rl\rangle + |rr\rangle \ , \tag{4.8}$$

independent of the outcome of the atomic state detection. It differs from the input state (Eq. (4.2)) by a minus sign on $|lr\rangle$ only. Hence, the total circuit acts as a pure photonic CPHASE gate:

$$\begin{aligned} |\mathrm{LL}\rangle &\to |\mathrm{LL}\rangle & \qquad |\mathrm{RL}\rangle &\to |\mathrm{RL}\rangle \\ |\mathrm{LR}\rangle &\to -|\mathrm{LR}\rangle & \qquad |\mathrm{RR}\rangle &\to |\mathrm{RR}\rangle \end{aligned} \tag{4.9}$$

Here the phase shift occurs for the first photon in $|\mathrm{L}\rangle$ and the second one in $|\mathrm{R}\rangle$, so the control qubit is inverted with respect to a canonical CPHASE, as indicated by the open circle in the final circuit diagram of Fig. 4.1(a).

To apply this scheme in practice, the qubits have to be stored and controlled in an appropriately timed sequence: After the first photon p_1 is reflected, it directly enters a 1.2 km

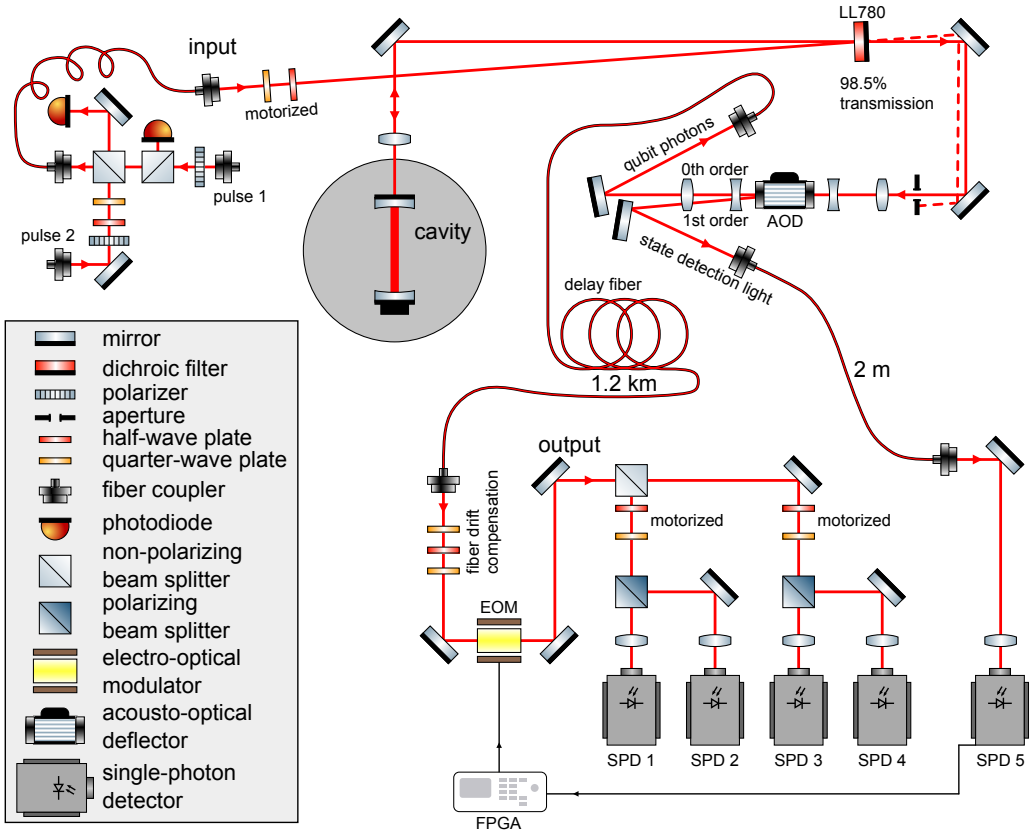

Figure 4.2.: Optical setup for the photon-photon gate. Qubit-carrying weak coherent photon pulses are combined on the left and coupled into the cavity beam path through the LL780 dichroic filter, which behaves as a 98.5% transmitting beam splitter. On the upper right, the cavity output beam is switched between delay fiber and direct detection. The lower part shows the output detection setup, where photons can be analyzed in two independent polarization bases. Additional components for cavity locking and atom trapping and manipulation, left out here for clarity, are shown in Fig. 3.2.

delay fiber (Sec. 4.2.1). The delay time of 6 µs is sufficient to allow for the reflection of both photons from the cavity, two coherent spin rotations, and state detection on the atom (Fig. 4.1(b)). The two photon wave packets are in independent spatio-temporal modes which can in principle be arbitrarily shaped. The only requirement is that the frequency spectrum should fall within the acceptance bandwidth of the cavity (0.7 MHz for $\pm 0.1\pi$ phase shift accuracy, according to Eq. (2.29)). We used Gaussian-like intensity profiles of 0.6 µs full width at half maximum (FWHM) within individual time windows of 1.3 µs width. Those pulses have a Fourier-limited FWHM bandwidth of 0.7 MHz, which fulfills the requirement.

4.2. Experimental Setup for the Photon-Photon Gate

The setup for the photon-photon gate consists of three parts: Preparation of input qubit photons, the gate itself (including cavity, delay fiber, switch and feedback electro-optic modulator (EOM)), and analysis of output qubits. Figure 4.2 shows the optical elements and beam paths.

The input part is on the left, where the two temporally separated input photons with independent polarizations are combined on a beam splitter. For the lack of a high-quality

real single-photon source, the gate was probed with weak coherent pulses of mean photon number $\overline{n} = 0.17$, and the presence of a photon was heralded afterwards with single-photon detector (SPD)s. The choice of $\overline{n}$ is a compromise between measurement time and measured gate fidelity. While lowering $\overline{n}$ reduces the data rate because of the high probability of zero-photon events in either of the two photon modes, increasing $\overline{n}$ raises the multi-photon probability per pulse thereby deteriorating the measured gate fidelity (see Sec. 4.3.5).

The input pulses are sent to the cavity through a 98.5% transmitting beam splitter (LL780 in Fig. 4.2), which discards most of the input light, but preserves most of the back-reflected output. Ideally, a polarization-independent circulator would preserve 100% of input and output light at this position, but to date the best available devices for 780 nm light only have transmissions up to 83%, which is not as good as the beam-splitter for the output direction. In this experiment the output direction is most relevant, because losses on the input can be compensated by a higher initial beam intensity. When the gate will be applied to process qubits from a preceeding quantum computation, both losses will matter.

After the cavity reflection, the photons pass a path switch (implemented by an acousto-optic deflector (AOD)), a delay fiber and a polarization-dependent phase shifter (implemented by an EOM), which finishes the action of the gate. Finally the photons are measured on four SPDs (SPCM-AQR from Perkin Elmer with ≈50% efficiency), two pairs that project on two independent polarization bases. The routing of each photon to the two bases is random through a non-polarizing beam splitter (NPBS). A valid gate output is recorded whenever one photon click arrives in each of the two time windows.

4.2.1. Delay Fiber

To realize the backaction of the second photon onto the first one, at least the first one has to be stored for a finite time interval. This time interval (Fig. 4.1(b)) must include the length of both photon wavepackets, two atomic $\pi/2$ spin rotations and the state detection of the atom. Storage of a photonic qubit requires a quantum memory [124, 125]. In terms of complexity and storage fidelity, the best available memory today is still an optical fiber.

The applied single-mode fiber (780HP from Nufern) has a length of 1.2 km, a delay time of 5.92 µs and a total transmission of 40% (including in-coupling efficiency). This corresponds to a loss of 3.3 dB/km and a $1/e$ storage efficiency decay time of 6.5 µs at the 780 nm wavelength. The chosen fiber length is a tradeoff between available time for the steps of the experiment and efficiency-reducing photon loss.

In order to transmit qubits of any polarization, the fiber was non-polarization-maintaining (non-PM), because polarization-maintaining (PM) fibers are only suited to maintain two distinct linear polarizations. The non-PM fiber has a temperature-dependent polarization drift, which can be significant due to the great fiber length. Stored inside the temperature-stabilized setup (Sec. 3.11) polarization drifts were about 5°/h. Hence, a manual compensation with three free-space waveplates (Fig. 4.2 after the fiber) once every half an hour kept the polarization error within acceptable limits.

4.2.2. Optical Path Switching

In the experimental setup (Fig. 4.2), both the qubit photons and the light from atomic state detection leave the cavity on the high transmission side. But the protocol (Fig. 4.1) requires a state detection after the second photon reflection and before the photons leave the setup through the feedback phase shifter (Sec. 4.2.4). Therefore the optical paths of signal photons and state-detection light have to be actively routed with a switch.

A suitable switch has to be fast (below microsecond timescale), absorb very little light, not distort the geometric mode required for coupling into single-mode fibers and leave the qubit-encoding polarization undisturbed. To date, such a switch is not yet available off the shelf. Two options were investigated: First, an optical chopper disk, made from an old hard disk drive that was gold-coated and used in previous experiments [83]. The disk rotates with 7200 rpm and has a hole pattern that alternates between reflection and transmission every 200 µs. With a well-focused beam, the switching time between full transmission and full reflection is 2 µs. The transmission is close to 100% and the measured reflection off the gold surface reaches up to 87%. Those parameters are sufficient for the gate, when the switching is done during the third atomic state rotation pulse (Fig. 4.1). However, when the disk was mounted on the main experiment table, it caused significant vibrations that disturbed the cavity lock to an unacceptable amount. Besides the main vibration frequency of 120 Hz, the cavity was shaking with a broad spectrum of mechanical vibrations in the few kilohertz range. This would lead to strong variations in the cavity-induced optical phase shift (such as shown in Sec. 5.9.5), and degrade the overall performance of the gate.

Therefore, a second option, an AOD, was chosen (upper right in Fig. 4.2). The AOD can efficiently deflect an optical beam inside its crystal via Bragg diffraction off a switchable (radio-frequency) sound wave. The chosen AOD, ATD-1501A2 from IntraAction achieved a transmission of 97.6% in the zeroth order direction for the qubit photons and 82% for the first-order diffracted direction, which was used for state detection. The coupling efficiencies to single-mode fibers were 84% for the zeroth order and 89% for the first order. The use of an AOD raises several experimental challenges: First of all, the AOD has an undesirable polarization dependent absorption and acts like a partial polarizer. The polarization-dependent absorption fraction was measured as 0.5% in zeroth order and 1% in first order, which is still acceptable. Second, a high first-order deflection efficiency requires very careful three-dimensional geometric alignment and high radio-frequency power of 2 W for switching. The dissipated power heats the AOD crystal and leads to geometric mode distortion as well as time-dependent birefringence at a measured rate of $\approx 10°/\mathrm{s}$. These problems can be avoided when the AOD runs at a very low duty cycle of 1.2 µs (for the state detection) within each experimental cycle of 2 ms, such that only little heat is dissipated on average and polarization changes stay below 2%. The switching time, limited by the optical beam diameter and the speed of sound in the AOD crystal, is below 0.1 µs.

4.2.3. Fast Atomic State Detection

The photon-photon gate protocol requires a measurement of the atomic state and a corresponding feedback to the polarization of the first photon, before that photon leaves the gate. Therefore the state detection needs to finish in around one microsecond, three times faster than previous experiments in the setup [70, 126]. To discriminate the atomic states $|\uparrow\rangle$ and $|\downarrow\rangle$, a cavity-resonant beam on the $|\uparrow\rangle \leftrightarrow |\mathrm{e}\rangle$ transition irradiates the atom transversally to the cavity. This performs a projective measurement of the spin state. In case of $|\uparrow\rangle$, many photons are scattered via the $|\uparrow\rangle \leftrightarrow |\mathrm{e}\rangle$ transition and most of them – through Purcell enhancement – into the cavity mode. In case of $|\downarrow\rangle$, the laser light is far-detuned and no photon gets scattered. Figure 4.3(a) shows the SPD count rate in case of $|\uparrow\rangle$ vs. incident laser power. Here, the saturation power is 1.7 µW and the asymptotic maximum count rate after losses, fiber coupling and finite detection efficiency is 4.8 cts/µs. An increased state-detection power causes significant heating of the atom, such that the trapping time reduces to few seconds at the saturation power, even if the duty cycle of the state detection is low. As a compromise between count rate and trapping time, a power of 3.5 µW with a count rate of 3.2 cts/µs was chosen.

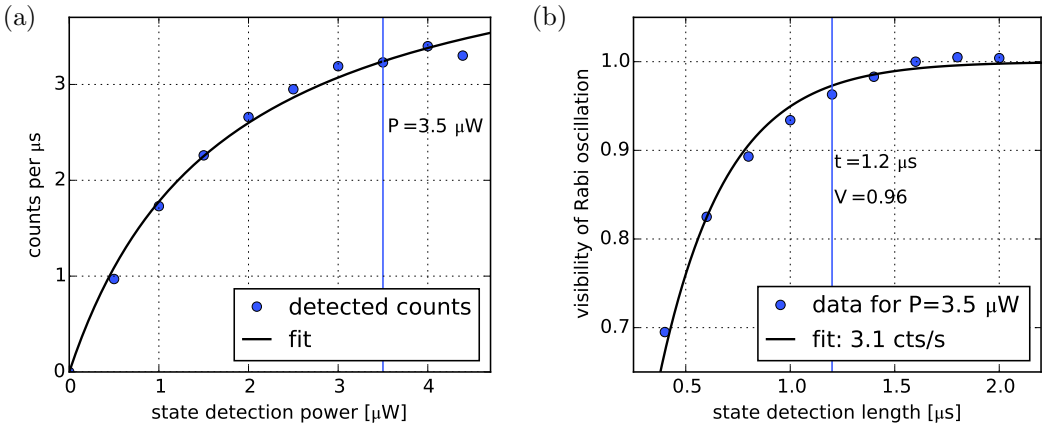

Figure 4.3.: Parameter-dependence of the state detection. (a) Rate of detected state detection photons vs. power of the state-detection beam (with a 34 µm beam waist). The solid curve is a fitted saturation model. (b) Visibility of an atomic Rabi oscillation with respect to the length of the state-detection interval. The visibility is limited by the small number of state-detection counts. At the chosen value of 1.2 µs for the gate (blue line), the visibility and therefore the fidelity of the state detection is 96%. The solid line is a fitted exponential curve, representing the expected probability to obtain at least one state-detection photon from a Poissonian number distribution.

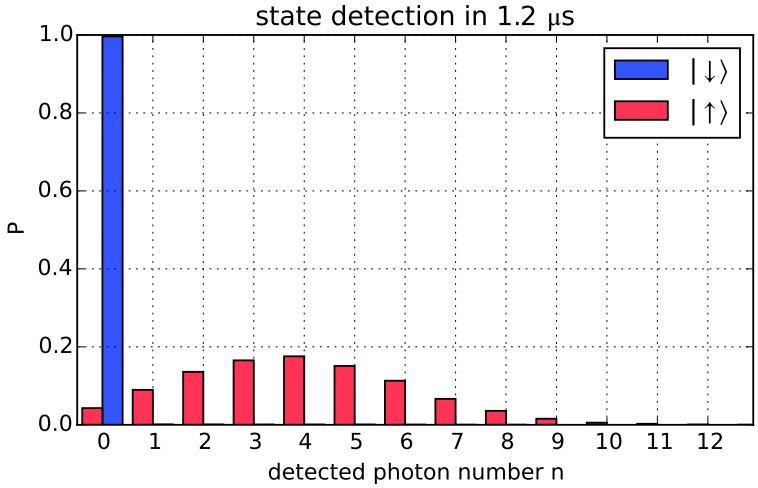

Figure 4.4.: State-detection histogram. Distribution of the number of detected photons within 1.2 µs when the atom was prepared in the states $|\downarrow\rangle$ and $|\uparrow\rangle$, respectively. The discrimination threshold was set between 0 and 1 photons. The state-detection fidelity is 96%, limited by the relatively low average photon number in the $|\uparrow\rangle$ case.

The second adjustable parameter is the length of the state-detection interval, which is proportional to the mean number of scattered photons. Figure 4.3(b) shows the visibility of Rabi-oscillations of the atom between $|\uparrow\rangle$ and $|\downarrow\rangle$, which is in this case determined by the probability to have at least one photon in the state detection of $|\uparrow\rangle$. At the chosen interval length of 1.2 µs, the visibility reaches 96%, and the remaining 4% are sacrificed to save time. On average, the state detection of $|\uparrow\rangle$ yields 4.0 photons with near-Poissonian distribution (Fig. 4.4). In case of $|\downarrow\rangle$, the state detection yields no photons in 99.6% of all cases, limited by imperfect state preparation.

4.2.4. Phase Feedback

The last step in the gate protocol is a controlled phase (CZ) gate with classical control. The classical control is the state-detection outcome of the atom with two possible bit states $|\uparrow\rangle$ and $|\downarrow\rangle$. The photon counts are evaluated in real-time by an FPGA, which discriminates the two possibilities "no counts" or "at least one count". The result controls a Z-gate, a conditional π phase shift on one polarization relative to the orthogonal one, equal to an optical half-wave plate. A controllable phase shifter is implemented by an EOM, based on the Pockels effect, where the retardation of the optical wave is controlled by a static electric field. We chose a Linos "LM202 PHAS" modulator with a KD*P crystal and an aperture of $3 \times 3\,\mathrm{mm}^2$. This EOM has a transmission of 96%.

Since the required half-wave voltage of 284 V is high, fast switching times require a very low capacitance (≈100 pF) and thus a short cable between EOM and the high-voltage supply. After testing several EOMs and cables, suitable switching times were achieved. The main transition edge lasts only 20 ns. However, there are so-called piezo oscillations on a timescale of 0.1 µs (Fig. 4.5(b)) and smaller polarization drifts for a few microseconds (Fig. 4.5(a)). The EOM is only active while the first photon exits the gate (5.9 µs to 7.2 µs) and must reset before the second photon exits (8.2 µs to 9.5 µs). Thus, both transition edges in Fig. 4.5(a) matter, and the polarization gets distorted by a few percent.

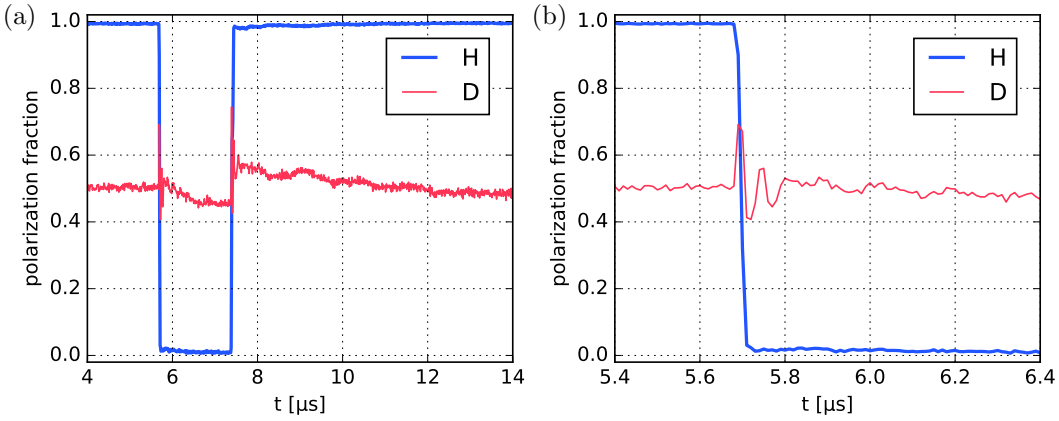

Figure 4.5.: Switching behavior of the Electro-optical modulator. To perform a classical polarization Z-gate, the EOM has to act like a switchable half-wave plate, where one linear polarization (here $|\mathrm{D}\rangle$, mapped to $|\mathrm{R}\rangle$ in the experiment) gets an optical π-phase with respect to the orthogonal polarization $|\mathrm{A}\rangle$. An $|\mathrm{H}\rangle$-polarized input should be switched between $|\mathrm{H}\rangle$ and $|\mathrm{V}\rangle$, and its projection on $|\mathrm{D}\rangle$ should remain 50%. Here, immediately after switching (at 5.7 µs and 7.4 µs), the phase oscillates with an amplitude of 0.1π at a 0.1 µs timescale (b) and then drifts by 0.04π for a few microseconds (a).

Table 4.1.: Behavior of a polarization CPHASE gate in different bases. All linear polarizations behave similar to the $|H\rangle/|V\rangle$ states. Intermediate elliptical polarizations result in a partially-entangling gate.

Input	$\|R\rangle/\|L\rangle$	$\|H\rangle/\|R\rangle$	$\|D\rangle/\|A\rangle$
$\|R\rangle/\|L\rangle$	CPHASE	CNOT	CNOT
$\|H\rangle/\|V\rangle$	CNOT	entangling	entangling
$\|D\rangle/\|A\rangle$	CNOT	entangling	entangling

4.3. Photon-Photon Gate Results

The action of a quantum gate on input qubits is described as a gate matrix. In case of the CPHASE and CNOT two-qubit quantum gates the gate matrices are:

$$\text{CPHASE:} \begin{pmatrix} 1 & 0 & 0 & 0 \\ 0 & 1 & 0 & 0 \\ 0 & 0 & 1 & 0 \\ 0 & 0 & 0 & -1 \end{pmatrix} \qquad \text{CNOT:} \begin{pmatrix} 1 & 0 & 0 & 0 \\ 0 & 1 & 0 & 0 \\ 0 & 0 & 0 & 1 \\ 0 & 0 & 1 & 0 \end{pmatrix} \tag{4.10}$$

From a quantum-information perspective, the two are almost equivalent, because a single-qubit rotation before and after the gate can convert one into the other [10]. The actual type of such a gate depends then on the chosen basis. The natural qubit basis for the photon-photon gate is the $|R\rangle/|L\rangle$-basis of right- and left-handed circular polarization, because $|R\rangle$ couples to an atomic transition, whereas $|L\rangle$ does not (Fig. 3.3). In this basis, the gate is a CPHASE, which is symmetric in both qubits. The behavior in other canonical bases is listed in Table 4.1. With one of the photons being circularly and the other one linearly polarized, the gate will act as a CNOT gate with the circular qubit being the control and the linear one being the target qubit that gets conditionally flipped. When both photons enter in linear polarization states, the gate will turn the two separable inputs into a maximally entangled state.

4.3.1. CNOT Operation

The CNOT operation is the quantum analog to an exclusive-OR (XOR) logic gate. One qubit (the target) will flip depending on the state of the other (the control), which will keep its state. Which of the two qubits is control and target depends on the chosen basis of input states, not on the gate itself. For separable input states from a CNOT basis set, the expected gate output is also a separable state from the same basis set. The experimental behavior is therefore captured in a truth table, where the probabilities for each of the four possible output states are measured for each of the four input states.

Figure 4.6 shows the truth tables for four different bases with a CNOT behavior: (R/L $\otimes$ H/V), (R/L $\otimes$ D/A), (H/V $\otimes$ R/L) and (D/A $\otimes$ R/L). Each truth table exhibits the expected behavior: The circular (control) qubit is preserved and the linear (target) qubit is conditionally flipped.

One basis (R/L $\otimes$ H/V), was measured with larger statistics of 802 detected photon pairs an has an average overlap with the ideal CNOT of

$$F_{\text{CNOT}} = (76.9 \pm 1.5)\% \,. \tag{4.11}$$

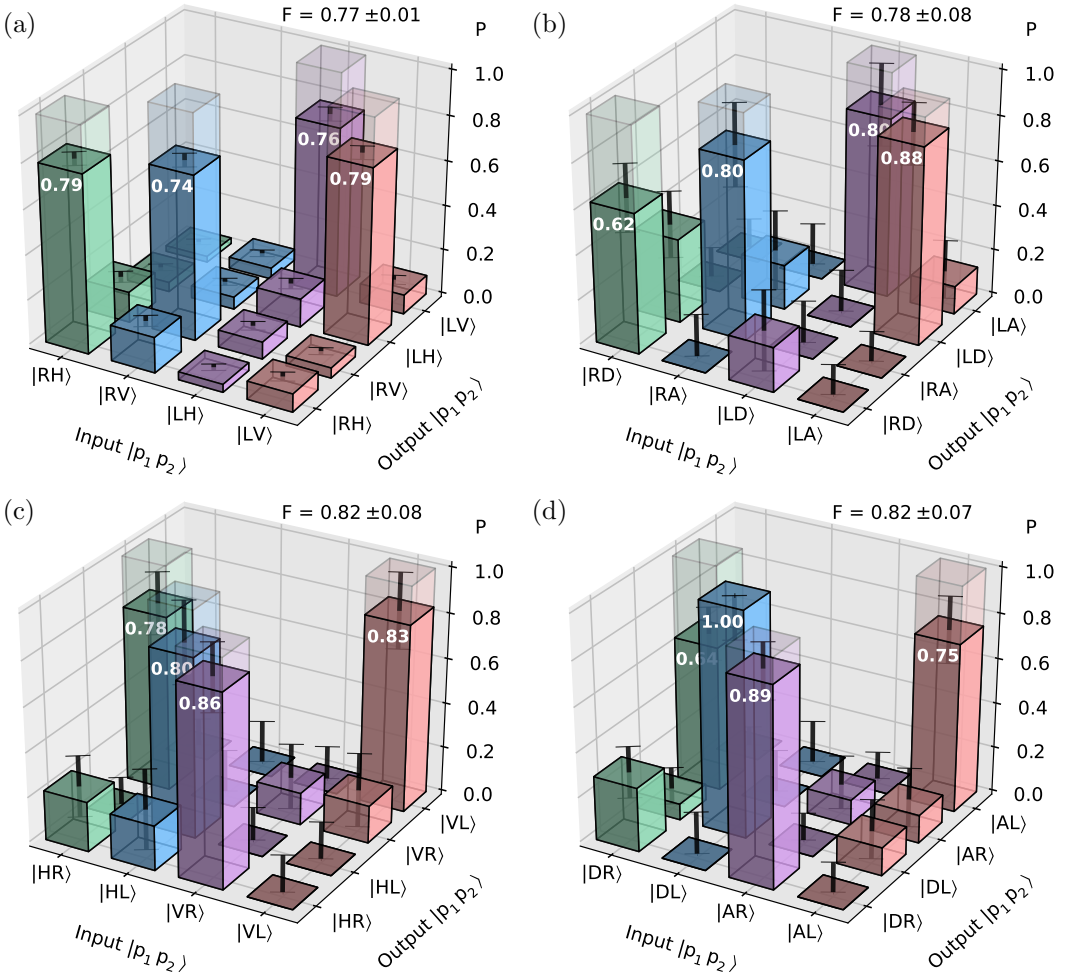

Figure 4.6.: Truth tables in four possible CNOT bases. (a) R/L ⊗ H/V, (b) R/L ⊗ D/A, (c) H/V ⊗ R/L and (d) D/A ⊗ R/L. The expected CNOT behavior is observed in each basis. The CNOT gate flips the linear polarization of the target photon whenever the control photon has a certain circular polarization. The vertical axis gives the probability to measure a certain output state given the designated input state. The truth table for ideal CNOT gates is indicated by the light transparent bars with P = 1. The black T-shaped bars represent statistical errors on each entry, computed via linear error propagation assuming independent photon statistics. ((a) from [96])

Apparently the gate errors on the target qubit are larger than on the control qubit. This is expected when the gate fails in a small fraction of trials, for example due to imperfect geometric mode matching of the photons to the cavity (Sec. 3.9). In such cases, the target is not flipped, but the control remains in the correct state.

4.3.2. Entangling Gate

The decisive property of a quantum gate that distinguishes it from its classical counterpart is the capability to generate entanglement [5] from a separable input. For both input photons in a linear polarization state, the gate ideally creates a maximally entangled state. The experimental output state is quantified in terms of a density matrix, that is obtained from projective measurements in various bases and tomographical reconstruction [50]. Tomography is an inverse problem: While quantum mechanics predicts the probability of a

measurement outcome when the state (density matrix) is given, the tomography should infer the original state from a set of measurement outcomes. A popular algorithm for state reconstruction is maximum likelihood (ML) estimation [127]. It determines the state, which produces the largest likelihood of obtaining the results that were actually measured. ML has some important properties [128], such as a very efficient use of the available information and the application of physical constraints. However, in some cases, it may be biased [129], most severely for small sample sizes. For this reason a second, unbiased algorithm was also applied, namely linear inversion. That scheme uses the pseudoinverse of the matrix that determines measurement probabilities from a density matrix. The result is a density matrix that depends linearly on the relative frequencies of measurement outcomes. However, due to statistical noise, that result may sometimes be unphysical, for instance exhibiting negative eigenvalues.

One entangling gate operation is demonstrated for an input of two diagonally polarized photons $|\mathrm{DD}\rangle$. The theoretical gate matrix (Eq. (4.9)) with the definitions of Eq. (2.5) predicts an output of

$$|\psi_{\mathrm{out}}\rangle = \frac{i}{\sqrt{2}}(|\mathrm{DL}\rangle + |\mathrm{AR}\rangle) =: |\Psi^+\rangle \,, \tag{4.12}$$

a maximally entangled Bell state in the (D/A $\otimes$ R/L) basis.

For this operation, 1378 processed photon pairs were collected at the gate output. The detection bases were randomized between the 3×3 two-qubit bases $(\mathrm{R/L, H/V, D/A})^2$, which are tomographically complete. Every valid measurement outcome of two photon clicks gives one of four possible measurement outcomes in the respective basis. The following clicks were collected:

$p_1\downarrow$ / $p_2\rightarrow$	R	L	H	V	D	A
R	75	49	37	42	**67**	5
L	70	48	21	22	11	**43**
H	45	23	31	**89**	36	17
V	28	34	**84**	26	33	21
D	12	**53**	23	30	56	35
A	**46**	8	24	20	65	49

Here the three diagonal blocks have a higher total number of counts, because of the additional chance that both photons are detected in the same detector pair of the detection setup (Fig. 4.2). The bold numbers indicate the results that should include all clicks from their block in case of the ideal state of Eq. (4.12). The six other blocks should each have a uniform distribution with multinomial statistical variations.

The reconstructed density matrix ρ (through linear inversion) for these data is depicted in Fig. 4.7. It turns out that the density matrix is actually physical (no negative eigenvalues) and close to the ML reconstruction (less than 2% difference in its entries). The error bars on ρ are obtained through linear error propagation [128] from the covariance matrix of multinomially distributed counts.

The density matrix has a fidelity $F_{\Psi^+} = \langle\Psi^+|\rho|\Psi^+\rangle = (72.9 \pm 2.8)\%$ with the ideal Bell state (unbiased linear estimate). The total data set can be separated into two subsets of equal size corresponding to the outcome of the atomic state detection being $|\downarrow\rangle$ or $|\uparrow\rangle$. The respective fidelities are $F^{\downarrow}_{\Psi^+} = (74.4 \pm 3.9)\%$ and $F^{\uparrow}_{\Psi^+} = (71.5 \pm 4.2)\%$, i.e. the gate works comparably well in both cases.

The output state ρ is significantly entangled with a negativity [130] of $\mathcal{N} = 0.242 \pm 0.028$ (where $\mathcal{N} = 0$ for an unentangled state and $\mathcal{N} = 0.5$ for a maximally entangled state).

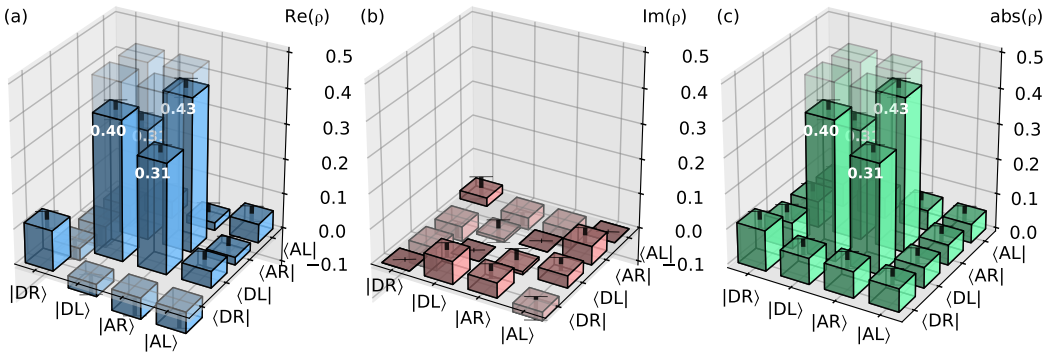

Figure 4.7.: Reconstructed density matrix of the entangled two-photon state created by the gate from the separable input state $|\mathbf{DD}\rangle$. Depicted are the real (a) and imaginary (b) parts and modulus (c) of the elements of the density matrix. The light transparent bars indicate the ideal density matrix for $|\Psi^+\rangle$ in the chosen basis. Statistical errors on each entry (RMS 2.4%) are drawn as black T-shaped bars. (from [96])

The generation of an entangled state from a separable input state directly sets a non-tight bound for the entanglement capability (smallest eigenvalue of the partially transposed density matrix) [131] of the gate, $\mathcal{C} \leq -0.242 \pm 0.028$, which is -0.5 for the ideal CPHASE gate and where a negative $\mathcal{C}$ denotes that the gate is entangling. Note that here $\mathcal{C} = -\mathcal{N}$, because the partially transposed of ρ has exactly one negative eigenvalue.

4.3.3. Average Gate Fidelity

Another meaningful measure of the gate performance is the average gate fidelity $\overline{F}$, which can be obtained as the average fidelity of 6×6 output states generated from the input states on all canonical polarization axes (H, V, D, A, R, L) with the theoretically expected ideal outcomes [132]. All 36 state fidelities were estimated linearly and bias-free with randomized tomographically complete basis settings. Although only insignificant statistics of 80 detected photon pairs were collected on each of the output states, their combination gives a well-determined value of $\overline{F} = (76.2 \pm 3.6)\%$. The deviation from unity is well understood from the technical imperfections discussed in Sec. 4.4. Average fidelities for subsets of different types of operations are $\overline{F}_{\mathrm{CPHASE}} = (86 \pm 10)\%$, $\overline{F}_{\mathrm{CNOT}} = (77 \pm 7)\%$ and $\overline{F}_{\mathrm{entangling}} = (73 \pm 8)\%$, perfectly in line with the individual measurements in previous sections.

4.3.4. Experimental Efficiency

The efficiency of the photon-photon gate, which is the combined transmission probability for two photons, is unity for the ideal scheme, but gets reduced by several experimental imperfections. It is polarization-independent because all optical elements including the cavity have near-equal losses for all polarizations. The two main loss channels are the long delay fiber (transmission $T = 40.4\%$) (Sec. 4.2.1) and the limited cavity reflectivity on resonance ($R = 67\%$, both for the case of a coupling and a non-coupling atom) (Sec. 2.5). All other optical elements have a combined transmission of 81%, dominated by the fiber-coupling efficiency and absorption of the AOD switch (Sec. 4.2.2). This yields a total experimental gate efficiency of $\eta_{\mathrm{gate}} = (22\%)^2 = 4.8\%$, where the single-photon transmission probability is squared to account for both photons. Despite the transmission losses, which are characteristic for all photonic devices, the protocol itself is deterministic. The largest

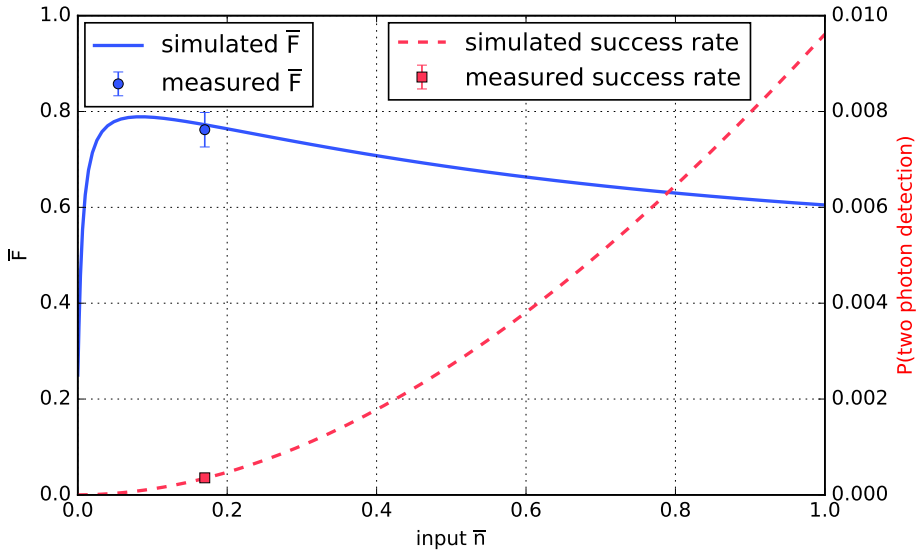

Figure 4.8.: Dependency of experimental fidelity and success rate on the average coherent state input photon number $\overline{n}$. The simulated average gate fidelity (blue curve) reaches an optimum of $\overline{F}_{\max} = 79\%$ at $\overline{n} = 0.1$. For lower $\overline{n}$, detector dark counts dominate, for higher $\overline{n}$, multi-photon contributions become relevant. The success rate to receive one photon in each time window of the two gate photon pulses at the detector rises quadratically with $\overline{n}$ (dashed curve, right scale). The chosen $\overline{n} = 0.17$ (markers) is a compromise between larger $\overline{F}$ and larger success rate.

potential improvement is offered by eliminating the fiber-induced losses, for instance by a free-space delay line, a delay cavity or an efficient optical quantum memory [124, 125].

4.3.5. Influence of the Average Input Photon Number

The photon-photon gate is designed to operate on two single input photons. In the experiment, good single photons were not available, and the gate was tested with coherent pulses. Coherent pulses contain a Poissonian photon-number distribution $P(n) = \overline{n}^n e^{-\overline{n}}/n!$ (Eq. (2.35)). When $\overline{n}$ is small, the distribution is dominated by the vacuum component, and higher photon numbers are suppressed increasingly. In a heralded operation, where only events are evaluated in which a photon is successfully detected, the zero-photon component is eliminated and the conditioned distribution approximates a single photon. However, since $P(2)/P(1) = \overline{n}/2$, the fraction of undesired two-photon components in each pulse increases with larger $\overline{n}$ and degrades the measured gate fidelity, as the phase flip $(-1)^n$ (Eq. (2.37)) is reverted by the second photon. The measured fidelity is then lower than the intrinsic fidelity for a single-photon input.

However, at smaller values of $\overline{n}$ the experimental success rate

$$P(\text{two photon detection}) \simeq (\overline{n} \cdot \eta_{\text{SPD}})^2 \cdot \eta_{\text{gate}} \tag{4.13}$$

decreases, where the experimental gate efficiency is $\eta_{\text{gate}} = 4.8\%$ and the single-photon detector efficiency is $\eta_{\text{SPD}} \approx 50\%$. Additionally, when $\overline{n}$ is too small, detector dark counts with a fixed rate of around $3.6 \cdot 10^{-4}$ per pulse become dominant. Figure 4.8 shows this behavior, simulated with all known imperfections (Sec. 4.4). At the chosen $\overline{n} = 0.17$ the measurable average gate fidelity $\overline{F}$ is close to the best achievable value and the heralding probability of $4 \cdot 10^{-4}$ per attempted gate operation is still acceptable.

Table 4.2.: Experimental imperfections in the photon-photon gate. Reductions in the fidelity the entangled photon-photon state produced by the gate. Each individual stated error is for an otherwise perfect system. The numbers do not add up linearly.

Imperfection	Reduction in F
Two-photon contributions	12%
Photon bandwidth	6%
Atomic state imperfections	6%
Cavity characteristics	5%
Detector dark counts	2%
Other optical elements	2%

4.4. Photon-Photon Gate Imperfections

To understand the imperfections encountered in the experiment, I have set up a model of both photonic qubits and the atomic ancilla qubit in terms of their three-particle density matrix ρ, numerically implemented with the Python software library "QuTiP" [133]. Under ideal conditions, the density matrix transforms via sequential unitary transformations U as $\rho \to U\rho U^\dagger$, and known error sources can be introduced at each specific step. Finally, the fidelity of ρ with the desired target state is calculated for comparison with experimental values. Table 4.2 lists the reductions in fidelity that each individual effect would introduce to an otherwise perfect gate.

In this scenario, an unnoticed, incorrect preparation of the atom in 2% of the cases creates an incoherent admixture of the wrong initial state. Errors in the atomic state detection (Sec. 4.2.3) lead to an exchange of the photonic submatrices corresponding to each atomic state. Detector dark counts are modeled as an admixture of a fully mixed state and decoherence effects are taken into account as reductions in off-diagonal elements of ρ. Cases where photons do not enter the cavity because of geometric mode mismatch are included with a phase shift of zero. Zero- and multi-photon components are modeled in truncated Fock space, where the phase-shift operator $\hat{U}(\phi) = \exp(-i\phi\hat{n})$ puts a $n\phi$ phase onto each $|n\rangle$ component, and only the odd photon components get the desired π phase (Eq. (2.37)). Random fluctuations in some of the parameters enter the model by integrating the resulting density matrix over their distribution function.

The largest imperfection stems from using weak coherent pulses instead of true single photons to characterize the gate and is therefore not intrinsic to the performance of the gate itself. First, at the chosen $\overline{n} = 0.17$ there is a significant probability of having two photons in one qubit mode if it is populated. Second, the probability to have both qubit modes populated is small, such that detector dark counts of $3.6 \cdot 10^{-4}$ per pulse contribute to the measured data. The measured gate fidelity could therefore be improved by employing a true single-photon source.

The relatively short delay introduced by the optical fiber restricts the temporal windows for the photon pulses and atomic state detection. The resulting bandwidth of the photons causes random fluctuations in the phase shift (Eq. (2.29)). The obvious solution is to choose a longer delay. Further errors can be attributed to the characteristics of the optical cavity, the state of the atom, and other optical elements. The cavity has a polarization-eigenmode splitting of 410 kHz (Sec. 3.10) that could be eliminated by selecting mirrors with little intrinsic birefringence and by avoiding mechanical stress on the mirror substrates [95]. Neither the resonance frequency of the cavity (Sec. 3.8) nor the spatial overlap between its mode and the fiber mode (Sec. 3.9) are perfectly controlled. The latter could be improved with

additional or better optical elements. Fidelity reductions associated with the state of the atom are due to imperfect state preparation, manipulation and detection, and decoherence. Improvements are expected from the application of cavity-enhanced state detection to herald successful state preparation, Raman sideband cooling [84] to eliminate variations in the Stark shift of the atom, and composite pulses to optimize the state rotations. The limited precision of polarization settings and polarization drifts inside the delay fiber are the main contribution from other optical elements. The latter can be improved using active stabilization, which has been recently set up in our laboratory. With all this in mind, progress towards even higher fidelities is certainly feasible for future implementations.

4.5. Conclusion

The implemented photon-photon gate operates in the predicted way and achieves all the important benchmarks. It follows a deterministic protocol and could therefore be a scalable building block for new photon-processing tasks such as those required by quantum repeaters [134], for the generation of photonic cluster states [135] or quantum computers [136]. The gate's ability to entangle independent photons could be a resource for quantum communication [20]. Moreover, the gate could serve as the central processing unit of an all-optical quantum computer, envisioned to processes pairs of photonic qubits that are individually stored in and retrieved from an in principle arbitrarily large quantum cache. Such cache would consist of an addressable array of quantum memories, individually connected to the gate via optical fibers. Eventually, such architecture might even be implemented with photonic waveguides on a chip.

5. Creation of Schrödinger-Cat States

Some contents of this chapter have been published in [137]: **Deterministic creation of entangled atom-light Schrödinger-cat states**. B. Hacker, S. Welte, S. Daiss, A. Shaukat, S. Ritter, L. Li and G. Rempe. *Nature Photonics* **13**(2), 110–115 (2019)

In the previous chapter, we employed the particle nature of light, working with discrete single photons. Let us now turn to the second experiment, which focusses on the wave nature. The core of the experiment – an atom in a cavity – will remain the same. The different behavior of the light is mostly determined by the way we choose to measure it. In comparison to single photons, which were essentially treated as mere qubits, the wave picture is richer. Waves are described in terms of amplitude and phase, which are continuous variables [138] with an infinitely large Hilbert space.

A classical electromagnetic wave is defined by the spatial distribution of the electromagnetic field at a given point in time. The field at any point oscillates rapidly with an optical frequency f and has an envelope which is called *spatio-temporal mode*. To study the dynamics of such an *electromagnetic oscillator*, amplitude and phase are expressed in the two-dimensional *phase space* of variables q and p. These are analogous to position and momentum of a mechanical oscillator, but in the optical case q and p are on equal footing.

In the quantum-mechanical treatment, $\hat{q}$ and $\hat{p}$ are operators, the so-called *quadratures*. In terms of the more widespread photon annihilation and creation operators $\hat{a}$ and $\hat{a}^\dagger$, respectively, they are defined as [68]

$$\hat{q} = \frac{1}{\sqrt{2}}(\hat{a}^\dagger + \hat{a})\sqrt{\frac{\hbar}{m\omega}}\,, \qquad \hat{p} = \frac{i}{\sqrt{2}}(\hat{a}^\dagger - \hat{a})\sqrt{\hbar m\omega} \tag{5.1}$$

with the adoption of $\hbar = 1$ and $m\omega = 1$ throughout this chapter. Optical fields in phase space can be treated with all the tools of the well-studied *quantum harmonic oscillator*. $\hat{q}$ and $\hat{p}$ are conjugate variables with the canonical commutation relation $[\hat{q}, \hat{p}] = i$. Therefore they are subject to the Heisenberg uncertainty relation

$$\Delta\hat{q} \cdot \Delta\hat{p} \geq \frac{1}{2} \tag{5.2}$$

that prevents their precise simultaneous measurement.

5.1. The Wigner Function

In classical optics, the wave in one optical mode can have a well defined amplitude $|\alpha|$ and phase $\arg(\alpha)$, which is a single point in phase space. For a statistical ensemble the state is expressed by a phase space distribution function $W(q, p)$, which follows classical statistics. For instance, W is non-negative, the volume is normalized and the so-called *marginal distribution* $\mathrm{pr}(q)$ in one quadrature q is obtained by integration along p.

In the quantum-mechanical treatment, one can analogously define the *quasiprobability* distribution $W(q, p)$ [139], a real-valued function in phase space, which unambiguously defines

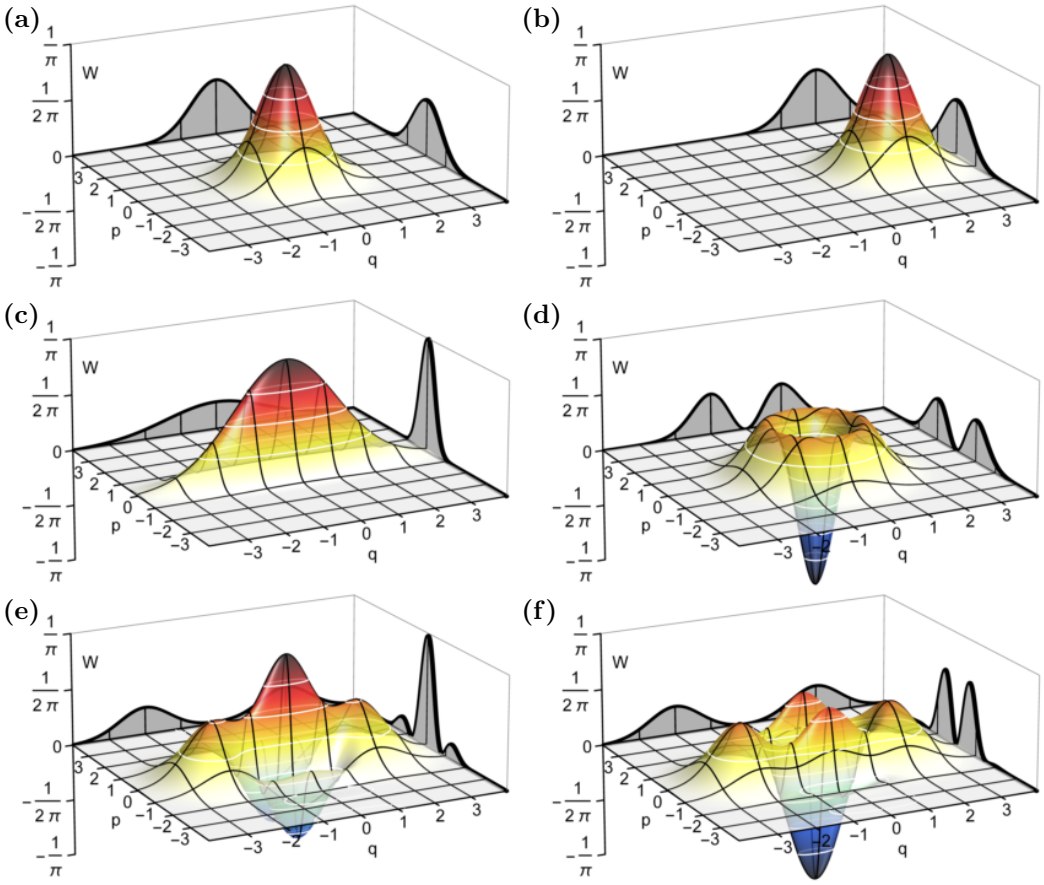

Figure 5.1.: Wigner functions $W(q,p)$ of various optical states. (a) Vacuum, (b) coherent state with $\alpha = \sqrt{2}$, (c) squeezed vacuum, (d) single-photon Fock state, (e) even cat state with $\alpha = \sqrt{2}$, (f) odd cat state with $\alpha = \sqrt{2}$ (described in Sec. 5.2). Two marginal distributions, the projections of W in q- and p-direction, which are measurable as voltage probability distributions, are drawn next to each Wigner function. Marginal distributions are strictly positive and their maximum value was scaled to the box height.

a state. W is one of a family of distribution functions, beside others such as the Husimi Q or the Glauber-Sudarshan P representation [68]. The Wigner function W is the one with the closest similarity to the classical probability distribution and is well suited to represent experimentally measured data.

One requires that the projection of the Wigner function along the direction $p_\varphi = -q\sin\varphi + p\cos\varphi$ onto $q_\varphi = q\cos\varphi + p\sin\varphi$ in phase space yields the marginal distribution $\mathrm{pr}_\varphi(q_\varphi)$ of one quadrature q_φ, just as in the classical case

$$\begin{aligned} \mathrm{pr}_\varphi(q_\varphi) &= \langle q|\hat{U}(\varphi)\,\rho\,\hat{U}^\dagger(\varphi)|q\rangle = \\ &= \int_{-\infty}^{\infty} W(q_\varphi\cos\varphi - p_\varphi\sin\varphi, q_\varphi\sin\varphi + p_\varphi\cos\varphi)\,\mathrm{d}p_\varphi \end{aligned} \tag{5.3}$$

where $\hat{U}(\varphi)$ is a rotation operator. This is called a *Radon transform* and it links $W(q,p)$ to the measurable distribution function $\mathrm{pr}_\varphi(q_\varphi)$.

From this requirement follows non-trivially the definition [139] of the Wigner function of a state with density matrix ρ as

$$W(q,p) = \frac{1}{\pi}\int_{-\infty}^{\infty} e^{2ipx}\langle q-x|\rho|q+x\rangle\,\mathrm{d}x\ . \tag{5.4}$$

Every information about ρ in Hilbert space is equivalently stored in $W(q,p)$ in phase space. Quantum mechanics in phase space can be considered as an alternative but equivalent framework to the Hilbert space approach of Schrödinger and Heisenberg [140].

An explicit relation between the density matrix in the Fock (photon number) basis and the Wigner function, the so-called *Wigner transform* is given by

$$W(q,p) = \sum_{m,n}\langle m|\rho|n\rangle\cdot W_{mn}(q,p) \tag{5.5}$$

with basis functions [68, 140, 141]

$$W_{mn}(q,p) = \sqrt{\frac{m!}{n!}}e^{i(m-n)\arctan\frac{p}{q}}\frac{(-1)^m}{\pi}\sqrt{2(q^2+p^2)}^{n-m}L_m^{n-m}\big(2(q^2+p^2)\big)\ e^{-q^2-p^2}, \tag{5.6}$$

and L_m^n being the associated Laguerre polynomials. In practice, the Laguerre polynomials are efficiently evaluated with iterative schemes [68].

The Wigner function is normalized

$$\int_{-\infty}^{\infty}\int_{-\infty}^{\infty} W(q,p)\,\mathrm{d}q\,\mathrm{d}p = 1 \tag{5.7}$$

and bounded

$$|W(q,p)| \le \frac{1}{\pi}\ . \tag{5.8}$$

In contrast to a classical probability distribution, W can take on negative values, and in fact it is only strictly positive for Gaussian wave functions [142]. The appearance of negative values in W is an important criterion for non-classical states [143, 144].

The expectation value of a physical observable $\hat{A}$ for a state of density matrix ρ is obtained by the phase space overlap

$$\langle\hat{A}\rangle = \mathrm{tr}(\rho\cdot\hat{A}) = 2\pi\int_{-\infty}^{\infty}\int_{-\infty}^{\infty} W_\rho(q,p)\cdot W_{\hat{A}}(q,p)\,\mathrm{d}q\,\mathrm{d}p \tag{5.9}$$

where the Wigner functions $W_\rho(q,p)$ and $W_{\hat{A}}(q,p)$ are the phase space representations of ρ and $\hat{A}$, respectively.

A few examples of prominent Wigner functions and their marginal distributions are given in Fig. 5.1.

5.2. Schrödinger-Cat States in Quantum Optics

One of the most fundamental harmonic oscillator states is the coherent state $|\alpha\rangle$, the eigenstate of the annihilation operator ($\hat{a}|\alpha\rangle = \alpha|\alpha\rangle$), characterized by its complex-valued amplitude α [69]. Coherent states are considered the most classical states, and sometimes called "pseudo-classical states" [145], because they possess a well-defined amplitude and phase (within the Heisenberg limit) and are directly produced from a coherent light source like

a laser, or, for instance, a microwave oscillator. In terms of Fock states $|n\rangle$ with a given photon number n, coherent states consist of a Poisson-distribution with a coherent-phase relation between all components [69]:

$$|\alpha\rangle = e^{-\frac{|\alpha|^2}{2}} \sum_{n=0}^{\infty} \frac{\alpha^n}{\sqrt{n!}} |n\rangle \tag{5.10}$$

The coherent state has the Schrödinger wave function

$$\psi_\alpha(q) = \langle q|\alpha\rangle = \frac{1}{\pi^{1/4}} \exp\left(-\frac{1}{2}(q - \sqrt{2}\,\mathrm{Re}(\alpha))^2 + iq\sqrt{2}\,\mathrm{Im}(\alpha)\right) , \tag{5.11}$$

a Gaussian wave packet. In phase space, coherent states are two-dimensional Gaussian distributions of standard width $\sigma = \sqrt{1/2}$, centered in phase space at $(q,p) = (\sqrt{2}\,\mathrm{Re}\,\alpha, \sqrt{2}\,\mathrm{Im}\,\alpha)$:

$$W_\alpha(q,p) = \frac{1}{\pi} \exp\left(-(q - \sqrt{2}\,\mathrm{Re}\,\alpha)^2 - (p - \sqrt{2}\,\mathrm{Im}\,\alpha)^2\right) \tag{5.12}$$

An example of a coherent state with $\alpha = \sqrt{2}$ is shown in Fig. 5.1(b).

Quantum mechanics allows for superpositions of any two states of a system, in particular coherent states of opposite phase $|\alpha\rangle$ and $|-\alpha\rangle$ with an arbitrarily large amplitude. Those two states can be largely separated in phase space and are therefore macroscopically distinct. They are two oscillations of opposite phase. This is much like in Erwin Schrödinger's famous gedankenexperiment from 1935 [146], where he points out that even macroscopic objects like a cat could be in a superposition of two distinct states *alive* and *dead* if quantum mechanics is taken seriously. The coherent-state superposition

$$\frac{1}{N}(|\alpha\rangle + e^{i\theta}|-\alpha\rangle) \tag{5.13}$$

was consequently named a *cat state* [145, 147]. Here, θ is the superposition phase and $N = \sqrt{2(1 + \exp(-2|\alpha|^2)\cos\theta)}$ is a normalization factor. Cat states with $\theta = 0$ are called "even" cat states, and those with $\theta = \pi$ are called "odd" cat states, due to their Fock-space representations of only even or odd photon numbers (Sec. 5.6.1). The two coherent components are near-orthogonal for large α, as their overlap becomes small [69]:

$$\langle\alpha|\beta\rangle = e^{-(|\alpha|^2+|\beta|^2)/2+\alpha^*\beta}, \qquad |\langle\alpha|\beta\rangle|^2 = e^{-|\alpha-\beta|^2} \qquad \forall\alpha,\beta\in\mathbb{C} \tag{5.14}$$

$$\langle\alpha|-\alpha\rangle = e^{-2|\alpha|^2}, \qquad |\langle\alpha|-\alpha\rangle|^2 = e^{-4|\alpha|^2} \qquad \forall\alpha\in\mathbb{C} \tag{5.15}$$

From now on, we will assume $\alpha \in \mathbb{R}$, which is related to the more general case by a phase-space rotation. The Wigner function of cat states [145, 148] is:

$$W(q,p) = \frac{e^{-p^2}\left(e^{-(q+\sqrt{2}\alpha)^2} + e^{-(q-\sqrt{2}\alpha)^2} + 2\,e^{-q^2}\cos(\theta + \sqrt{8}\alpha p)\right)}{2\pi(1 + e^{-2\alpha^2}\cos\theta)} \tag{5.16}$$

It consists of two coherent peaks (Eq. (5.12)) and an additional interference pattern with a Gaussian envelope in the phase-space origin. Examples of cat-state Wigner functions are shown in Fig. 5.1(e),(f).

5.2.1. Experimental Creation of Cat States

With increasing control in quantum optics experiments in the last few decades, cat states have become a model system to study macroscopicity of quantum systems. And since the

underlying harmonic oscillator is ubiquitous in quantum physics, there is a wide range of platforms for their implementation. The first realization of cat states succeeded in 1996 on the motional state of a single ion, which then oscillates in two different directions at the same time [149–151]. Soon afterwards followed the realization on a stationary microwave field inside a cavity with the help of traversing Rydberg atoms [27, 152, 153]. More recently, cat states were also created on microwave fields in circuit QED [154–157]. Other types of systems include the mechanical motion of mesoscopic mechanical oscillators of various types [158] or approximate cat states in multi-spin systems [159].

5.2.2. Experimental Creation of Optical Cat States

The realization of cat states with optical light is especially appealing, because it allows for the fast and long-range transmission of states, and therefore a connection of remote quantum systems and the construction of quantum networks [47]. There has been quite a number of ideas how to create optical cat states in the laboratory [160, 161]. Experimental realizations, however, have essentially all been based on the idea of conditional measurements of squeezed states on a beam splitter, which probabilistically produces approximate cat states as long as α is small [162]. After the first demonstration in 2006 [163], a many improved versions followed [164–169]. While optical cats have so-far only been created in a heralded fashion, there is great effort under way to release them in a quasi-deterministic manner [170].

5.2.3. Entangled Cat States

There is a second class of cat states, which are not only in a superposition, but entangled to another system. If taken literally, Schrödinger's original gedankenexperiment [146] was of that type. His cat remains entangled to an atom in two possible states (decayed and not decayed), representing one qubit. To discriminate the different kinds of cat states, we will henceforth denote the entangled state as "Schrödinger-cat state" and the disentangled superposition state as "cat state". A variety of entangled optical Schrödinger-cat states has been created with heralded protocols of conditioned measurements [171–176] and microwave Schrödinger-cat states were created in circuit QED [156, 177]. When the atom part of the Schrödinger-cat state is well controlled, a suitable projective measurement in a superposition basis can turn the optical part into a superposition cat state, disentangled from the atom. In Schrödinger's original gedankenexperiment this was not the case, but in many of today's implementations it is.

5.2.4. Applications of Cat States

Cat states are not only a model system for potentially macroscopic states and their behavior under decoherence. They also feature some neat properties for quantum information processing. A qubit encoded in an arbitrary superposition of $|\alpha\rangle$ and $|-\alpha\rangle$ with small overlap $|\langle-\alpha|\alpha\rangle|^2$ may be processed with universal quantum gate operations using the tools of linear optics quantum computing [178–180]. Such operations can be made fault tolerant using several states in parallel [181, 182] or using multi-component cat-states [183, 184], as pioneered in circuit QED [185, 186]. Therefore, optical cat states offer the perspective for quantum communication with correction for transmission losses [187], for instance in a quantum repeater based on optical cavities [188].

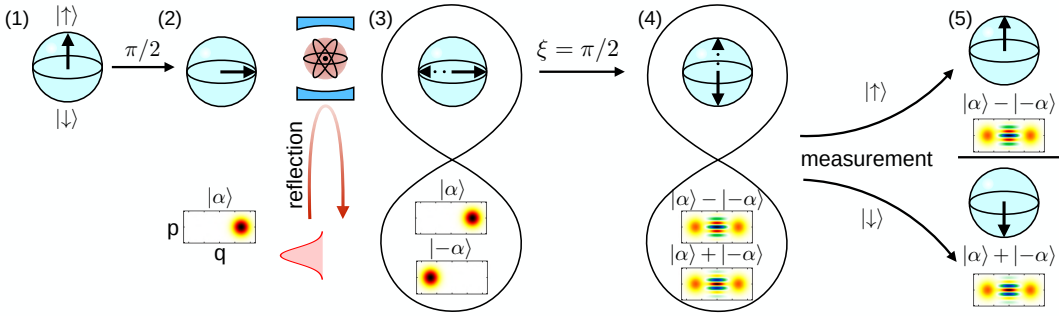

Figure 5.2.: Protocol for the creation of optical cat states. Initially the atom is prepared in the state $|\uparrow\rangle$ (1) before a $\pi/2$ rotation is applied to bring it into the coherent superposition $(|\uparrow\rangle+|\downarrow\rangle)/\sqrt{2}$ (2). Then, a coherent state $|\alpha\rangle$ is reflected from the cavity and thus an entangled state $(|\uparrow\rangle|\alpha\rangle+|\downarrow\rangle|-\alpha\rangle)/\sqrt{2}$ is created (3). A subsequent $\pi/2$ rotation on the atom prepares $\frac{1}{2}\left[|\uparrow\rangle\left(|\alpha\rangle - |-\alpha\rangle\right) + |\downarrow\rangle\left(|\alpha\rangle + |-\alpha\rangle\right)\right]$ (4). The last step in the protocol is a state detection on the atom that projects the optical part onto the even or the odd cat state (5). (from [137])

5.3. Cat States from an Optical Cavity

In 2005, it was realized that optical cat states could be created by the interaction of a light pulse with one single atom in an optical cavity [189]. This scheme has important advantages over previous experiments: It produces theoretically exact cat states without coarse approximations and for arbitrary amplitudes α, and does this deterministically, i.e. in every attempt. The experimental requirement is one atom that is strongly coupled to an optical cavity, just as in the QGate setup.

The protocol, illustrated in Fig. 5.2, works as follows. Reflection of a light pulse from the cavity will shift the optical phase by an angle ϕ depending on the state of the atom. In the resonant case of a π-phase shift (Eq. (2.38)), the amplitude α gets flipped only in case of a non-coupling atom $|\downarrow\rangle$, but not when it couples $|\uparrow\rangle$:

$$|\uparrow\rangle|\alpha\rangle \rightarrow |\uparrow\rangle|\alpha\rangle, \qquad |\downarrow\rangle|\alpha\rangle \rightarrow |\downarrow\rangle|-\alpha\rangle \tag{5.17}$$

When the atom is in an equal superposition of coupling and non-coupling states, the reflection entangles the (potentially macroscopic) light field with the atom, much like in Schrödinger's gedankenexperiment:

$$\frac{1}{\sqrt{2}}(|\uparrow\rangle + |\downarrow\rangle)|\alpha\rangle \quad \rightarrow \quad \frac{1}{\sqrt{2}}(|\uparrow\rangle|\alpha\rangle + |\downarrow\rangle|-\alpha\rangle) \tag{5.18}$$

Henceforth the state of the atom and the light pulse are entangled, and a measurement of the atom in the $|\uparrow\rangle/|\downarrow\rangle$ basis would determine the phase of the light pulse immediately. But unlike in classical physics, the correlation between the two subsystems is not limited to one given basis. Eq. (5.18) can be rewritten as

$$\frac{1}{\sqrt{8}}\Big((|\uparrow\rangle + |\downarrow\rangle)(|\alpha\rangle + |-\alpha\rangle) + (|\uparrow\rangle - |\downarrow\rangle)(|\alpha\rangle - |-\alpha\rangle)\Big) \tag{5.19}$$

where the entanglement is apparently between superposition states of the atom and of the light field. The correlation persists, if one of the two subsystems is coherently manipulated between various superposition states. The atomic qubit can be rotated with the Raman laser the same way it was rotated to prepare the initial superposition state. A rotation angle of $\xi = \pi/2$ around a rotation axis shifted by θ (with respect to the initial superposition-state preparation) creates the combined state

$$\frac{1}{2}\Big(\big(|\uparrow\rangle + e^{-i\theta}|\downarrow\rangle\big)|\alpha\rangle + \big(-e^{i\theta}|\uparrow\rangle + |\downarrow\rangle\big)|-\alpha\rangle\Big) = \tag{5.20}$$

$$= \frac{1}{2}\Big(|\uparrow\rangle\big(|\alpha\rangle - e^{i\theta}|-\alpha\rangle\big) + e^{-i\theta}|\downarrow\rangle\big(|\alpha\rangle + e^{i\theta}|-\alpha\rangle\big)\Big) \,. \tag{5.21}$$

Here, the $|\uparrow\rangle/|\downarrow\rangle$ eigenstates of the atom correspond to cat states of the light field. A projective measurement of the atom yields:

$$|\uparrow\rangle : \qquad \frac{|\alpha\rangle - e^{i\theta}|-\alpha\rangle}{\sqrt{2(1 - e^{-2\alpha^2}\cos\theta)}} \tag{5.22}$$

$$|\downarrow\rangle : \qquad \frac{|\alpha\rangle + e^{i\theta}|-\alpha\rangle}{\sqrt{2(1 + e^{-2\alpha^2}\cos\theta)}} \tag{5.23}$$

The measurement outcome of the atomic spin is necessarily random, due to the entanglement. The resulting photonic state is a cat state (Eq. (5.13)) in both cases, but the superposition phase factor $\pm e^{i\theta}$ depends on the measurement outcome. For the case of a constant spin rotation axis ($\theta = 0$), an outcome of $|\uparrow\rangle$ signals the creation of an odd cat state and $|\downarrow\rangle$ signals the creation of an even cat state.

The probability to obtain each of the two cat states is 50% for $\alpha \gg 1$, but in general, the Born rule applied to Eq. (5.21) yields

$$P(|\uparrow\rangle) = \frac{1}{2}\left(1 - e^{-2\alpha^2}\cos\theta\right) \qquad P(|\downarrow\rangle) = \frac{1}{2}\left(1 + e^{-2\alpha^2}\cos\theta\right) \,, \tag{5.24}$$

which means the probability for an atomic spin flip during the light reflection reduces when the reflected light field is close to the vacuum. In case of a real cavity with optical losses, the effective α in $P(|\uparrow\rangle/|\downarrow\rangle)$ is reduced with respect to the incident amplitude α_0 as $\alpha = \sqrt{\eta}\,\alpha_0$, which will be discussed in Sec. 5.7.

5.4. Optical Loss

Optical loss is one of the key challenges in working with non-classical states, because it reduces quantum features and – in contrast to classical optics – it cannot be reverted straightforwardly. Losses occur in many optical components in the laboratory at a percent-level.

The effect of losses on a generic quantum state ρ is obtained theoretically by a beamsplitter model [68, 190, 191]. One can assume that the optical state of interest passes an ideal beam splitter, with intensity reflection equal to a loss fraction L, and transmission $1 - L$, where the second input port is open and contains the vacuum mode $|0\rangle_l$. After transmission, the optical state is split between the two output modes. Subsequently, the loss mode gets absorbed and the transmitted state is obtained by tracing out the loss mode. The output after losses is then given by the reduced density matrix.

$$\rho_{\text{out}} = \text{tr}_l\left(\hat{S}(\rho_{\text{in}} \otimes |0\rangle_l\langle 0|_l)\hat{S}^\dagger\right) \tag{5.25}$$

Here

$$\hat{S} = \exp\big(\arccos(\sqrt{1-L})(\hat{a}_{\text{in}} \otimes \hat{a}_l^\dagger - \hat{a}_{\text{in}}^\dagger \otimes \hat{a}_l)\big) \tag{5.26}$$

is the unitary transformation matrix of the beam splitter [161]. The resulting state ρ_{out} is given by the linear map [192]

$$\rho_{\text{out}} = \sum_i \hat{M}_i \rho \hat{M}_i^\dagger \qquad \text{with} \qquad \hat{M}_i = L^{i/2}(1-L)^{(\hat{a}^\dagger\hat{a})/2}\hat{a}^i/\sqrt{i!} \,. \tag{5.27}$$

The matrix elements in the Fock basis of photon-number states $|m\rangle$ and $|n\rangle$ are [68]

$$\langle m|\rho_{\text{out}}|n\rangle = \sum_{k=0}^{\infty} \sqrt{b_n^{n+k}(L) \cdot b_m^{m+k}(L)} \langle m+k|\rho|n+k\rangle \ , \tag{5.28}$$

which is called a generalized Bernoulli transformation, where $b_k^n(L)$ is the binomial distribution

$$b_k^n(L) = \binom{n}{k} L^{n-k}(1-L)^k \ . \tag{5.29}$$

This means that each discrete photon-number component of the original state will be turned into a broader binomial distribution of Fock components in the final state. Losses tend to smooth the photon-number distribution. Eq. (5.28) is applied in Sec. 5.9.3 to compensate for losses in measured states.

In phase space, loss has two effects on the Wigner function: First, all amplitudes are reduced to a fraction $\sqrt{1-L}$, and the whole Wigner function is contracted towards the phase-space origin by the same amount. Second, the Wigner function gets convoluted by a Gaussian of width $\sqrt{L/2}$, that broadens the distribution [68, 193]. With these actions combined, any coherent state will keep its width of $\sigma = \sqrt{1/2}$. The convolution smears out sharp features and negative regions, such that they eventually disappear for large enough losses. The sharper the features, the more they will be affected by the convolution.

5.4.1. Losses on Cat States

In this section, we examine a generic cat state under the influence of relative intensity losses L, which occur when the optical beam passes an absorber. The surviving intensity fraction will be $R = 1 - L$, with a relative amplitude of $r = \sqrt{R}$. Let us consider an initial ideal cat state

$$|\psi_{\text{cat}}\rangle = \frac{|\alpha\rangle + e^{i\theta}|-\alpha\rangle}{\sqrt{2(1+e^{-2\alpha^2}\cos\theta)}} \tag{5.30}$$

with real and symmetric amplitudes α and $-\alpha$. This case already covers the features of cat states with two arbitrary amplitudes, because these can be considered rotated and shifted versions of a centered cat state in phase space. The essential parameters are the peak distance $2\sqrt{2}\alpha$ and the superposition phase θ. The initial state has a pure density matrix

$$\rho_{\text{cat}} = |\psi_{\text{cat}}\rangle\langle\psi_{\text{cat}}| = \frac{|\alpha\rangle\langle\alpha| + e^{-i\theta}|\alpha\rangle\langle-\alpha| + e^{i\theta}|-\alpha\rangle\langle\alpha| + |-\alpha\rangle\langle-\alpha|}{2(1+e^{-2\alpha^2}\cos\theta)} \ . \tag{5.31}$$

The effect of losses on such a state is discussed to some extent in [194], and more explicitly in [161, 187, 192, 195, 196] with varying parametrizations and levels of detail. When the cat state is affected by losses L, the state becomes [192]

$$\rho_{\text{cat,loss}} = \frac{|r\alpha\rangle\langle r\alpha| + e^{-2L\alpha^2}\left(e^{-i\theta}|r\alpha\rangle\langle-r\alpha| + e^{i\theta}|-r\alpha\rangle\langle r\alpha|\right) + |-r\alpha\rangle\langle-r\alpha|}{2(1+e^{-2\alpha^2}\cos\theta)} \tag{5.32}$$

where the amplitudes have reduced to $\pm r\alpha$ and the coherences are damped by $e^{-2L\alpha^2}$. The normalization, however, has not changed. In the Fock basis, the state is (here with complex α)

$$\langle n|\rho_{\text{cat,loss}}|m\rangle = \frac{(r\alpha)^n (r\alpha^*)^m}{\sqrt{n!\,m!}} e^{-|r\alpha|^2} \frac{1 + (-1)^{n+m} + e^{-2L|\alpha|^2}(e^{i\theta}(-1)^n + e^{-i\theta}(-1)^m)}{2(1+e^{-2|\alpha|^2}\cos\theta)} \ . \tag{5.33}$$

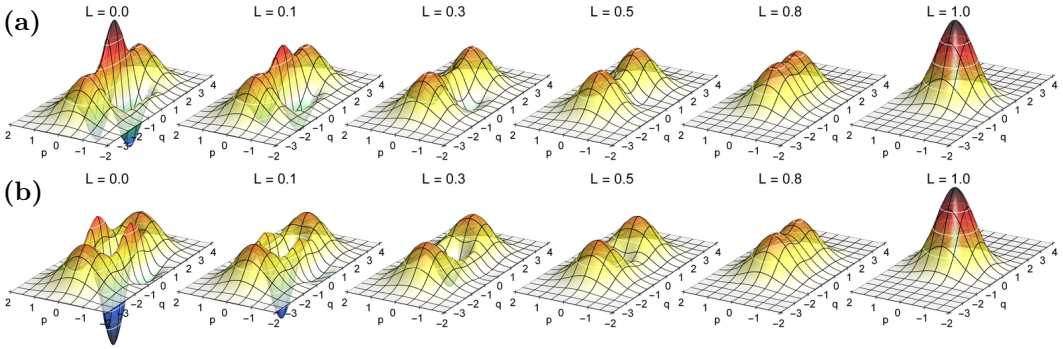

Figure 5.3.: Effect of losses on even and odd cat states. (a) Even cat state, $\alpha = \sqrt{2}$, $\theta = 0$, (b) odd cat state $\alpha = \sqrt{2}$, $\theta = \pi$. The sharp interference fringes for $L = 0$ drop quickly with increasing losses. Above $L = 0.5$, all negative values vanish. For $L = 1$, both coherent peaks merge to the vacuum.

The corresponding Wigner function (assuming a real α again) is [192]

$$W(q,p) = \frac{e^{-p^2}\left(e^{-(q+\sqrt{2}r\alpha)^2} + e^{-(q-\sqrt{2}r\alpha)^2} + 2\,e^{-2L\alpha^2}\,e^{-q^2}\cos(\theta+\sqrt{8}r\alpha p)\right)}{2\pi(1+e^{-2\alpha^2}\cos\theta)}\,. \tag{5.34}$$

Figure 5.3 shows this Wigner function with $\alpha = \sqrt{2}$ for various losses L. As in the density matrix (Eq. (5.32)), coherence terms are damped by $e^{-2L\alpha^2}$. The frequency of the fringes $\sqrt{8}r\alpha$ reduces proportionally to the coherent peak amplitude α.

5.5. The Effect of Imperfect Atomic State Detection

While optical losses are most relevant for large α, there is a second important imperfection in experimental implementations of the presented protocol, most relevant for small α. The presented protocol requires a measurement of the atomic spin and produces two complementary optical cat states with opposite phase θ depending on the measurement outcome. Every atomic state detection has a small finite error ϵ to yield the wrong result, which will be assumed here to be identical for the two cases $|\uparrow\rangle$ and $|\downarrow\rangle$ for simplicity. In the experiment, ϵ contains actual wrong state detections from photon dark counts or a lack of sufficient counts, as well as imperfect state preparation and imprecise state rotations. The value of ϵ fluctuates over time in the experiment, but typically $\epsilon = 2\%$. For convenience, I introduce the parameter $s := 1-2\epsilon$, which is 1 for an ideal state detection and -1 for a state detection that always yields the opposite result.

Measured optical states are conditioned on the measured atomic state-detection outcome. The amount of admixture of complementary cat states can be quantified with Bayesian statistics. Using Eq. (5.24), the marginal probability of actually creating a cat state with superposition phase θ is $P(\mathrm{cat}_\theta) = (1 + e^{-2\alpha^2}\cos\theta)/2$. The conditional probability to actually measure the atom in $|\downarrow\rangle$ when the cat state $|\mathrm{cat}_\theta\rangle$ was created, is $P(\downarrow|\mathrm{cat}_\theta) = 1-\epsilon$, and analogously $P(\downarrow|\mathrm{cat}_{\theta+\pi}) = \epsilon$. The marginal probability to find the atom in $|\downarrow\rangle$ is

$$\begin{aligned} P(\downarrow) &= P(\downarrow|\mathrm{cat}_\theta)P(\mathrm{cat}_\theta) + P(\downarrow|\mathrm{cat}_{\theta+\pi})P(\mathrm{cat}_{\theta+\pi}) = \\ &= \frac{1+(1-2\epsilon)e^{-2\alpha^2}\cos\theta}{2} = \frac{1}{2} + \frac{s}{2}e^{-2\alpha^2}\cos\theta\,. \end{aligned} \tag{5.35}$$

Hence, using Bayes' theorem, the conditional probability to have the anticipated optical state, given the atomic state outcome $|\downarrow\rangle$, is

$$P(\mathrm{cat}_\theta|\downarrow) = \frac{P(\downarrow|\mathrm{cat}_\theta)\cdot P(\mathrm{cat}_\theta)}{P(\downarrow)} = \frac{(1-\epsilon)(1+e^{-2\alpha^2}\cos\theta)}{1+(1-2\epsilon)e^{-2\alpha^2}\cos\theta}\ . \tag{5.36}$$

In the complementing cases with $P(\mathrm{cat}_{\theta+\pi}|\downarrow) = 1 - P(\mathrm{cat}_\theta|\downarrow)$, the opposite cat state is created and will be admixed incoherently in the result.

In particular for the case of $\theta = 0$, the likelihood for odd and even cat states given the respective outcome of the atomic state detection is

$$P(\mathrm{cat}_{\mathrm{odd}}|\uparrow) = \frac{1-\epsilon}{1-\epsilon+\epsilon\coth(\alpha^2)}\ , \tag{5.37}$$

$$P(\mathrm{cat}_{\mathrm{even}}|\downarrow) = \frac{1-\epsilon}{1-\epsilon+\epsilon\tanh(\alpha^2)}\ . \tag{5.38}$$

This means, for large α, the admixture of opposite cat states tends towards $1-\epsilon$, so the erroneous contributions are small. However, for small α the likelihood for an even cat increases for both atomic state-detection outcomes. In particular, with any non-zero ϵ, $P(\mathrm{cat}_{\mathrm{odd}}|\uparrow)_{\alpha\to 0} \to 0$, such that very small odd cat states have a dominating unanticipated contribution of small even cats, and the created odd cat states $|\mathrm{cat}_{\mathrm{odd}}\rangle$ will ultimately not approach the single-photon Fock state, but the vacuum state instead.

5.6. Properties of Lossy Cat States

With the analytic expressions for the cat states (Eq. (5.32)) at hand, let us derive several properties, which we can later compare to the experimental data. Some properties can be found in the literature and they are marked with citations. The other expressions were derived in the course of this work. Unless otherwise noted, the states contain losses L as well as a state detection parameter s.

5.6.1. Photon Number and Statistics

The photon-number distribution of a cat state after losses follows directly from Eq. (5.33)

$$P(n) = \langle n|\rho_{\mathrm{cat,loss}}|n\rangle = \frac{((1-L)\alpha^2)^n}{n!}e^{-(1-L)\alpha^2}\cdot\frac{1+(-1)^n s\, e^{-2L\alpha^2}\cos\theta}{1+s\, e^{-2\alpha^2}\cos\theta}\ . \tag{5.39}$$

The first part of this formula is the Poissonian distribution of a coherent state $|r\alpha\rangle$. The second part creates an oscillatory behavior in n through the $(-1)^n$ term (see also [145, 194]), which depends on the even- or oddness through θ. This oscillation is damped by losses proportionally to $e^{-2L\alpha^2}$, which was for instance shown in [192].

The mean photon number $\overline{n}$ of a cat state after losses is:

$$\overline{n} = \mathrm{tr}(\hat{n}\cdot\rho_{\mathrm{cat,loss}}) = (1-L)\alpha^2\cdot\frac{1-s\, e^{-2\alpha^2}\cos\theta}{1+s\, e^{-2\alpha^2}\cos\theta} \tag{5.40}$$

Consequently $\overline{n} \simeq \alpha^2$ for the ideal cat states at large α. The fraction is a correction factor at small α, and losses reduce the mean photon number linearly.

Non-classical light is often characterized through photon statistics, which can be measured with simple single-photon detectors. Any photon statistic can be derived from the distribution function $P(n)$ (Eq. (5.39)).

The photon-number parity Π can be defined as the probabilty to have an even photon number minus the probability for an odd photon number. Thus, an ideal even cat state has the maximum parity 1 and an odd one the minimum parity -1, regardless of α. With losses, we obtain:

$$\Pi = \sum_n (-1)^n P(n) = \frac{e^{-2(1-L)\alpha^2} + s\, e^{-2L\alpha^2} \cos\theta}{1 + s\, e^{-2\alpha^2} \cos\theta} \tag{5.41}$$

The Mandel Q parameter [197], designed to measure deviations from Poissonian statistics, is

$$Q = \frac{\langle (\Delta\hat{n})^2 \rangle - \langle \hat{n} \rangle}{\langle \hat{n} \rangle} = 4(1-L)\alpha^2 \frac{(s + e^{-2\alpha^2}\cos\theta) e^{-2\alpha^2}\cos\theta}{(1 + s\, e^{-2\alpha^2}\cos\theta)(1 - (e^{-2\alpha^2}\cos\theta)^2)} \,, \tag{5.42}$$

and, if $s = 1$,

$$Q = 4(1-L)\alpha^2 \frac{e^{-2\alpha^2}\cos\theta}{(1 - (e^{-2\alpha^2}\cos\theta)^2)} \,. \tag{5.43}$$

It only deviates much from 0 at small α, even for low losses. On the other hand, it is rather robust to losses, because L enters only linearly.

5.6.2. Marginal Distribution

The marginal distribution $\mathrm{pr}_\varphi(q_\varphi)$ of the lossy cat state (Eq. (5.34)) is obtained via projection (Eq. (5.3)) along the direction p_φ. Hence the marginal distribution of a cat state after losses, assuming good state detection ($s = 1$), is:

$$\mathrm{pr}_\varphi(q_\varphi) = \frac{1/(2\sqrt{\pi})}{1 + e^{-2\alpha^2}\cos\theta} \Big(e^{-(q_\varphi + \sqrt{2} r\alpha \cos(\varphi))^2} + e^{-(q_\varphi - \sqrt{2} r\alpha \cos(\varphi))^2} + 2 e^{-2L\alpha^2} e^{-q_\varphi^2 - 2(r\alpha)^2 \cos^2(\varphi)} \cos(\theta + \sqrt{8} r\alpha \sin(\varphi) q_\varphi) \Big) \,. \tag{5.44}$$

Each of the three Gaussian peaks in the Wigner function leads to a Gaussian component in the marginal distribution. The two coherent components are sinusoidally modulated in φ and the fringe component is again damped by $e^{-2L\alpha^2}$. Examples of cat-state marginal distributions with and without loss are shown in Fig. 5.4.

5.6.3. Wigner Function at the Phase-Space Origin

The value of the Wigner function at the phase-space origin $W(0,0)$ is proportional to the parity Π (Eq. (5.41)), because $W_{|n\rangle}(0,0) = (-1)^n/\pi$,

$$W(0,0) = \frac{e^{-2(1-L)\alpha^2} + s\, e^{-2L\alpha^2} \cos\theta}{\pi(1 + s\, e^{-2\alpha^2} \cos\theta)} \tag{5.45}$$

and a plot of this is shown in Fig. 5.5. The central fringe amplitude drops almost exponentially like $e^{-2L\alpha^2}$ and approaches the vacuum value $+1/\pi$ at $L = 1$ with the same rate as the interference dropped for small L. For odd cats, $W(0,0)$ crosses 0 exactly at $L = 0.5$. The fringe amplitude at the origin is a well measurable quantity that is for instance hardly affected by phase noise and therefore proves useful to quantify losses in the experiment.

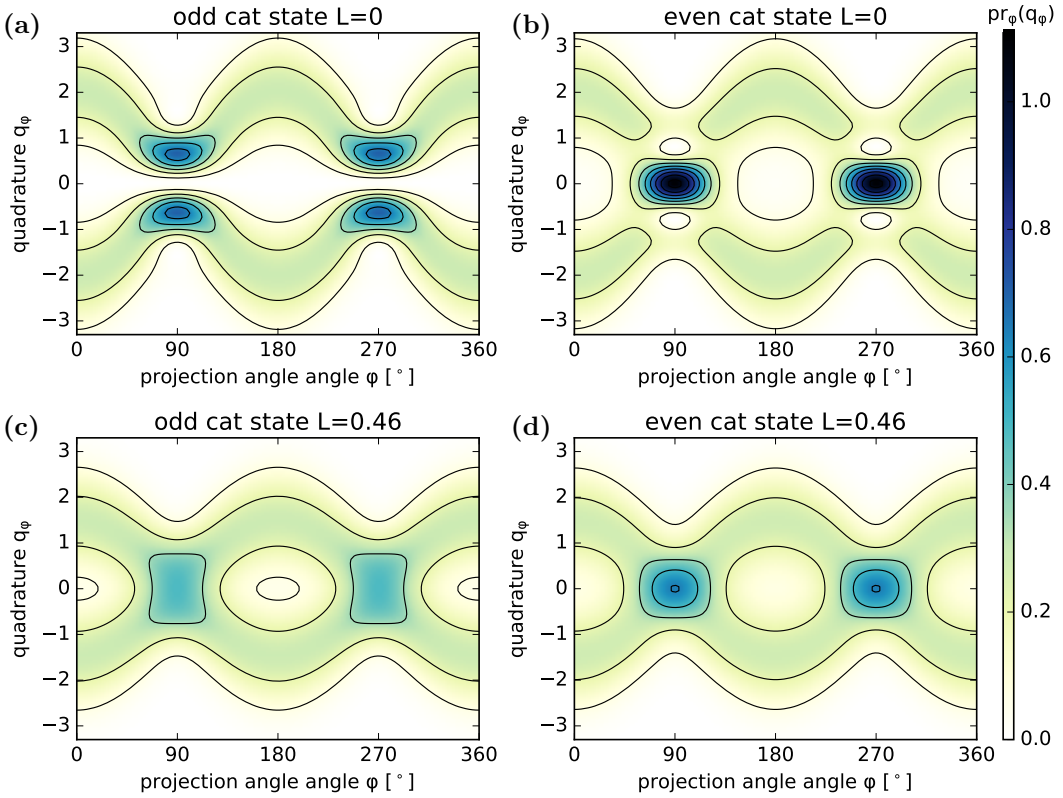

Figure 5.4.: Theoretical marginal distribution of cat states. The marginal distributions $\mathrm{pr}_{\varphi}(q_{\varphi})$ for an odd (a) and an even (b) cat state of $\alpha = 1.41$ and $L = 0$ are plotted vs. φ and q_{φ} according to Eq. (5.44), assuming $s = 1$. Increased losses $L = 0.46$ in (c) and (d) reduce the oscillation amplitude and damp the interference features around $q_{\varphi} = 0, \varphi = 90°$ and $\varphi = 270°$ where the two states differ the most.

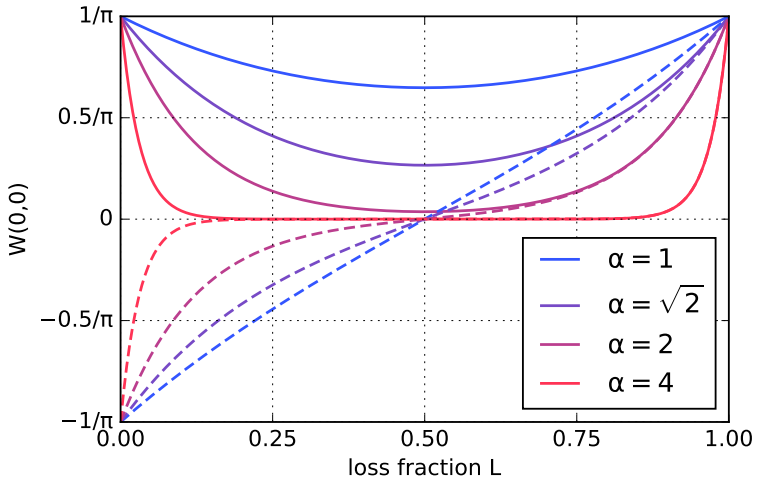

Figure 5.5.: Central value $W(0,0)$ of cat-state Wigner functions with loss. Even cat states (solid lines) have a maximum in the center that drops with increasing losses L for $L < 50\%$ depending on α^2. Odd cat states (dashed lines) have a negative minimum in the center. At losses of 50% and above, the Wigner function becomes strictly positive and $W(0,0)$ increases towards the vacuum value at $L = 1$. Here, the atomic state detection is considered ideal ($s = 1$).

5.6.4. Visibility

As the cavity experiment creates pairs of cat states with opposite θ, we can define another useful quantity, the fringe visibility

$$V = \frac{\pi}{2}(W_{\mathrm{even}}(0,0) - W_{\mathrm{odd}}(0,0)) = \frac{s\, e^{-2L\alpha^2}(1 - e^{-4(1-L)\alpha^2})}{1 - s^2 e^{-4\alpha^2}}\,, \tag{5.46}$$

which is 1 for ideal cat states and drops with increasing losses. When the overlap of the two coherent peaks is small, $(1-L)\alpha^2 \gg 1$, and the state detection is good ($s = 1$), this approaches again the exponential $V \simeq e^{-2L\alpha^2}$.

5.6.5. Purity

The purity $\gamma = \mathrm{tr}(\rho^2)$ quantifies how much a state is mixed. The purity of an ideal cat state is 1, and drops with increasing losses.

$$\gamma = \mathrm{tr}(\rho_{\mathrm{cat,loss}}^2) = 1 - \frac{(1 - e^{-4(1-L)\alpha^2}) \cdot (1 - s^2\, e^{-4L\alpha^2})}{2(1 + s\, e^{-2\alpha^2} \cos\theta)^2} \tag{5.47}$$

At large α and intermediate losses, γ will approach 1/2, because then the state becomes a mixture of two coherent states without interference.

5.6.6. Fidelity

The fidelity F of a cat state after losses (Eq. (5.32)) with an equally large ideal cat of amplitude $r\alpha$ is:

$$\begin{aligned} F &= \langle \psi_{\mathrm{cat}} | \rho_{\mathrm{cat,loss}} | \psi_{\mathrm{cat}} \rangle \\ &= \frac{\langle r\alpha| + e^{-i\theta}\langle -r\alpha|}{\sqrt{2(1 + e^{-2(1-L)\alpha^2}\cos\theta)}} \rho_{\mathrm{cat,loss}} \frac{|r\alpha\rangle + e^{i\theta}|-r\alpha\rangle}{\sqrt{2(1 + e^{-(1-L)\alpha^2}\cos\theta)}} \\ &= 1 - \frac{1}{2} \cdot \frac{(1 - e^{-4(1-L)\alpha^2})(1 - s\, e^{-2L\alpha^2})}{(1 + e^{-2(1-L)\alpha^2}\cos\theta)(1 + s\, e^{-2\alpha^2}\cos\theta)} \end{aligned} \tag{5.48}$$

The two coherent peaks contribute approximately 1/2 to the fidelity, and the fringes contribute another 1/2, so for intermediate losses $1/\alpha^2 \ll L \ll 1 - 1/\alpha^2$ the fidelity will drop to 1/2.

For the fidelity with cats of the original amplitude α instead of the reduced amplitude $r\alpha$, see [161].

5.6.7. Squeezing

Quite remarkably, cat states, which are superimposed from two coherent states, may have a narrower phase-space distribution than a single coherent state, a property called squeezing. This property was already discovered in the pioneering paper on cat states [145]. The squeezing of cat states under the influence of losses was derived in [194], although not for arbitrary θ.

Cat states in our parametrization are most narrow in p-direction (see Fig. 5.1(e)). One finds:

$$\langle p^2 \rangle = \frac{1}{2} - 2(1-L)\alpha^2 \frac{s\, e^{-2\alpha^2}\cos\theta}{1 + s\, e^{-2\alpha^2}\cos\theta} \tag{5.49}$$

and

$$(\Delta p)^2 = \langle p^2 \rangle - \langle p \rangle^2 = \frac{1}{2} - 2(1-L)\alpha^2 \frac{s\, e^{-2\alpha^2}(s\, e^{-2\alpha^2} + \cos\theta)}{(1 + s\, e^{-2\alpha^2}\, \cos\theta)^2} \,. \tag{5.50}$$

A comparison with the width of a coherent peak, $(\Delta p_0)^2 = \sigma^2 = 1/2$ shows that cat states are always squeezed for $|\theta| < \pi/2$, $L < 1$ and $s > 0$. The p-variance of an even cat with ideal state detection is

$$(\Delta p_{\mathrm{even}})^2 = \frac{1}{2} - 2(1-L)\alpha^2 \frac{1}{e^{2\alpha^2} + 1} \,, \tag{5.51}$$

which takes a minimum at $\alpha = 0.80$, with minimally achievable width of $\Delta p / \Delta p_0 = 0.665$ and a maximum squeezing parameter of $10 \log_{10}((\Delta p_0)^2/(\Delta p)^2)$ of 3.54 dB.

5.6.8. Cattiness

The idea of cat states is to study macroscopic quantum objects. This requires two things: First, the state needs to be "macroscopic", which is easily realized in this experiment by choosing a large α. Second, the state needs a sufficient amount of quantum coherence, which, in the case of optical cat states, corresponds to a good fringe visibility. Several measures for macroscopic quantumness have been developed [198], and they are often called "cattiness". We will examine one such measure $\mathcal{I}(\rho)$ here, which is described in [199],

$$\mathcal{I}(\rho) = -\operatorname{tr}\big(\rho \mathcal{L}(\rho)\big) \tag{5.52}$$

with the Lindblad superoperator

$$\mathcal{L}(\rho) = \hat{a}\rho\hat{a}^\dagger - \frac{1}{2}\rho\hat{a}^\dagger\hat{a} - \frac{1}{2}\hat{a}^\dagger\hat{a}\rho \,. \tag{5.53}$$

This cattiness $\mathcal{I}(\rho)$ essentially measures how quickly the purity of ρ degrades through losses, which is a characteristic of macroscopic quantum states.

For lossy cat states (at ideal state detection $s = 1$), we obtain

$$\mathcal{I}(\rho_{\mathrm{cat,loss}}) = (1-L)\alpha^2 \cdot \frac{e^{-4L\alpha^2} - e^{-4(1-L)\alpha^2}}{(1 + e^{-2\alpha^2}\cos\theta)^2} \,. \tag{5.54}$$

It has indeed the property that it approximates the photon number of a cat state $n \simeq \alpha^2$ when the amplitude is large and losses are negligible. The exponential damping term $e^{-4L\alpha^2}$ brings the cattiness close to zero whenever L is not tiny. The cattiness is extremely sensitive to losses. For instance, small losses $L = 0.01$ will limit the maximally achievable cattiness to 9.1, and a moderate value of $L = 0.19$ will already limit the cattiness to 0.50.

5.6.9. Entanglement Potential

The entanglement potential (EP) [200] is a measure of non-classicality that can be applied to any density matrix. The idea is that if the state of interest was sent through an (imaginary) 50/50 beam splitter and the two output modes showed entanglement, then the state must have been non-classical before the beam splitter. The EP is an appealing measure, because it witnesses the non-classicality of cat states [201] for arbitrarily large losses $L < 1$ [144], even where other measures, such as negative values of the Wigner function, would fail to do so.

The EP uses a generic entanglement measure such as the logarithmic negativity [130] and applies it to the two beam-splitter output modes:

$$\mathrm{EP}(\rho) = \log_2 ||\sigma^{T_a}||_1 \ , \tag{5.55}$$

where σ^{T_a} is the partial transpose of the two-mode output state σ after the beam splitter

$$\sigma = S(\rho \otimes |0\rangle\langle 0|)S^\dagger \tag{5.56}$$

with the beam splitter transformation operator S like in Eq. (5.26). An analytic evaluation of Eq. (5.55) may be intricate. However, the EP can be evaluated numerically in truncated Fock space for any state ρ, for instance using the software toolbox "QuTiP" [133].

5.7. Losses in the Cavity

When cat states are produced at our cavity by the protocol outlined in Sec. 5.3, there is an immediate optical loss during the reflection, due to the limited cooperativity $C = 4.1 < \infty$ and single-sidedness $\kappa_r/\kappa < 1$ of the cavity. At the beginning of the experiment, it was an open question whether those losses fully affect the cat states like the absorption losses in the previous section. In this section, we will see that this is not the case. It is shown that the cat size is reduced by the full amount of losses, but the interference fringes are only affected by half of the losses, in terms of optical depth. In a simplified picture, half of the losses strike before the cat state is created, and the other half strikes afterwards. The first half acts like an absorber in the ingoing coherent laser beam and does not deteriorate the resulting state.

To calculate the effect of cavity losses, we make two assumptions: First, the optical intensity varies slowly compared to the dynamic timescale of the system $1/\kappa$. Therefore, the field changes adiabatically, and can be described as a single-frequency mode with constant phase shift (Eq. (2.25)). Second, the probability of having the atom excited when a second photon enters the system is low, and therefore higher states in the Jaynes-Cummings ladder can be neglected. Under these conditions, the system is well described by input-output theory [63] and we can use the above-mentioned amplitudes (Eq. (2.14)–(2.17)).

We consider an incoming coherent beam of amplitude α_0. The relevant optical modes are $|\alpha_0\rangle$ for the input beam, $|r_{\uparrow/\downarrow}\rangle$ for the reflected (output) mode, $|t_{\uparrow/\downarrow}\rangle$ for the cavity transmission, $|m_{\uparrow/\downarrow}\rangle$ for the mirror losses and $|a_{\uparrow/\downarrow}\rangle$ for scattering via the atom, where the variables inside the vectors denote modes and amplitudes. The modes $|m_{\uparrow/\downarrow}\rangle$ and $|a_{\uparrow/\downarrow}\rangle$ may become phase-randomized in the incoherent scattering processes, with density matrices $\rho_\alpha = e^{-|\alpha|^2} \sum_n \frac{|\alpha|^{2n}}{n!} |n\rangle\langle n|$. While the overlap fidelity of two coherent states is $F(|\alpha\rangle, |\beta\rangle) = |\langle\alpha|\beta\rangle|^2 = \exp(-|\alpha - \beta|^2)$ (Eq. (5.14)), that of two phase-randomized coherent states is $F(\rho_\alpha, \rho_\beta) = \mathrm{tr}^2 \sqrt{\sqrt{\rho_\alpha}\rho_\beta\sqrt{\rho_\alpha}} = \exp(-\big||\alpha| - |\beta|\big|^2)$. These two overlap fidelities are identical when the amplitudes α and β have the same phase, which is the case both for $|a_\uparrow\rangle$ and $|a_\downarrow\rangle$ as well as for $|m_\uparrow\rangle$ and $|m_\downarrow\rangle$ in the resonant system. Therefore the loss modes can be treated like pure states, for simplicity, in the following derivation.

The output in the reflection mode will be a superposition of two coherent fields of amplitude $r_\downarrow$ and $r_\uparrow$. If the moduli of the two amplitudes differ, the resulting cat state in phase space will be off-centered, which may be corrected with a displacement operation. In our experiment however, the two amplitudes are approximately identical (Fig. 2.4). The total size of the cat state is given by the amplitude distance of the two coherent components in phase space

$$\alpha_{\mathrm{out}} = \frac{1}{2}|r_\uparrow - r_\downarrow| = \frac{\kappa_r}{\kappa}\frac{g^2}{g^2 + \kappa\gamma}\alpha_0 = \eta\alpha_0 \ , \tag{5.57}$$

where we use the definition

$$\eta := \frac{\kappa_r}{\kappa}\frac{g^2}{g^2+\kappa\gamma}\ (=0.81)\ . \tag{5.58}$$

The total losses can be expressed as $L_{\rm cav} = 1-\alpha_{\rm out}^2/\alpha_0^2 = 1-\eta^2\ (=0.34)$, as measured in Fig. 2.4(a).

Henceforth, we consider the reflected light modes $|r_\uparrow\rangle$, $|r_\downarrow\rangle$ and the loss modes $|l_\uparrow\rangle := |t_\uparrow\rangle|m_\uparrow\rangle|a_\uparrow\rangle$ and $|l_\downarrow\rangle := |t_\downarrow\rangle|m_\downarrow\rangle|a_\downarrow\rangle$, which (using Eq. (5.14)) have overlaps of

$$\langle r_\uparrow|r_\downarrow\rangle = e^{-\frac{1}{2}|r_\uparrow - r_\downarrow|^2} = e^{-2\eta^2\alpha_0^2}\ , \tag{5.59}$$

$$\langle l_\uparrow|l_\downarrow\rangle = \langle t_\uparrow|t_\downarrow\rangle\,\langle m_\uparrow|m_\downarrow\rangle\,\langle a_\uparrow|a_\downarrow\rangle = e^{-2(1-\eta)\eta\alpha_0^2}\ , \tag{5.60}$$

$$\langle l_\uparrow|\,\langle r_\uparrow|r_\downarrow\rangle\,|l_\downarrow\rangle = e^{-2\eta\alpha_0^2}\ . \tag{5.61}$$

The optical pulse is reflected when the atom is in an equal superposition of $|\uparrow\rangle$ and $|\downarrow\rangle$ and after a consecutive $\pi/2$ rotation with phase θ, the atomic state is detected. The produced optical state right after reflection and state detection of the atom is

$$|\psi_{\rm out}\rangle = \frac{|r_\uparrow\rangle|l_\uparrow\rangle + e^{i\theta}|r_\downarrow\rangle|l_\downarrow\rangle}{\sqrt{2(1+e^{-2\eta\alpha_0^2}\cos\theta)}} \tag{5.62}$$

for the atom measured in $|\downarrow\rangle$, and similar with $\theta\to\theta+\pi$ for the atom in $|\uparrow\rangle$. Light in the loss modes will be dissipated to the environment. The remaining optical state ρ is obtained by tracing out the losses:

$$\rho = {\rm tr}_l\,|\psi_{\rm out}\rangle\langle\psi_{\rm out}| = \tag{5.63}$$

$$= \frac{|r_\uparrow\rangle\langle r_\uparrow|\,\langle l_\uparrow|l_\uparrow\rangle + e^{-i\theta}|r_\uparrow\rangle\langle r_\downarrow|\,\langle l_\downarrow|l_\uparrow\rangle + e^{i\theta}|r_\downarrow\rangle\langle r_\uparrow|\,\langle l_\uparrow|l_\downarrow\rangle + |r_\downarrow\rangle\langle r_\downarrow|\,\langle l_\downarrow|l_\downarrow\rangle}{2(1+e^{-2\eta\alpha_0^2}\cos\theta)} = \tag{5.64}$$

$$= \frac{|r_\uparrow\rangle\langle r_\uparrow| + e^{-2(1-\eta)\eta\alpha_0^2}(e^{-i\theta}|r_\uparrow\rangle\langle r_\downarrow| + e^{i\theta}|r_\downarrow\rangle\langle r_\uparrow|) + |r_\downarrow\rangle\langle r_\downarrow|}{2(1+e^{-2\eta\alpha_0^2}\cos\theta)} = \tag{5.65}$$

$$= \frac{|r_\uparrow\rangle\langle r_\uparrow| + e^{-2(1-\eta)\alpha^2}(e^{-i\theta}|r_\uparrow\rangle\langle r_\downarrow| + e^{i\theta}|r_\downarrow\rangle\langle r_\uparrow|) + |r_\downarrow\rangle\langle r_\downarrow|}{2(1+e^{-2\alpha^2}\cos\theta)} \tag{5.66}$$

This cat state from the cavity is identical to a cat state after generic losses (Eq. (5.32)), with initial amplitude $\alpha = \sqrt{\eta}\alpha_0$ and effective losses $L_{\rm eff} = 1-\eta\ (=0.19)$. Thus, only a part of the total cavity losses $L_{\rm cav} = 1-\eta^2$ affects the coherences. In terms of optical depth, the coherence-reducing losses $-\ln(\eta)$ are exactly half the total losses $-2\ln(\eta)$.

The Wigner function W of the cavity output state is in analogy to Eq. (5.32):

$$\begin{aligned} W(q,p) \;=\; & \frac{1}{2\pi}\Big(2\,e^{-2(1-\eta)\eta\alpha_0^2}\,e^{-p^2-(q-(r_\downarrow+r_\uparrow)/\sqrt{2}\,\alpha_0)^2}\cdot\cos(\theta+\sqrt{8}\eta\alpha_0 p) \\ & + e^{-p^2-(q-\sqrt{2}r_\downarrow\alpha_0)^2} + e^{-p^2-(q-\sqrt{2}r_\uparrow\alpha_0)^2}\Big)/(1+e^{-2\eta\alpha_0^2}\cos\theta) \end{aligned} \tag{5.67}$$

It shares the same features as the generic lossy cat state (Eq. (5.34)) but may be shifted off-center to $q = (r_\downarrow + r_\uparrow)/\sqrt{2}\,\alpha_0$, $p=0$.

A recent numerical simulation from the theory group of Klaus Mølmer confirms the creation of such a lossy cat state with an atom-cavity system [202].

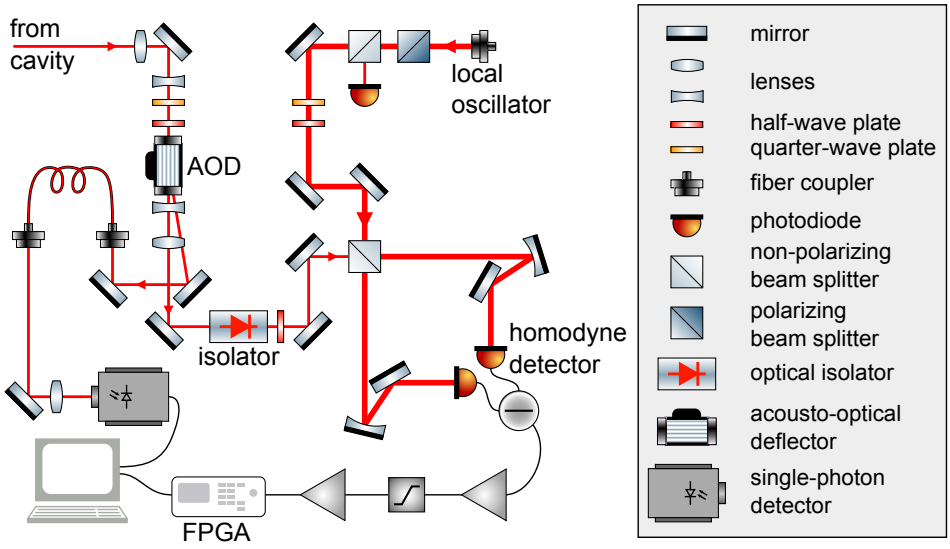

Figure 5.6.: Homodyne detection setup for continuous-variable states. The optical signal from the cavity passes an AOD in zeroth order, which can switch the beam direction into the first order onto a single-photon detector for the state detection of the atom. After an optical isolator that avoids leakage of reflected LO light, the signal is combined with the LO beam on a 50/50 NPBS. The two balanced output beams are measured on the photodiodes of the homodyne detector. The electrical current signal is then amplified, filtered and digitized by an FPGA.

5.8. Homodyne Measurement

Continuous-variable states can be fully characterized with *optical homodyne detection* [68, 167, 203]. The idea is to amplify the weak signal of an optical quantum state by interference with a strong beam, the so-called local oscillator (LO), and measure the macroscopic photocurrent on an efficient standard photodiode. The scheme was originally borrowed from radio technology, where fast modulated signals are down-mixed with a carrier-frequency that is generated locally. In this experiment, the LO is obtained from the same laser that creates the signal pulses, such that the signal path and the LO path form a Mach-Zehnder interferometer. This is often used in optical experiments, because frequency- and phase noise of the laser appear identically in the signal and the LO, and therefore cancel, as long as the path difference is shorter than the coherence length of the laser (around 400 m for the measured laser linewidth). More specifically, we applied *balanced* homodyne detection [204, 205], where the signal and LO are interfered on a 50/50 beam splitter. Both output beams are detected on two independent photodiodes and the difference of their photocurrents is recorded. This way, no signal is lost, and the maximally achievable signal-to-noise ratio can be realized. Figure 5.6 illustrates the full homodyne setup of the experiment.

Within a pulse of finite length, the detector produces an electric charge $Q_- = e \cdot n_-$ with electron charge e and the amplified difference photon number of the two detector arms n_-, which is the integrated photocurrent over the chosen temporal pulse profile (Sec. 5.8.5). The detector output current is proportional to both the LO amplitude α_{LO} and the signal amplitude q_φ, which we want to measure [68, 203].

An alternative measurement scheme to homodyning would have been heterodyning, where the LO is detuned from the signal, typically by some megahertz. Instead of a DC amplitude which yields one quadrature q_φ for a given LO angle φ, heterodyning yields both quadratures q and p at the same time, from the sine and cosine components of the detected signal.

Heterodyning has the additional advantages that electronic $1/f$ noise is less pronounced at higher frequencies and that LO light is not resonant with the atom, which can otherwise lead to scattering and decoherence (Sec. 5.8.3). However, the simultaneous measurement of the two non-commuting variables q and p comes at a cost: Only half of the available signal gets into each of the two components, which decreases their signal-to-noise ratio. One obtains a Gaussian-broadened version of the two variables, whose reconstruction results not in the Wigner function, but in a smoothed Wigner function, the Husimi Q function [206]. In that, quantum features are strongly damped to a non-recoverable level. Therefore, homodyning is the method of choice.

5.8.1. Analog Data Acquisition

The hardware in the detection setup was chosen for minimal losses and noise, because any loss that occurs up to the first amplification stage degrades the measured quantum state. The chosen photodiodes were the S3883 from Hamamatsu, which are Si PIN photodiodes with a cutoff frequency of 300 MHz and a specified spectral response of 0.58 A/W at 780 nm, which corresponds to a detection efficiency of 92%. After removal of their glass windows, the efficiency was found to be much higher, $(98.5 \pm 1)\%$ at normal incidence.

The first analog amplification stage is a LMH6624 operational amplifier with the amplification set to $2.2 \cdot 10^4$ V/A (for detailed considerations of noise spectra see [207]). To avoid clipping of the signal, it is high-pass filtered with a cutoff frequency of 0.7 kHz. This frequency was chosen to be much less than the typical signal bandwidth (Sec. 5.8.5). A second amplification stage is realized with another LMH6624 and a voltage amplification factor of 73.5, such that the total theoretical amplification is $G = 1.6 \cdot 10^6$ V/A. Together with a 50% voltage divider at the 50 Ω input of the analog-to-digital converter (ADC) the total theoretical optical difference signal amplification (through one photodiode) is $U/P = 0.51$ V/µW. The analog signal is recorded with a NI5781 ADC with a maximum bandwidth of 40 MHz and a voltage resolution of 0.12 mV. To remove slow drifts of the signal in the whole processing chain, I implemented an FPGA-based digital high-pass filter with a cutoff frequency of 1 kHz, which is active only between recordings, but keeps a fixed offset value during each signal pulse to avoid further bandwidth loss at low frequencies.

The actual system amplification, measured with a sinusoidal signal at 20 kHz, was (0.55 ± 0.02) V/µW, slightly above the theoretical value, possibly due to imprecise resistors and other analog electronic components.

5.8.2. Vacuum Signal

An important characteristic of the homodyne detector is its output spectrum for a vacuum signal, i.e. when the LO is switched on but there is no optical signal applied. The theoretical expectation is a flat white-noise spectrum [203]. Some measured spectra for LO powers up to 2 mW are shown in Fig. 5.7. Over the relevant frequency range the vacuum spectra are flat. There is some electronic pick-up noise at 15 kHz and 50 kHz and some laser noise at 10 kHz. The electronic dark noise (black line for 0 mW LO power) is equivalent to the vacuum noise of 0.05 mW.

The relevant portion of the spectrum is the range that falls into the bandwidth of the signal pulse (dashed curve in Fig. 5.7) and therefore contributes to the quadrature values. Integrated spectral powers over the Gaussian spectrum of the signal for different LO powers are shown in Fig. 5.8. A quadratic fit yields the following intensity dependence:

$$U^2/(\mathrm{mV})^2 = 0.75 + 14.85 \cdot P_{\mathrm{LO}}/\mathrm{mW} + 0.15 \cdot (P_{\mathrm{LO}}/\mathrm{mW})^2 \tag{5.68}$$

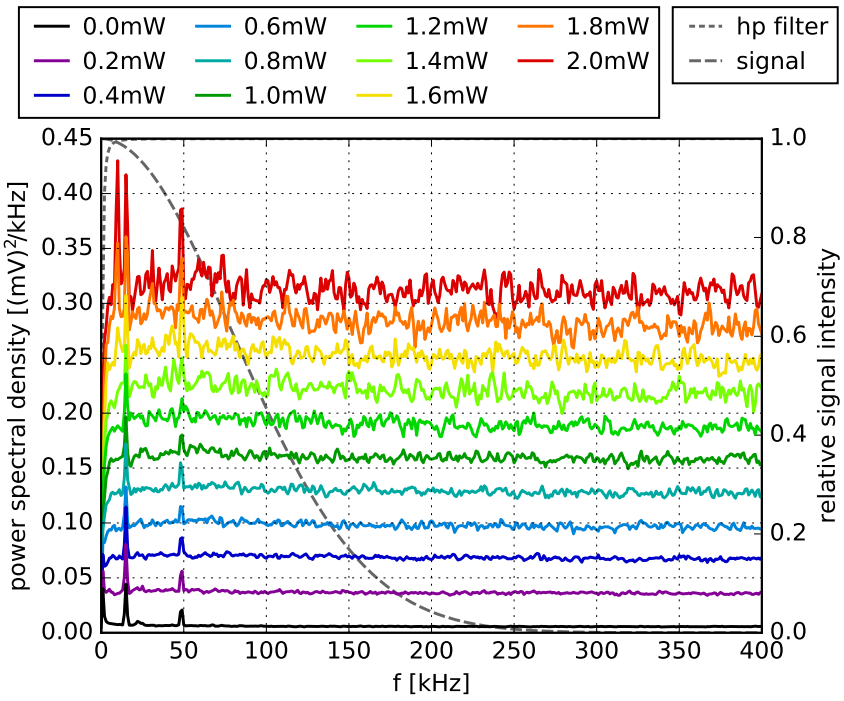

Figure 5.7.: Power spectra of the amplified vacuum. Measured spectra of the digitized homodyne signal for different values of the optical LO power with the signal beam switched off (vacuum signal). The spectra are mostly flat (within the measurement noise) and the power spectral density increases nearly linearly with the optical LO power. The dashed line shows the expected (Gaussian) spectrum of our signal and the dotted line shows the spectrum of the 0.7 kHz high-pass filter, which applies to signal and noise.

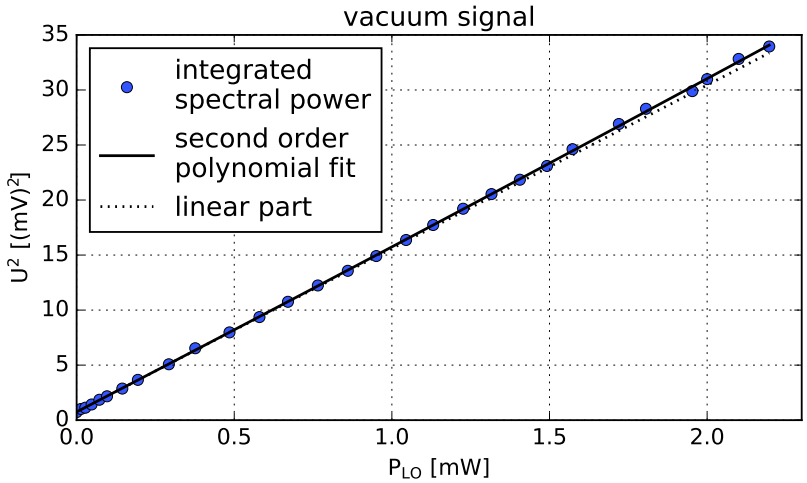

Figure 5.8.: Integrated spectral power vs. optical LO power. The integrated power of the vacuum over the Gaussian pulse spectrum scales mostly linear with the local oscillator power P_{LO}. A small constant offset and quadratic part is observed.

The constant offset is electronic dark noise, the linear part is the optical shot noise and the quadratic part is classical noise [203]. Only the linear part makes the desired signal of the vacuum quantum noise. The constant offset and the quadratic part result from additional technical noise which blur the result and act effectively similar to optical losses. At the chosen working point of $P_{\mathrm{LO}} = 1.8\,\mathrm{mW}$ the non-quantum noise amounts to 4.3% of the total voltage variance.

5.8.3. Optical Isolator

The homodyne setup is meant as a passive measurement device, which detects the state of the optical field without influencing the atom. However, when the LO beam was first switched on, the behavior of Fig. 3.4(b) was observed with the atom. The coherence time of an atomic superposition state, which is normally hundreds of microseconds, dropped to 24 µs, at an LO power of only 0.43 mW. The decoherence was caused by photons from the LO that got reflected from optical elements in the homodyne setup back into the cavity and then got scattered from the atom, causing decoherence of the qubit states. As the LO is operated at the atomic resonance frequency, the photons naturally pass all optical filters and interact with the atom. From the macroscopic power of 0.43 mW a tiny fraction of $2 \cdot 10^{-11}$ of the LO photons is enough to cause the observed decoherence, which is a realistic value for the accidental backscattering.

The problem was solved with an optical isolator (see Fig. 5.6), which prevents light from the homodyne setup from leaking into the cavity. We used an SSR780 isolator from TOPTICA Photonics with a relatively high transmission of 97%, which is critical for preserving nonclassical features of the optical states. The isolation was only around 20 dB due to imperfect alignment, but enough to extend the straylight-induced coherence time to an estimated value of $10^2 \cdot 24\,\mu\mathrm{s} = 2.4\,\mathrm{ms}$, well above the limitations imposed by magnetic fields and vector light shifts (Sec. 3.6).

5.8.4. Optical Losses in the Setup

The signal of optical states that emerge from the cavity, undergoes various losses before it is finally detected, electronically processed and saved. Because such losses are the major cause of signal degradation (see Sec. 5.4.1), we will analyze them in some detail.

Losses fall into several categories:

- Losses inside the cavity, which affect the optical state already when it is created. As we have derived in Sec. 5.7, the total intensity losses in the cavity from the impinging to the emerging beam are $L_{\mathrm{cav}} = 1 - \eta^2 = 34\%$, but the effective losses that decrease the coherence of cat states are only $L_{\mathrm{eff}} = 1 - \eta = 19\%$.
- Optical transmission losses L_{o}: Every optical element that the beam passes, induces some absorption and reflection losses. A single uncoated glass surface would already reflect 4% of an optical beam at normal incidence. Therefore every surface in the beam path has either a high-reflection or an anti-reflection coating, which reduces losses at each surface to less than 1%. The beam first passes the vacuum window, then one lens, one mirror and a dichroic filter (Fig. 3.2), and subsequently enters the homodyning setup (Fig. 5.6). In total, the beam passes one vacuum window ($L = 0.6\%$), seven mirrors ($L = 0.2\%$ each), five lenses ($L = 0.7\%$ each), three wave plates ($L = 0.4\%$ each), one dichroic filter (Semrock LL780, $L = 1.5\%$), one isolator ($L = 3.0\%$, Sec. 5.8.3), one AOD in zeroth order ($L = 2.5\%$) and one NPBS ($L = 1.5\%$). This makes the total optical losses $L_{\mathrm{o}} = 13.9\%$. Because lenses have higher

Table 5.1.: List of experimental losses. Loss channels in the experiment that were individually quantified.

Source of loss	(effective) loss	L_i	
Finite cavity reflectivity	19.0%	L_{eff}	
Lenses, waveplates, mirrors and NPBS	9.5%	L_{o}	$L_{\text{p+d}}$
Finite isolator transmission	3.0%		
Finite switch AOD transmission	2.5%		
Mode matching with LO	6.0%	L_{m}	
Finite quantum efficiency of photodiodes	1.5%	L_{d}	
Detector dark noise	2.5%	L_{n}	
LO classical laser noise	1.8%		
Electronic high pass 0.7 kHz signal reduction	1.1%		
Electronic high pass background noise	0.2%		
Total losses L_{sum}	39.3%		

losses than mirrors, the beams are focussed onto the photodiodes of the homodyne detector by curved mirrors.

- Mode-matching losses: The homodyne setup interferes the signal beam with the LO beam at a beam splitter (Fig. 5.6). This interference requires the two beams to share the same spatial optical mode, otherwise the part of the signal that is orthogonal to the LO mode will not get amplified and leaves no measurable signal in the detector. The mode matching between the two beams is limited by the beam profiles, the signal beam emerging from the cavity and the LO beam coming from a fiber coupler. Additionally, various optical elements distort the wavefront of each beam randomly. At an optimized mode matching, the effective mode matching losses were $L_{\text{m}} = 6\%$.

- Detection losses: The photodiodes of the homodyne detector were chosen for a maximal detection efficiency. With the detection efficiency found in Sec. 5.8.1, the detection losses become $L_{\text{d}} = 1.5\%$.

- Noise: Any optical or electronic noise induces random fluctuations to the measured quadrature values and therefore broadens (convolves) their distribution. As outlined in Sec. 5.4, such a broadening of the marginal distribution – and therefore the Wigner function – has the same effect as losses after the signal is renormalized to the width of the vacuum state. The effective losses induced by noise of variance var(noise) are [193]

$$L_{\text{noise}} = \frac{\text{var(noise)}}{\text{var(vacuum)} + \text{var(noise)}} \tag{5.69}$$

with the quadrature noise of the vacuum being var(vacuum) = 1/2. Therefore the effective losses by detector dark noise according to Eq. (5.68) at 1.8 mW are $L_{\text{dark}} = 2.7\%$ and by classical laser noise $L_{\text{laser}} = 1.7\%$. The electronic high-pass filter of 0.7 kHz cuts away part of the spectrum (Fig. 5.7) which amounts to a loss of $L_{\text{hp}} = 1.1\%$. The additional software high-pass filter at 1 kHz is less detrimental, because it uses a fixed offset value during each signal pulse. However, between signal pulses the filter collects noise which will randomly shift the voltage offset and causes effective losses of 0.2%. There may be other noise sources, such as slow drifts of powers and detunings, but those were not quantified.

The different losses are summarized in Table 5.1. Subsequent loss channels only affect the previously transmitted fraction, and thus the total loss is obtained by a multiplication of all transmission fractions

$$1 - L_{\mathrm{sum}} = \prod_i (1 - L_i) \; . \tag{5.70}$$

In total, the losses amount to $L_{\mathrm{sum}} = 39\%$, slightly less than the experimentally measured value from the reconstructed states $L_{\mathrm{det}} = 46\%$, which contain additional unaccounted loss channels.

All losses can be divided into two fundamental categories: Cavity losses $L_{\mathrm{eff}} = 19.0\%$, which affect the state when it is created, and propagation and detection losses $L_{\mathrm{p+d}}$ introduced thereafter. An estimate of the originally created state can be obtained from the raw data by correcting for $L_{\mathrm{p+d}} = 25\%$.

5.8.5. Temporal Optical Pulse Shape

Each experiment to create one optical state was performed within a finite temporal mode. This mode is chosen via the intensity profile of the input signal beam, which is controlled by a Direct-Digital-Synthesizer (AD9910) and applied to the laser beam through an acousto-optic modulator (AOM). For all experiments within this chapter, we chose a Gaussian intensity profile of temporal width $\sigma = 1\,\mu\mathrm{s}$, i.e.

$$I(t) = I_0 \cdot \exp\left(\frac{1}{2}\frac{(t-t_0)^2}{\sigma^2}\right) \tag{5.71}$$

The Gaussian shape was chosen because it is relatively well confined in the time- as well as in the frequency domain. The width was chosen large enough that the constant phase shift condition (Eq. (2.32)) is fulfilled and the average photon number in the cavity remains low.

The generated intensity profile, measured by the average number of single-photon detections per time bin, is shown in Fig. 5.9(a). For this measurement the average photon number per pulse was set to a large value of 14 (after losses), and the intensity follows the chosen Gaussian profile.

A single-shot voltage trace of one measurement with the homodyne detector is shown in Fig. 5.9(b). The raw signal is very noisy, because it contains the white noise of the vacuum (with the spectrum shown in Fig. 5.7), bandwidth-limited by the discrete sampling of 10 samples/µs. The signal which yields the quadrature value is contained in the temporal mode of the pulse amplitude, in this case a Gaussian of width $\sigma_{\mathrm{ampl}} = \sqrt{2}\,\mu\mathrm{s}$. A single quadrature value is obtained by the scalar product between the raw signal and the theoretical amplitude profile. In the measurement of Fig. 5.9(b), the contribution of the Gaussian mode to the signal is shown in black, and in this case yields a positive quadrature value. The high-frequency components of the raw signal do not contribute the Gaussian mode, so according to the signal spectrum (dashed gray in Fig. 5.7), which drops off above 250 kHz, a Nyquist sampling rate of 500 kHz is sufficient to obtain the quadrature value.

To calibrate the time delay of the analog processing chain, the actual signal waveform was extracted from a large number of analog data traces. Each trace however is dominated by white noise, and for uniformly distributed LO angles, the traces will average to zero. However, the common signal pulse shape in each trace can be elegantly retrieved via eigenfunction expansion [208]. To this end, I computed the mean autocorrelation matrix of a large number of measured traces and obtained the eigenmodes as the eigenvectors of this matrix. The eigenvector with the largest eigenvalue then estimates the signal waveform. One such result is shown in Fig. 5.9(c). The Gaussian waveform with $\sigma_{\mathrm{ampl}} = \sqrt{2}\,\mu\mathrm{s}$ is retrieved, and

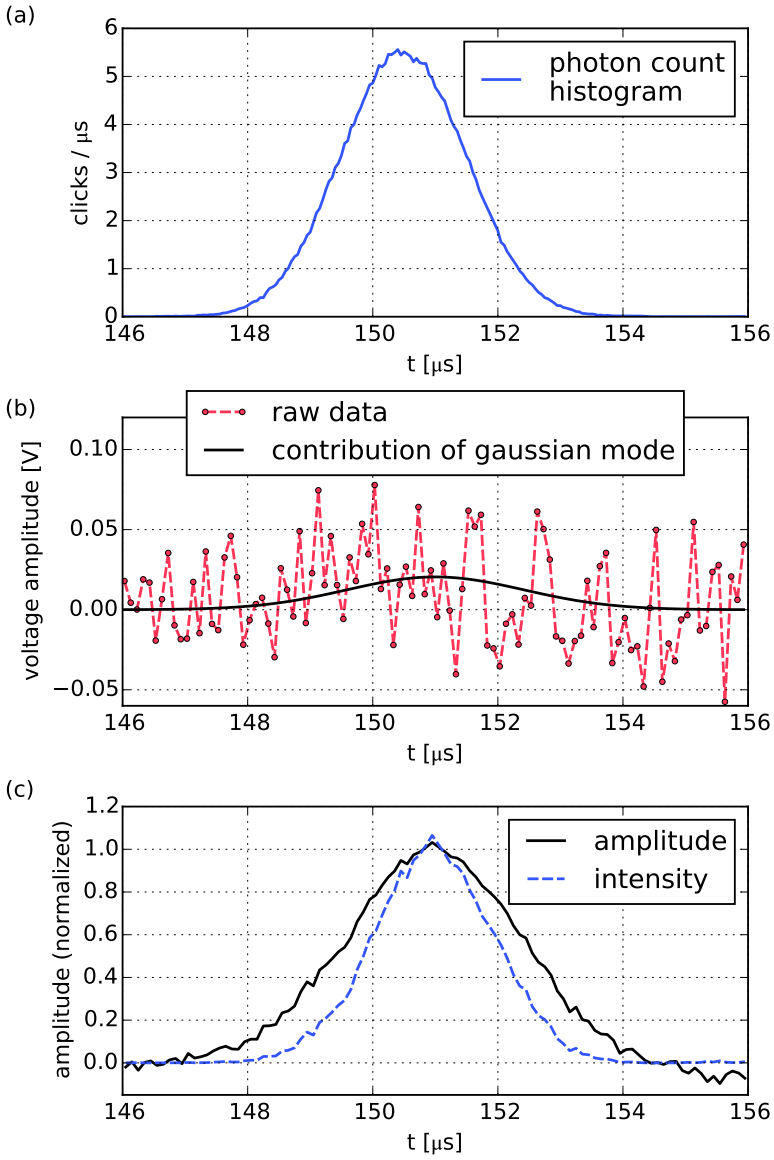

Figure 5.9.: Temporal pulse profile in the continuous-variable experiments. (a) Intensity profile of the chosen Gaussian of $\sigma = 1\,\mu s$. The histogram is composed of 394 488 single-photon detections in 28 530 experiments. (b) Voltage recording of the homodyne detector in one single experiment with 10 MHz sampling (dashed) and its contribution of the signal waveform (solid line). The raw data contains additional bandwidth-limited white noise. (c) Amplitude waveform of the homodyne signal (solid line), reconstructed from 40 453 experiments as the eigenvector with the largest eigenvalue of the autocorelation function [208]. The square of the waveform (dashed) resembles the original intensity profile from (a), with a small time-delay due to a different processing pipeline.

the corresponding intensity profile (square of the amplitude) resembles the photon click histogram of Fig. 5.9(a) with a time delay of 0.5 µs. Apparently, the reconstructed amplitude waveform becomes slightly negative for $t > 155$ µs. This behavior can be attributed to the electronic high-pass filter of 0.7 kHz right after the current amplifier.

5.8.6. Measurement of Quadratures and Phases

Each experiment consists of the preparation of an atomic state, the reflection of an optical pulse, readout of the atomic spin in a chosen basis and the recording of the optical waveform like the one in Fig. 5.9(b). The scalar product of the measured waveform with the chosen field waveform yields one quadrature value q_φ.

It is important to know the projection angle φ under which q_φ was projected from the total distribution function $W(q, p)$. The angle φ is given by the relative interferometric phase between the signal and the LO beam. This phase can be arbitrarily chosen by the

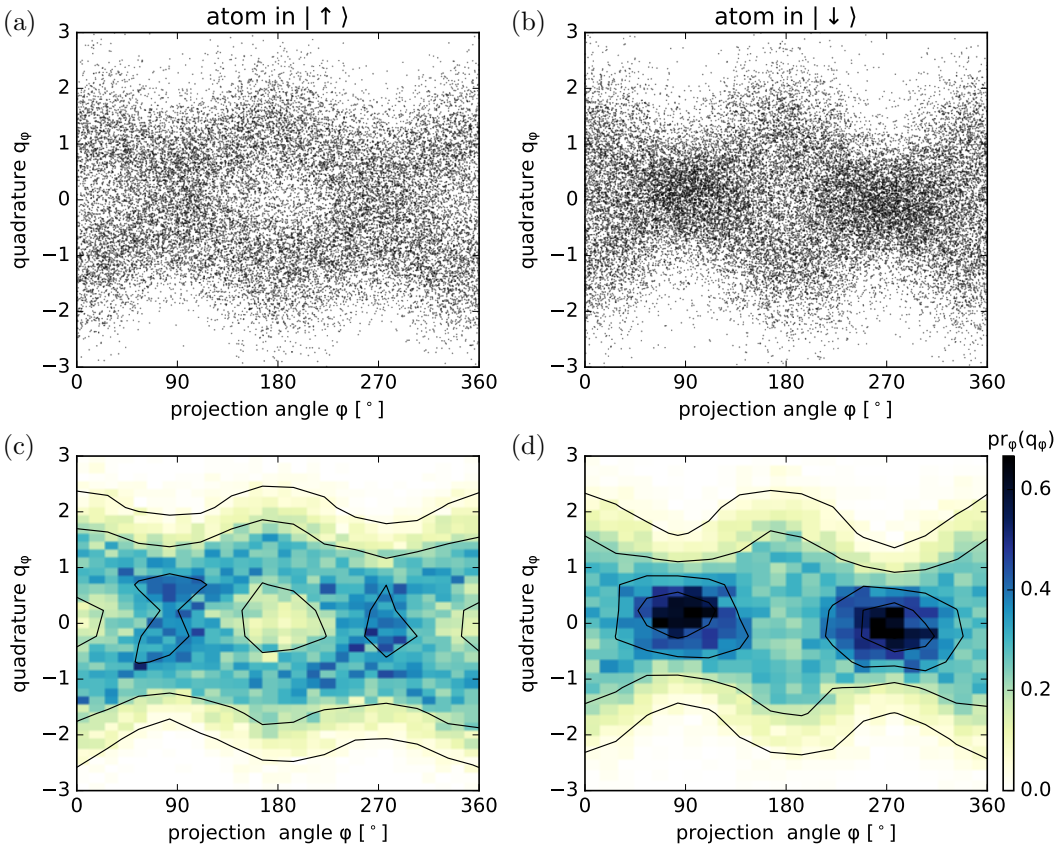

Figure 5.10.: Measured quadrature distributions. Set of quadrature values q_φ for uniformly distributed projection angles with a coherent input state of $\alpha = 0.97$. Both data sets are from the same experimental run, sorted for the outcome of the atomic state. (a) 21 711 quadrature values where the atom was $|\uparrow\rangle$ and the optical state is an odd cat state. (b) 26 522 quadrature values where the atom was $|\downarrow\rangle$ and the optical state is an even cat state. (c) and (d) are histograms for the data of (a) and (b), respectively. The even cat state is squeezed and has more concentrated quadrature distributions at 90° and 270° than the odd cat state. The atom was $|\downarrow\rangle$ in 55% of the cases, because at this small α the cat state is more likely to be even than odd (Eq. (5.24)). The measured distributions resemble the theoretical distributions of Fig. 5.4, except for a different chosen amplitude α.

path length difference between these two laser beams. Instead of actively tuning the phase, we applied a frequency offset of 1 Hz between the two beams, such that φ gradually shifts over the range of 2π during 500 subsequent experiments. After each experiment we measured the phase φ with a strong signal beam of around 10 photons per µs. This phase referencing beam is quickly swept in phase by 2π within 100 µs, while the atom is kept in the non-coupling state $|\downarrow\rangle$. A sinusoidal fit of the homodyning amplitude during this interval yields the phase φ with an accuracy of 2°.

A set of $5 \cdot 10^4$ measured phase and quadrature pairs for two small cat states of $\alpha = 0.97$ is shown in Fig. 5.10. Such a raw distribution function is sometimes called *sinogram* [209], because each point of the Wigner function leads to a sinusoidal contribution in the distribution function $\mathrm{pr}_\varphi(q_\varphi)$.

5.9. Optical Homodyne Tomography

The marginal distribution $\mathrm{pr}_\varphi(q_\varphi)$, which is sampled randomly in the experiment, is obtained from the quantum state's Wigner function $W(q,p)$ through a one-dimensional projection (Eq. (5.3)). The set of projections for all projection angles φ – the sinogram – contains the full information about $W(q,p)$. The measurable sinogram is the *Radon transform* of the not directly measurable Wigner function. Since we want to find the Wigner functions of experimentally created states, we need to infer them from measured projections. This process is called *tomography*, or more specifically optical homodyne tomography (OHT) [167]. Tomography in phase space is essentially an inverse Radon transform. To implement it, several mathematical tools have been developed and applied, namely the filtered back projection, pattern functions, maximum-likelihood reconstruction and maximum-entropy reconstruction [167]. One challenge is the presence of unavoidable quantum noise, that makes the outcome of every experiment random, and only converges to the underlying probability distribution function after a large number of individual measurements.

5.9.1. Filtered Back-Projection

The filtered back projection (FBP) is a direct numerical implementation of the inverse Radon transform. The algorithm is well established in classical computed tomography (CT), such as X-ray CT [209, 210] and has first been applied to OHT in 1993 [205].

The FBP algorithm [68, 167, 209] takes a discrete set of measured marginal distributions $\mathrm{pr}_\varphi(q_\varphi)$ for evenly spaced projection angles φ. In this experiment we chose 180 discrete angles and obtained $\mathrm{pr}_\varphi(q_\varphi)$ through binning of the measured angles and quadrature values. Each marginal distribution is then convolved (filtered) with an appropriate ramp (high-pass) convolution kernel using the fast Fourier transform (FFT) and subsequently back-projected into the phase space area to obtain $W(q,p)$.

The FBP is computationally fast and has the advantage that it makes no specific assumption about admissible shapes of the Wigner function and thus returns a relatively direct representation of the measured data. The drawback of the FBP is that it requires regularization by means of a low-pass filter (smoothing) in phase space, otherwise the result would become infinitely noisy. This smoothing however systematically broadens the Wigner function and especially dilutes narrow quantum features. Therefore one needs to choose an appropriate tradeoff between residual noise and undesired smoothing.

5.9.2. Maximum Likelihood Reconstruction in Truncated Fock Space

The Wigner function of a physical quantum state has to correspond to a physical, i.e. normalized positive Hermitian density matrix ρ. Unlike $W(q,p)$, which is a real function in two variables, ρ has only a countable number of degrees of freedom. When ρ is represented in the Fock basis $|n\rangle\langle m|$, states with well localized phase space distribution – such as cat states – only have significant populations up to a certain $n_{\max}$. Such states can be efficiently represented in truncated Fock space using a finite $(n_{\max}+1)\times(n_{\max}+1)$ density matrix.

The Wigner function of any ρ is given by Eq. (5.5) and the corresponding marginal distributions are obtained by projection along one direction in phase space, which results in [211]

$$\mathrm{pr}_\varphi(q_\varphi) = \mathrm{tr}(\Pi(\varphi,q_\varphi)\cdot\rho) \tag{5.72}$$

with the quadrature projection operator $\Pi(\varphi,q_\varphi) = |\varphi,q_\varphi\rangle\langle\varphi,q_\varphi|$ with the eigenstates $|\varphi,q_\varphi\rangle$ of the quadrature q_φ at a projection along φ. Its matrix elements in Fock space are

$$\Pi_{nm}(\varphi,q_\varphi) = \langle n|\,\Pi(\varphi,q_\varphi)\,|m\rangle = \langle n|\varphi,q_\varphi\rangle\,\langle\varphi,q_\varphi|m\rangle\ , \tag{5.73}$$

with the energy eigenstates of the harmonic oscillator

$$\langle n|\varphi,q_\varphi\rangle = \frac{e^{in\varphi}}{\pi^{1/4}\sqrt{2^n n!}} H_n(q_\varphi)\exp(-q_\varphi^2/2)\ , \tag{5.74}$$

where H_n are Hermite polynomials (in physicists' convention).[1] The quadrature projection operators $\Pi_{nm}(\varphi,q_\varphi)$ approximate a thin line in phase space at an angle φ and center-offset q_φ, whose actual finite length and width depend on the value of $n_{\max}$.

The goal is to find a density matrix ρ whose marginals $\mathrm{pr}_\varphi(q_\varphi)$ match the observed quadrature values. A popular choice is to search for the density matrix ρ that maximizes the likelihood $\mathcal{L}$ of obtaining the measured data set $\{(\varphi_i,q_i)\}$

$$\mathcal{L}(\rho) = \prod_i \mathrm{pr}_{\varphi_i}(q_i)\ . \tag{5.75}$$

This maximum likelihood (ML) technique [127] was first applied to OHT in 1999 [212] using a generic optimization algorithm. That procedure however is numerically slow, because of the intermediate number of free parameters $(n_{\max}+1)^2 \approx 100$ and the requirement to evaluate Hermite polynomials and the likelihood function for a large number $\approx 10^5$ of quadrature measurements.

A significant speedup was achieved by an iterative scheme [213] applied to OHT [211], which converges close to the ρ with maximum $\mathcal{L}$ in about 10^3 iteration steps. The algorithm gradually improves ρ using the iteration step

$$\rho^{\mathrm{new}} := N(R(\rho)\rho R(\rho)) \tag{5.76}$$

where N is the normalization and

$$R(\rho) := \sum_i \frac{\Pi(\varphi_i,q_i)}{\mathrm{pr}_{\varphi_i}(q_i)} \tag{5.77}$$

with i running over the set of measured quadratures and $\Pi(\varphi_i,q_i)$ is the projector onto the quadrature eigenstate $|\varphi,q_\varphi\rangle$ defined in Eq. (5.73). $\Pi(\varphi_i,q_i)$ remains constant during

[1] Note that the source [211] uses a different, but also widespread convention where $\hbar = 1/2$ instead of $\hbar = 1$ and thus the quadratures scale differently in phase space.

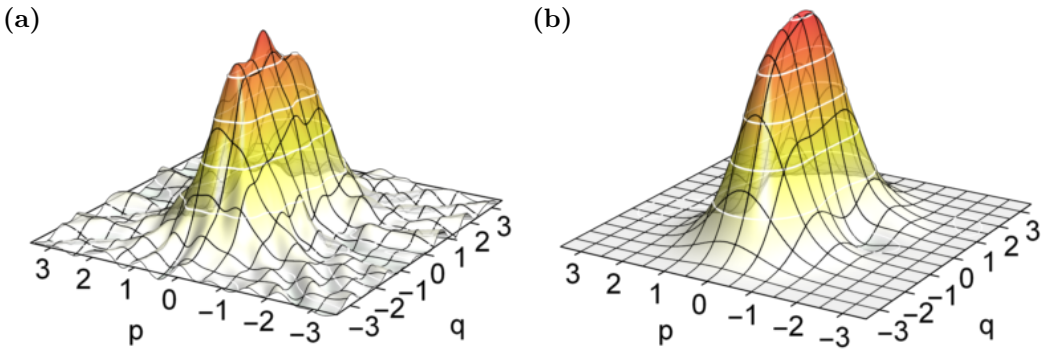

Figure 5.11.: Wigner function reconstruction. The Wigner function of a small even cat state was reconstructed from the measured quadrature data set of Fig. 5.10(b), using (a) the FBP and (b) the ML method with maximum Fock number $n_{\max} = 6$. The FBP reconstruction is noisy and has a smaller maximum value than the ML-reconstruction because of the necessary smoothing. For a state with such a small amplitude $\alpha = 0.97$, the ML method is clearly better suited. Even the two slightly negative regions next to the peak at $p = \pm 1.5$ are retrieved. Vertical mesh lines are spaced by $1/(8\pi)$.

the iteration and has to be computed only once for each data set, whereas $\mathrm{pr}_{\varphi_i}(q_i)$ has to be updated at every iteration according to Eq. (5.72). This iterative ML reconstruction is called $R\rho R$ algorithm [167] and is the workhorse to reconstruct our experimental data.

The ML reconstruction has the advantage over the FBP that it returns a physical density matrix ρ from which various properties (Sec. 5.6) can be easily derived. The associated Wigner function is smooth for small enough $n_{\max}$ and exhibits no systematic broadening. A disadvantage compared to the FBP is the much larger computing effort. Furthermore for states with larger phase space amplitudes, i.e. larger α, a larger Fock space size $n_{\max}$ is required and experimental noise as well as too much truncation can lead to artificial noise patterns in $W(q,p)$ around the phase space center.

Examples of Wigner functions reconstructed from experimental data using FBP and ML for comparison are shown in Fig. 5.11.

5.9.3. Correction for Losses

Reconstruction via the density matrix ρ brings another advantage: Optical losses can be incorporated and therefore corrected in the reconstruction. In Fock space, losses apply through the generalized Bernoulli transform (Eq. (5.28)). To find the loss-corrected density matrix ρ, the likelihood is not derived from ρ itself, but from a modified density matrix which has undergone losses. Loss correction has been introduced to OHT in 1995 [214].

In fact, many of the losses in our experiment (Sec. 5.4) are technical transmission and detection losses, that are introduced in the homodyne detection setup. The state of interest, however, is the one that is originally produced as it leaves the cavity. Figure 5.12 shows the effect of loss correction on experimental data. An odd cat state recorded at the detector displays a strongly damped fringe pattern in the phase space center. The visibility improves when propagation and detection losses are compensated for (Fig. 5.12(b)), and even more, when the full amount of losses in the system is compensated for (Fig. 5.12(c)). However, the visibility does not become as large as in a lossless theoretical state (Fig. 5.12(d)), because additional imperfections such as phase noise (Sec. 5.9.5) are present.

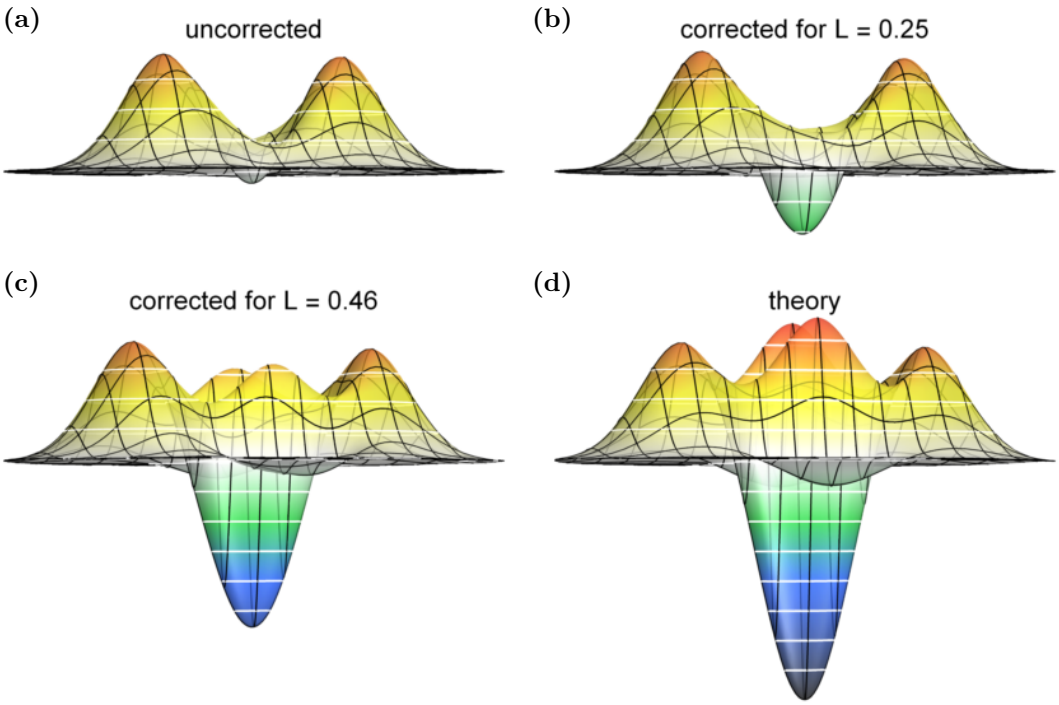

Figure 5.12.: Reconstructed odd cat state with and without loss correction. The Wigner function of a measured odd cat state with $\alpha = 1.4$ (before losses) was reconstructed using the ML method. (a) Direct reconstruction without loss correction. The Wigner function reaches a minimum of -0.016 ± 0.004 in the center. (b) Same data set corrected for $L_{\mathrm{p+d}} = 0.25$ (see Tab. 5.1), an estimate for the state that is originally created. (c) Same data set corrected for all losses $L_{\mathrm{det}} = 0.46$. The fringe visibility is still less than an ideal cat state of the same size (d), because the measured data is broadened in azimuthal direction around the phase space origin (phase noise). The ideal cat state (d) reaches a minimum value of $-1/\pi$. Horizontal mesh lines are spaced by $1/2$ and vertical mesh lines by $1/(8\pi)$.

5.9.4. Estimation of Statistical Uncertainties

Uncertainties in ρ (of size $n \times n$) are expressed by a covariance matrix $\mathrm{cov}(\rho)$ of size $n^2 \times n^2$ which contains the variance of each element of ρ as well as the covariance of each pair of elements. The covariance matrix can be obtained directly from the likelihood function $\mathcal{L}$ (Eq. (5.75)) as the negative inverse of the Hessian matrix H of $\ln \mathcal{L}$ [128] (Eq. 5.35 therein). To this end, ρ is parametrized by a real vector t:

$$-\,\mathrm{cov}(\rho)^{-1}(t)_{ij} = H_{ij}(t) = \frac{\mathrm{d}^2 \ln \mathcal{L}(\rho(t))}{\mathrm{d}t_i\,\mathrm{d}t_j} \tag{5.78}$$

This differentiation is achieved numerically using finite differences. The normalization constraint of ρ requires an additional correction term for $\mathrm{cov}(\rho)$, which is given in [212].

Knowledge of the covariance matrix $\mathrm{cov}(\rho)$ allows us to derive statistical uncertainties for all quantities $f(\rho)$ that are functions of ρ, such as photon numbers, values of the Wigner function and entanglement measures, using the law of error propagation [128]:

$$\mathrm{cov}(f) = J_f \cdot \mathrm{cov}(\rho) \cdot J_f^T \tag{5.79}$$

where J_f is the Jacobian matrix $J_{ij} = \partial f_i / \partial \rho_j$ that describes how f changes with ρ (again parametrized as a real vector with entries j). J_f is also obtained numerically using difference quotients.

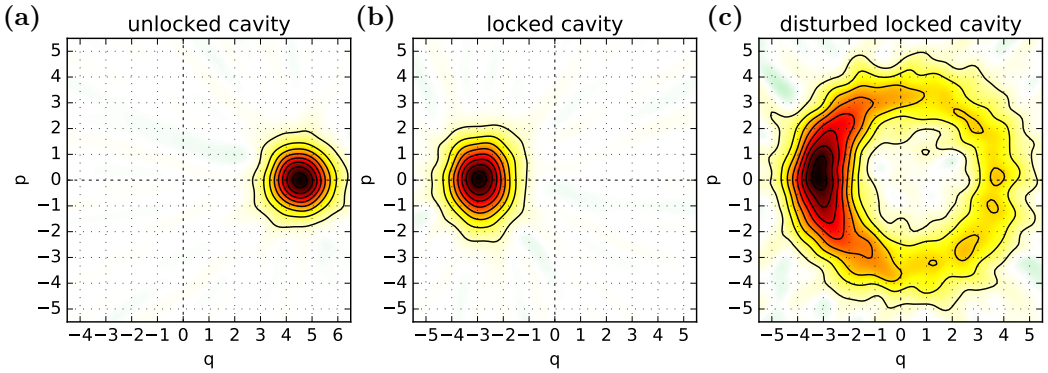

Figure 5.13.: Wigner functions for coherent pulses, reflected off (a) the unlocked cavity, (b) the locked cavity and (c) the locked cavity while scratching the optical table. The fitted RMS phase noise on top of the width of an ideal coherent state is 0.01π, 0.05π and 0.39π, respectively. The Wigner functions were reconstructed with the FBP method, and the color scales are normalized to each maximum.

5.9.5. Cavity Phase Noise

The main ingredient for cat states, coherent light pulses, are prepared almost ideally from a narrow line-width laser beam. When reflected from the incoupling mirror of a far off-resonance cavity, the coherent state is well preserved (Fig. 5.13(a)). The reconstructed coherent peak exhibits an additional azimuthal broadening of 0.01π, caused by the inaccuracy of determining the LO phase as well as smoothing from the FBP reconstruction.

When the cavity is locked on resonance, any reflected light will get a phase shift that depends on the exact offset frequency between the incoming beam and the cavity resonance (Sec. 2.6). The linewidth of the laser (250 kHz) and residual fluctuations of the cavity lock (150 kHz RMS) lead to additional random phase-shift variations. The coherent pulse reflected from the locked cavity (Fig. 5.13(b)) is on average phase-shifted by π, reduced in amplitude by a factor of $\eta = 0.81$, and spread in azimuthal direction by 0.05π as expected from the frequency noise.

It is easily verified that an additional azimuthal spread is caused by fluctuations of the cavity frequency. When the cavity lock is mechanically disturbed, e.g. by scratching the optical table, the phase-space distribution broadens significantly (Fig. 5.13(c)).

5.9.6. Veto Herald

The most fundamental imperfections in the creation of cat states are optical losses inside the cavity, as described in Sec. 5.7. The loss channels are mirror scattering losses m, scattering via the atom a and cavity transmission losses t. The scattered light leaves the system into a large solid angle or into the mirror material and is therefore hard to capture. The transmitted light through the cavity, however, propagates in a well-defined spatial mode $|t\rangle$ and can be directed onto a single-photon detector ("cavity transmission output" in Fig. 3.2). Such an arrangement can be used as a veto herald in the following way: When the SPD clicks (ignoring dark counts), a photon was definitively lost and the cat state is known to be degraded. In this case the signal can be used as a veto and the cat state can be discarded. If the SPD does not click, it will project the transmitted light into a vacuum state, at least when the detection efficiency η_{det} is unity, so it acts as a herald for reduced losses in the reflection mode. The created cat state will then exhibit less losses [215]. Recoverable transmission losses (Eq. (2.19)) are $T_{\downarrow} = 10\%$ and $T_{\uparrow} = 0.13\%$ for the parameters of this experiment. As this improvement of the quality of cat states would render the the experiment slightly probabilistic, it was eventually not applied.

5.10. Cat-State Results

The protocol of Sec. 5.3 with a coherent input state of $\alpha = 1.4$ creates the output shown in Fig. 5.14 and Fig. 5.15. One observes the characteristic Wigner functions with two Gaussian peaks and interference fringes in the center, as described by Eq. (5.34). Data selected for the atom in $|\downarrow\rangle$ represent an even cat (left column) and data selected for $|\uparrow\rangle$ represent the odd cat (right column). The even cat state displays a local maximum and the odd cat state a minimum at the center of the Wigner distribution. A fit of theoretical cat states with losses to the measured Wigner function yields an effective loss of $L_{\mathrm{det}} = 46\%$. The fidelities of these measured states with ideal even and odd cat states are $(59.2 \pm 0.6)\%$ and $(51.2 \pm 0.6)\%$, respectively. Applying a correction for 25% combined propagation and detection loss $L_{\mathrm{p+d}}$ (Fig. 5.15, bottom row and Fig. 5.14), the fidelities reach $(68.0 \pm 0.9)\%$ and $(62.8 \pm 0.8)\%$, respectively.

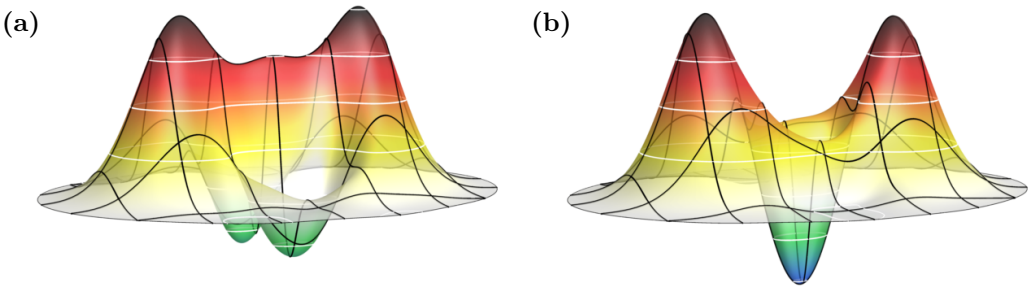

Figure 5.14.: 3D Wigner functions of measured cat states. (a) Even cat state and (b) odd cat state. Horizontal mesh lines are spaced by 1 and vertical mesh lines by $1/(8\pi)$. Both states were corrected for 25% propagation and detection losses.

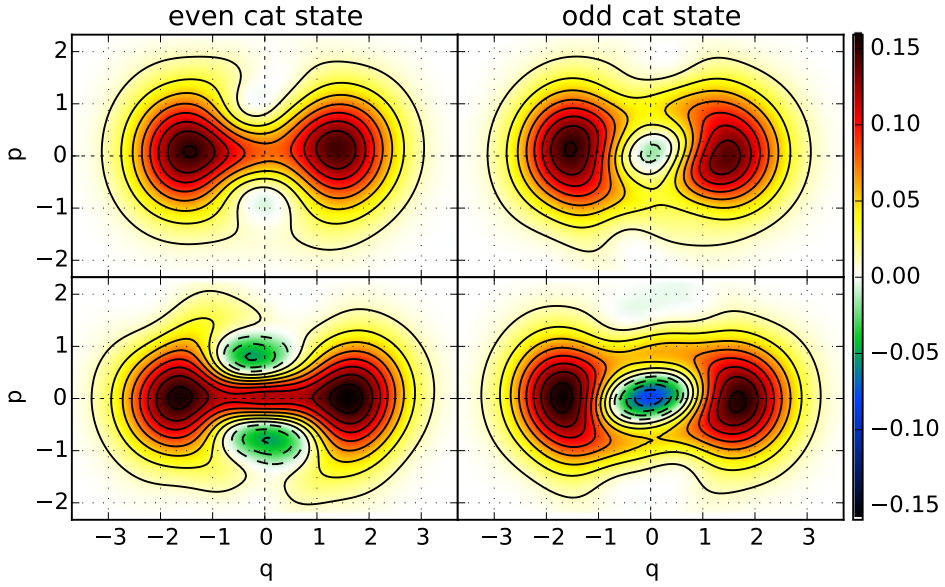

Figure 5.15.: Experimentally created even and odd cat states with $\alpha = 1.4$. The top row is without any loss correction. Even (left column) and odd cat states (right column) differ significantly, and negative regions in the Wigner function appear. The bottom row shows the same data corrected for propagation and detection losses $L_{\mathrm{p+d}} = 25\%$, identical to the states depicted in Fig. 5.14. (from [137])

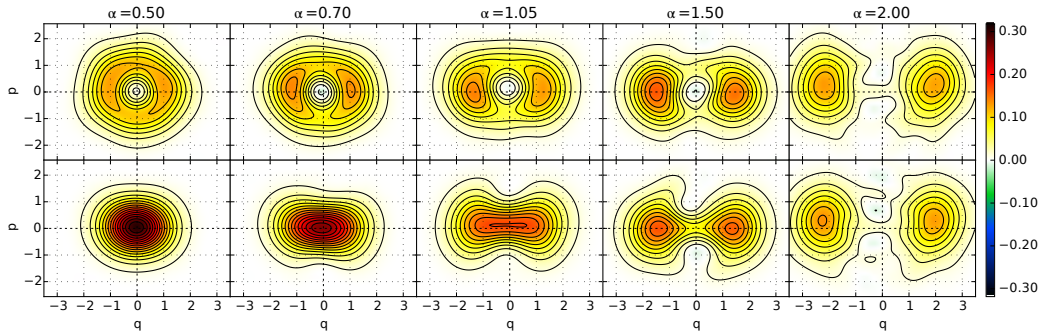

Figure 5.16.: Varying the cat size α. Odd (top row) and even (bottom row) cat states for varying amplitudes α between 0.5 and 2. The most significant negative values are observed for $\alpha = 1.4$. Above $\alpha = 2$ the interference fringes become dominated by noise. (from [137])

Any difference of the coherence fringes between the two Wigner functions for $|\uparrow\rangle$ and $|\downarrow\rangle$ demonstrates that the optical states are not mere mixtures of $|\alpha\rangle$ and $|-\alpha\rangle$ but (at least partially) coherent superpositions. A characteristic feature of cat states, which has no classical explanation, is the existence of negative regions in the Wigner function. The measured odd cat state has a minimum value of

$$\min(W) = -0.016 \pm 0.004 \tag{5.80}$$

without loss correction, in line with the theoretical expectation from Eq. (5.45) ($\min(W) = -0.012 \pm 0.004$ for $L = 0.46 \pm 0.01$ and $\epsilon = 0.02 \pm 0.01$). When propagation and detection losses $L_{\mathrm{p+d}} = 25\%$ are corrected for, the minimum value becomes $\min(W) = -0.083 \pm 0.005$ (Fig. 5.14, 5.15).

With different amplitudes of the coherent input pulse, cat states of various sizes can be produced. Figure 5.16 shows five pairs of cat states between $\alpha = 0.5$ and $\alpha = 2$. At small α, even (bottom row) and odd (top row) cat states approach the zero- and one-photon Fock states, respectively. With increasing α, the two coherent peaks separate. For values above $\alpha = 2$, interference fringes get increasingly damped by optical losses.

5.10.1. Properties of Measured Cat States

Every experiment yields two results, one outcome of the atomic state detection, and one projection of the photonic state to a quadrature value. The average outcome of the atomic state detection is shown in Fig. 5.17. When no light is reflected from the cavity ($\alpha = 0$), the atom always ends up in $|\downarrow\rangle$ after two $\pi/2$ rotations from $|\uparrow\rangle$ in the protocol. With increasing optical amplitude, the probability for the final atomic state approaches 50% for both $|\uparrow\rangle$ and $|\downarrow\rangle$, which is due to entanglement with the light field Eq. (5.18) (see Sec. 5.10.4 for details). The measured value of the relative frequency $P(\uparrow)$ can be used to infer the amplitude α inside the cavity, independent of optical mode matching (Sec. 3.9) or optical losses (Sec. 5.4.1). It is therefore a means to calibrate the total losses in the experiment $L_{\mathrm{det}} = 0.46$.

Fringe Visibility

Let us turn to the optical output of the experiment, our cat states. Their most essential feature are the interference fringes in phase space at the center between the two coherent state peaks. The coherence manifests most clearly in the difference between two

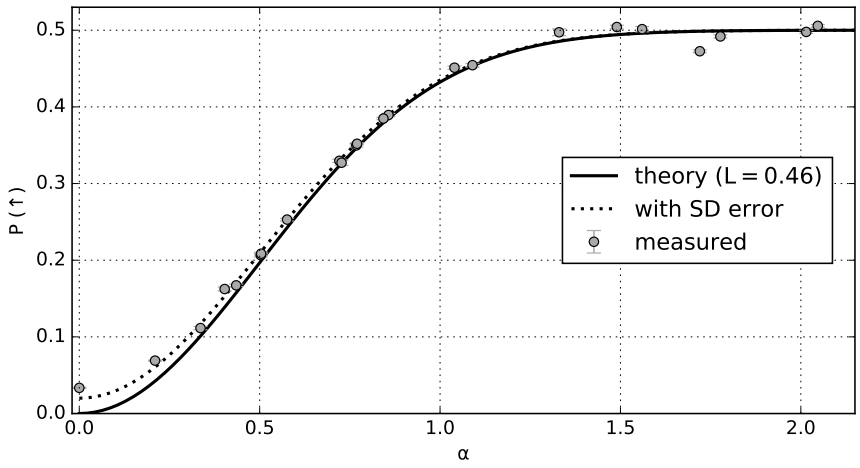

Figure 5.17.: Probability to detect the atom in $|\uparrow\rangle$. When coherent pulses of various amplitudes α are reflected from the cavity, the final state detection of the atom at the end of the protocol (Fig. 5.2) results in the relative frequencies $P(\uparrow)$ shown here. The theoretical expectation from Eq. (5.24) with ideal state detection ($s = 1$) is plotted as the solid line. Taking imperfect atomic state detection (Sec. 5.5) into account, $P(\uparrow) = (1 - s \cdot \exp(-2\alpha^2))/2$ (dotted line with $s = 0.96$), closely followed by the experimental data.

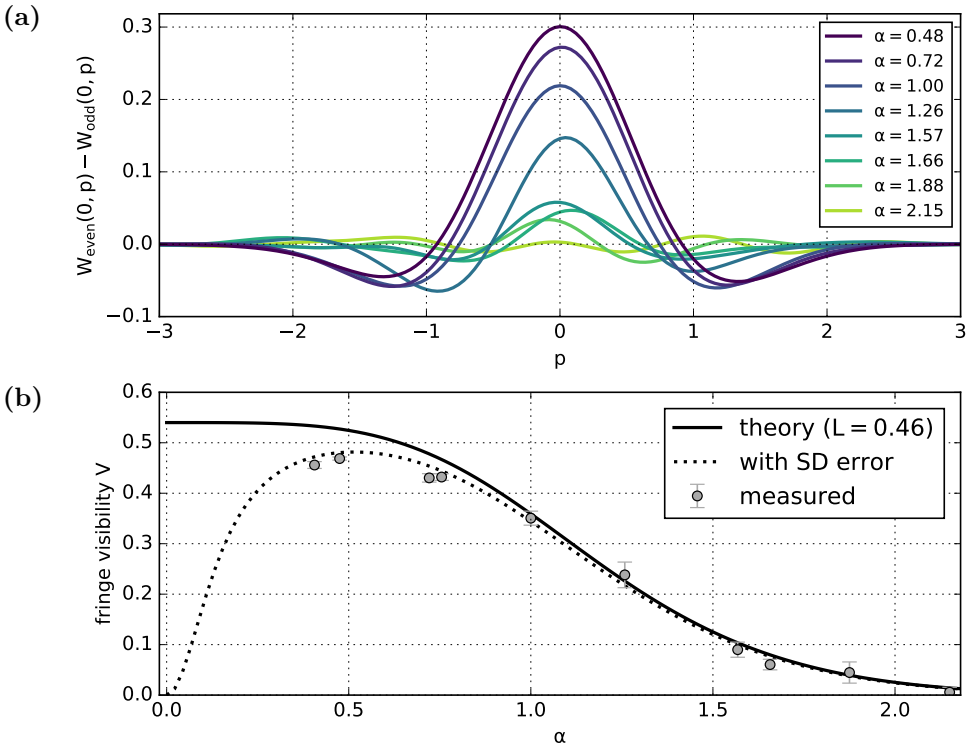

Figure 5.18.: Interference fringe visibility of measured Wigner functions. (a) Slices of the Wigner function differences for simultaneously measured even and odd cats $W_{\mathrm{even}} - W_{\mathrm{odd}}$ along p at $q = 0$ show the interference fringes. Their oscillation frequency increases with α and their amplitude gets damped for larger alpha due to losses. (b) The fringe visibility V for various α behaves according to Eq. (5.46). The solid line shows the theoretical expectation with experimental losses L_{det} at the detector, which reduce the visibility with increasing α. For α close to 0, errors in the atomic state detection dominate and cause the visibility to drop (dotted line with $\epsilon = 2\%$). All data points are without correction for optical losses. Error bars depict statistical standard errors.

Wigner functions for opposite atomic state outcomes, such as $W_{\mathrm{even}} - W_{\mathrm{odd}}$, which vanishes completely for incoherent mixtures. Figure 5.18(a) shows cuts along p across the fringes of ML-reconstructed Wigner functions of various α. With increasing α, the oscillation frequency increases proportionally as $\sqrt{8(1-L)}\alpha$, while the amplitude drops asymptotically like $\exp(-2L\alpha^2)$ (Eq. (5.46)). Fitted amplitudes of these oscillations are shown in Fig. 5.18(b), together with theory curves including losses and imperfect atomic state detection of $\epsilon = 2\%$.

Photon Statistics

The photon-number distribution $P(n)$ of reconstructed states is the diagonal of their density matrix in the Fock basis. Apart from the ML reconstruction, one can obtain $P(n)$ through direct sampling of the phase-averaged quadrature distribution using the overlap integral with so-called pattern functions [167], however with much larger statistical uncertainties. The average photon number $\overline{n}$ through direct sampling is obtained as [216]

$$\overline{n} = \langle q_\varphi^2 \rangle_\varphi - 1/2 \,, \tag{5.81}$$

which follows from the definition of the quadrature operators (Eq. (5.1)) and $\hat{n} = \hat{a}^\dagger \hat{a}$. Such a direct evaluation may have less bias than through the ML-evaluated density matrix, but we find in general good agreement between the two methods. Figure 5.19 shows the measured average photon numbers for pairs of even and odd cat states, determined by Eq. (5.81). In these measurements, the LO phase was swept constantly, such that the quadrature distribution is indeed averaged uniformly over all values of φ. The measurements follow the theoretical expectations of Eq. (5.40), with $\overline{n}$ of odd cat states larger than for even ones and an asymptotic approach towards $(1-L)\alpha^2$ for large α.

The photon statistics are also predicted to deviate from Poissonian statistics, which is quantified by the Mandel Q parameter Eq. (5.42). Experimental results are presented in

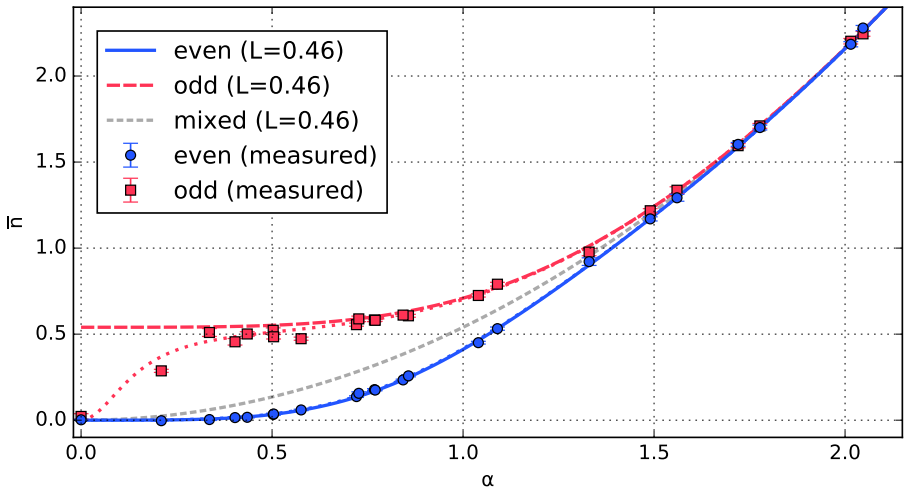

Figure 5.19.: Average photon number in measured even and odd cat states. Without consideration of the atom, a coherent output state after losses L would have the average photon number $\overline{n} = (1-L)\alpha^2$ (grey dashed line). A post-selection on the atom for even (blue, solid line) and odd (red, dashed line) cat states results in different average photon numbers for small α. The measured data follow the theoretical model. The dotted lines include the effect of imperfect atomic state detection of $\epsilon = 2\%$.

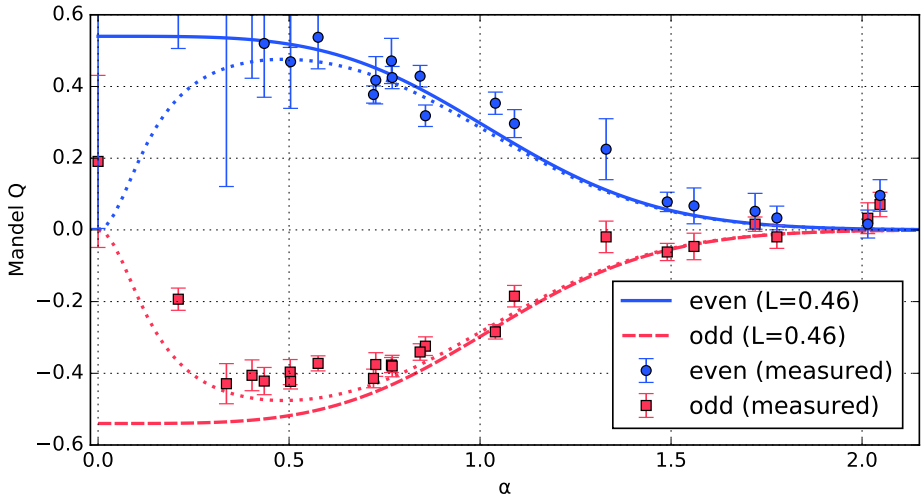

Figure 5.20.: Measured Mandel Q parameters for even and odd cat states. For small α, the Q parameter becomes positive for even cat states (blue, solid line) and negative for odd cat states (red, dashed line). Close to $\alpha = 0$, state detection errors (dotted lines for $\epsilon = 2\%$) bring the Q parameter to 0 instead of $\pm(1 - L)$.

Fig. 5.20. The data exhibit very significant differences between even and odd states, in agreement with the theoretical model. Odd cat states are sub-Poissonian and even cat states are super-Poissonian. For large α, the differences vanish, not because of losses but as a general property of cat states.

Fidelity

Figure 5.21 shows measured fidelities of even and odd cat states with ideal lossless cat states of equivalent amplitudes. When α is large enough that the Gaussian peaks do not overlap, the fidelity acquires up to 50% from the two coherent Gaussian peaks and another 50% from the coherent interference pattern. Thus, at finite losses, fidelities tend towards 50% for large α. Apart from this behavior, for α close to 0, the even cat states tend towards unity fidelity because the ideal even cat state approaches the vacuum. In contrast, odd cat states tend towards fidelity 0, because even small atomic state detection errors produce a dominating admixture of even cat states (dotted line, Sec. 5.5). One can also observe a drop of the measured values below the theory curves at large α, which is caused by a phase uncertainty that broadens the coherent Gaussian peaks in phase space (Sec. 5.9.5) and reduces their fidelity contribution below 50%.

Purity

The purity of an ideal cat state is unity and drops towards 0.5 for an incoherent mixture of two coherent states with little overlap of the two coherent components. The experimental data, shown in Fig. 5.22, quickly drop towards 0.5 due to loss-induced decoherence. Similar to the fidelity, the purity at very low α is 1 because the vacuum is pure, and the values for large α show an additional drop due to azimuthal noise in phase space (Sec. 5.9.5).

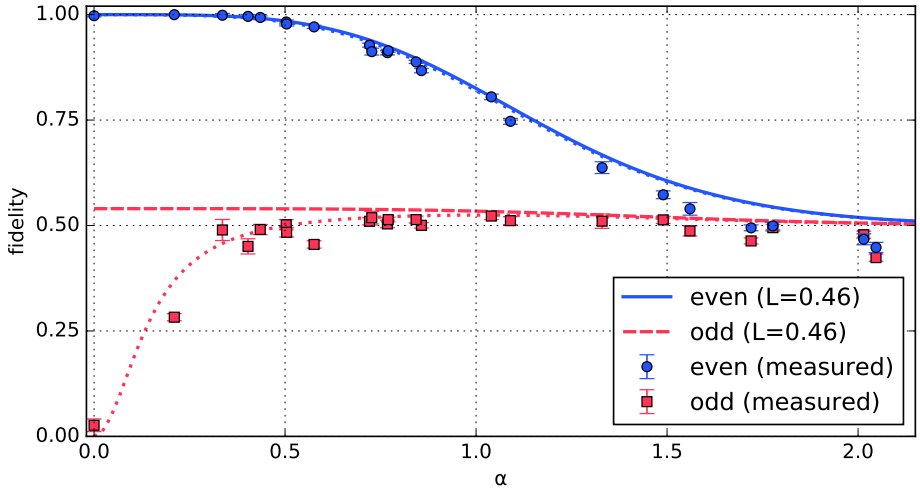

Figure 5.21.: Measured fidelity of even and odd cat states. At large α, where losses dominate, theoretical fidelities for both even and odd cat states approach 50%. At α close to 0, the even cat states approach the vacuum, where the fidelity becomes unity, whereas odd cat states reach maximally $1 - L$. State detection errors of $\epsilon = 2\%$ (dotted lines) decrease the fidelity further. An additional drop is observed for $\alpha > 1.5$, due to phase uncertainties associated to cavity vibrations, which are not included in the model.

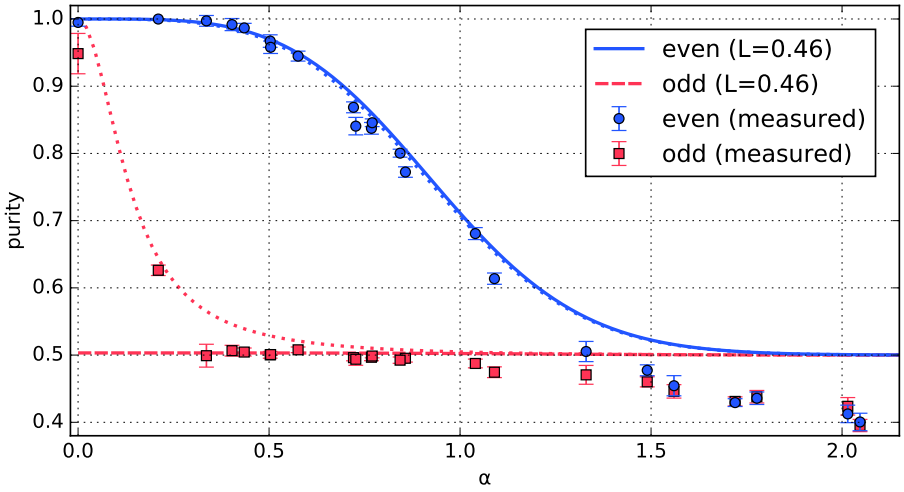

Figure 5.22.: Measured purity of even and odd cat states. Theoretical models with losses and experimental data are shown for even (solid blue line) and odd states (dashed red line). The dotted lines include additional state-detection errors of $\epsilon = 2\%$.

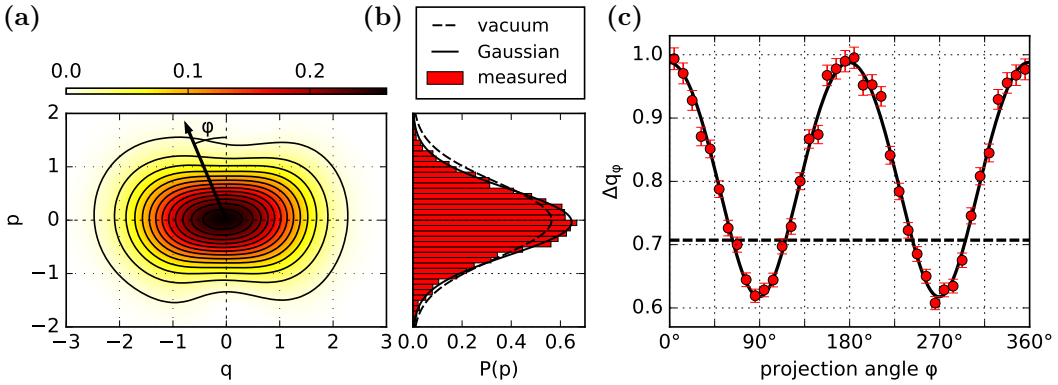

Figure 5.23.: Experimentally measured squeezed even cat state with $\alpha = 0.7$. (a) Reconstructed Wigner distribution from $\approx 7 \cdot 10^4$ measured quadrature values using the ML reconstruction in Fock space without loss-correction. The arrow shows the projection direction along p_φ used in (c). (b) Histogram of measured quadrature values for projection angles in the interval $90° \pm 5°$. The solid curve is a normalized Gaussian with the same mean value and spread as the measured distribution. The dashed curve shows the respective distribution of a vacuum state. (c) Standard deviation (including Bessel's correction) of directly measured quadrature values Δq_φ vs. projection angle φ given by the relative phase of the local oscillator. Fitted values range from 0.62 (squeezed) to 0.99 (anti-squeezed). The vacuum noise level is at $1/\sqrt{2}$ (dashed line). (from [137])

Squeezing

Pure coherent states have a fixed spread in phase space $\Delta q = \Delta p = \sqrt{1/2}$ with the convention used in this work. Larger spreads are easily achieved, for instance when different states are mixed. The minimum spread however has to obey the uncertainty principle $\Delta q \cdot \Delta p \geq 1/2$ for the two non-commuting variables q and p. A state with a spread lower than the vacuum value in any direction is called *squeezed* [194].

The p-quadrature variance of a lossy cat state (Eq. (5.50)) for the even cat ($\theta = 0$) is always narrower than the vacuum as long as $(1 - L)\alpha^2 > 0$. The squeezing is most pronounced when the amplitude is around 1, regardless of the amount of losses.

The experimental realization of a squeezed state with $\alpha = 0.7$ is shown in Fig. 5.23. At this low α the two coherent contributions are merged into one single peak at the phase space center. In comparison to the vacuum state, the state is anti-squeezed in q-direction ($\Delta q = 0.99$) and squeezed in p-direction ($\Delta p = 0.62 = 0.87 \Delta p_{\text{vac}}$), fulfilling the uncertainty principle.

A fluctuation in the measured projection angle of $\Delta\varphi$ causes a random rotation of the Wigner function in phase space and thus a broader marginal distribution with increased Δp. Coherent peaks of a cat state with size α are located at $q = \pm\sqrt{2}\alpha$. The additional variance due to a variation in φ is therefore $(\Delta p_\varphi)^2 = 2(1 - L)\alpha^2(\Delta\varphi)^2$. The variances of independent contributions add up, such that the total quadrature variance becomes

$$(\Delta p)^2 = \frac{1}{2} - \frac{2(1 - L)\alpha^2}{e^{2\alpha^2} + 1} + 2(1 - L)\alpha^2(\Delta\varphi)^2 \,. \tag{5.82}$$

This behavior can be seen in Fig. 5.24, where the p-variances of even and odd cat states are shown for different values of α. Squeezing is present up to $\alpha = 1.15$. The fit of Eq. (5.82) reveals $\Delta\varphi = 0.06\pi$, similar to the phase spread observed in Sec. 5.9.5.

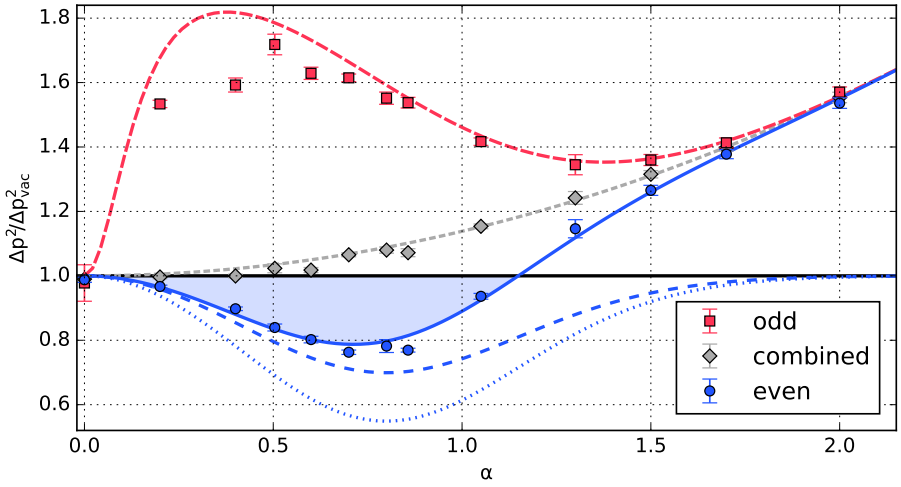

Figure 5.24.: Measured variances of the p-quadrature for cat states of different amplitudes. Even cat states are squeezed with reduced Δp for low α (light blue area), with a maximum squeezing of 1.18 ± 0.03 dB. The dotted and dashed blue lines show the theoretical prediction for even cat states with losses $L_{\text{eff}} = 0.19$ and $L_{\text{det}} = 0.46$ for the states right after the cavity and at the homodyne setup, respectively. The full model for even (solid blue), odd (dashed red) and combined (dashed gray) cat states contains atomic state-detection errors of 2%, important at small α, and random noise in the phase angle φ, important at larger α. The latter limits the observable squeezing to states with $\alpha < 1.15$.

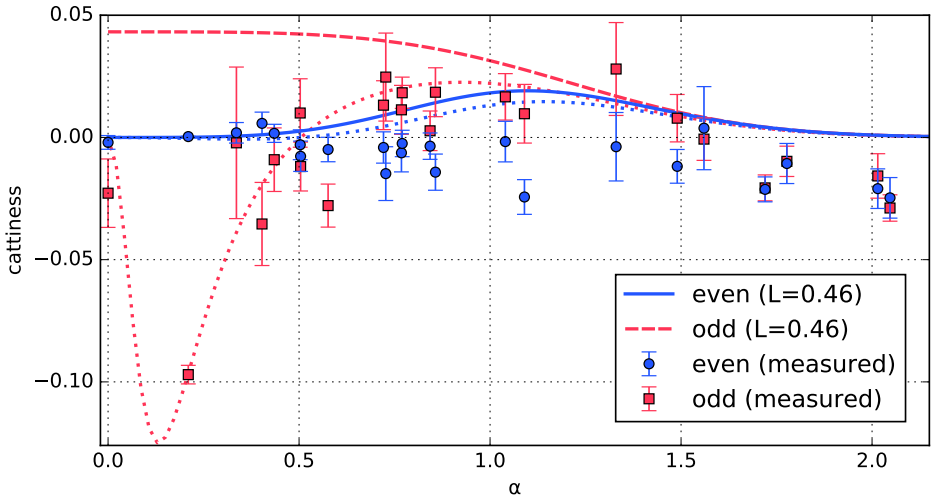

Figure 5.25.: Measured cattiness of even and odd cat states. The theory predicts very low values both for even and odd cats, due to the significant losses. The data confirm that the cattiness does not become significantly positive. With state-detection errors of $\epsilon = 2\%$ included (dotted lines), the cattiness may even turn negative.

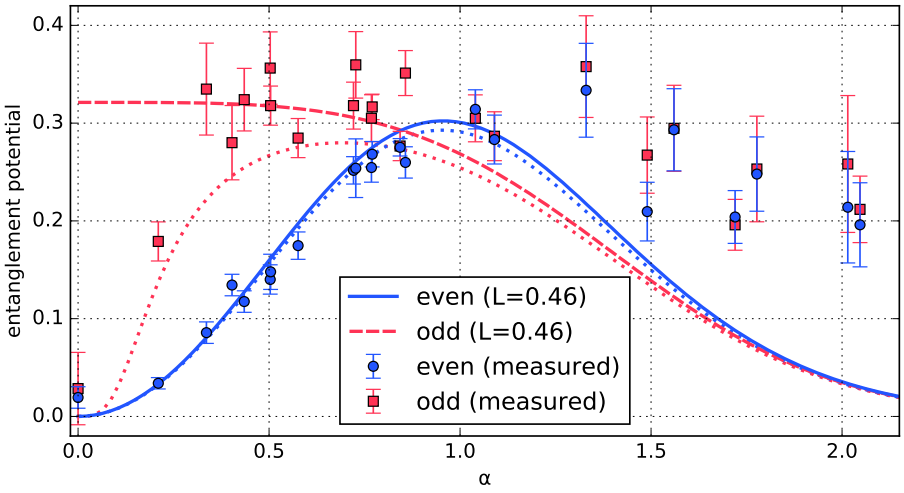

Figure 5.26.: Measured EP for even and odd cat states. For small $\alpha < 1$ the measurements agree well with the theory and show significant EP, even with state-detection errors (dotted lines). Above $\alpha = 1$, the data over-estimate the EP due to statistical noise and Fock-space truncation.

Cattiness

The cattiness of measured cat states is plotted in Fig. 5.25. In accordance with the theory (Eq. (5.54)), the measured values do not reach significantly above 0. The cattiness is a very strict measure that requires both large amplitudes and large fidelities at the same time, which cannot be achieved at presence of a significant amount of losses.

Entanglement Potential

The entanglement potential (EP) quantifies the non-classicality by how much the two outputs would be entangled if the state is split by a beam splitter. Results are shown in Fig. 5.26. Measured cat states of intermediate size around $\alpha = 1$ exhibit significant amounts of EP which is expected to persist for arbitrarily large finite losses [144]. Measured values at larger α clearly exceed the theoretical expectation. As simulations have shown, this effect is due to experimental noise and the necessary Fock-space truncation in the density matrix reconstruction. The EP is somewhat too sensitive and care has to be taken in order to use it as a reliable measure.

5.10.2. Generalized Cat States

The even and odd cat states shown so far are special cases of more general coherent-state superpositions of the form

$$|\mathrm{cat}\rangle = \frac{\cos(\xi/2)|\alpha\rangle + e^{i\theta}\sin(\xi/2)|e^{i\phi}\alpha\rangle}{\sqrt{1 + e^{-2|\alpha|^2\sin^2(\phi/2)}\cos(\theta + |\alpha|^2\sin\phi)\sin\xi}} \tag{5.83}$$

with parameters α, ϕ, θ and ξ. This experiment allows the control of all those parameters, the modulus and the complex phase of α, the optical phase ϕ between the coherent contributions, the superposition phase θ that determines even or odd cat states and the population fraction of the two coherent contributions ξ. This control opens the possibility to create more complex states that are required for continuous-variable error correction codes [181, 183, 184].

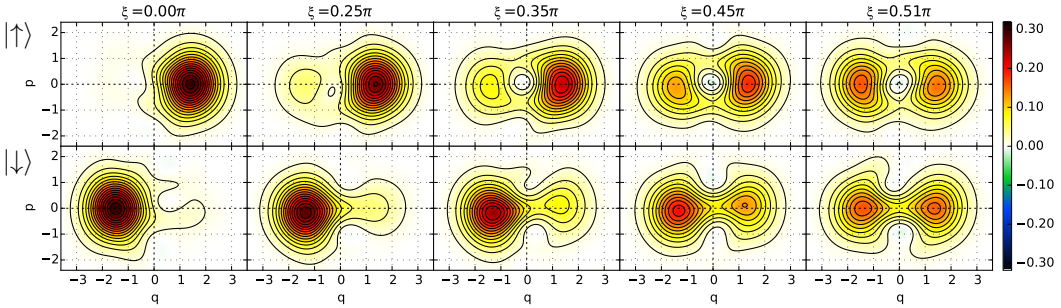

Figure 5.27.: Varying pulse area ξ. Wigner functions for varying pulse area ξ of the final spin rotation pulse (step 4 in the protocol, Fig. 5.2). One can smoothly transition between coherent states ($\xi = 0$) and cat states ($\xi = \pi/2$). Results for $|\uparrow\rangle$ (top row) and $|\downarrow\rangle$ (bottom row). Here $\alpha = 1.4$, $\theta = 0$ and $\phi = \pi$. (from [137])

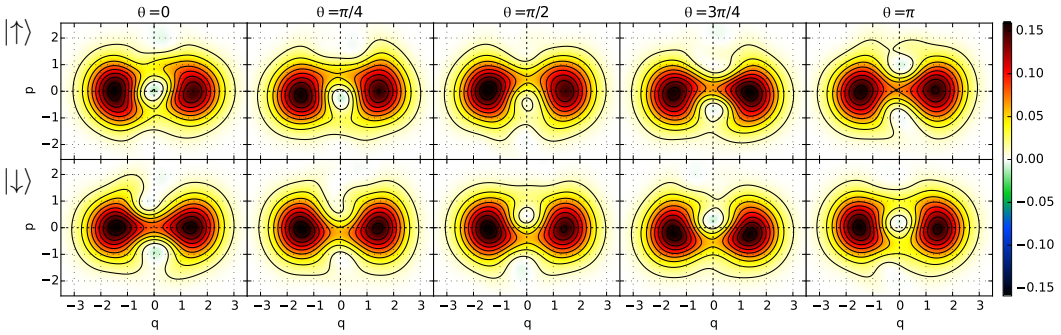

Figure 5.28.: Varying superposition phase θ. A continuous transition from an odd into an even cat state (upper row, for the atom in $|\uparrow\rangle$) and vice versa (lower row, for the atom in $|\downarrow\rangle$) is observable. The generated cat states have the form $(|\alpha\rangle \mp e^{i\theta}|-\alpha\rangle)/N$ with $\alpha = 1.4$. (from [137])

Specifically, the angle of the last spin rotation (step 4 in Fig. 5.2) controls the relative probabilities of the two coherent state contributions in the generated cat state. Scanning the Raman-pulse area ξ from 0 to $\pi/2$ continuously transforms the optical state (after measuring the atom) from a coherent state into a cat state with equal amplitudes of coherent contributions (Fig. 5.27).

The cat state in Equation (5.83) can be continuously tuned from an even cat state into an odd cat state via a change of the phase θ of the final $\pi/2$ rotation (step 4 in Fig. 5.2). This phase is imprinted onto the observed interference fringes in the Wigner function. Figure 5.28 shows the continuous transition from an even into an odd cat state and vice versa for $0 \leq \theta \leq \pi$. For instance at $\theta = \pi/2$, cats with imaginary superposition phases are created, sometimes called Yurke-Stoler states [147].

The optical phase ϕ is varied between 0 and 2π via a detuning between the impinging light and the cavity resonance. On resonance, $\phi = \pi$. Coherent state mixtures for various cavity detunings and values of ϕ are shown in Fig. 5.29. Here, the atomic state was not selected for $|\uparrow\rangle$ and $|\downarrow\rangle$ and the amplitude α was increased to better discriminate the two coherent peaks. Measured optical phase shifts $\phi(\Delta)$ are compared to the theory in Fig. 2.5.

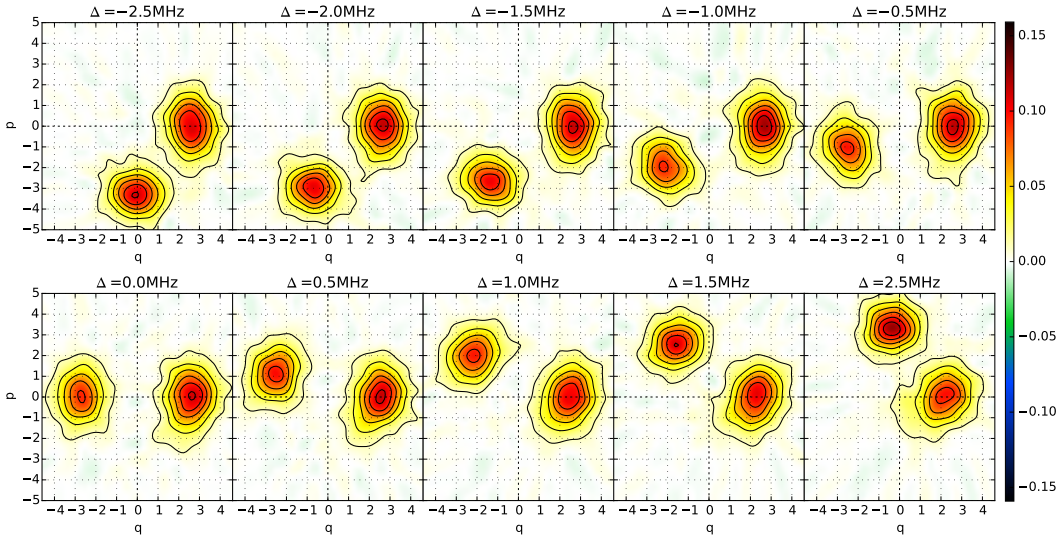

Figure 5.29.: Varying optical phase shift ϕ with cavity-light detuning Δ. Wigner functions of reflected coherent pulses of $\alpha = 2.3$ with the atom prepared in $(|\uparrow\rangle + |\downarrow\rangle)/\sqrt{2}$ and no consideration of the final atomic state. The detuning Δ between the impinging light and the cavity is scanned between ± 2.5 MHz in steps of 0.5 MHz. The Gaussian on the positive q axis corresponds to $|\alpha\rangle$ with the coupling atom $|\uparrow\rangle$, while the other Gaussian $|e^{i\phi}\alpha\rangle$, corresponding to $|\downarrow\rangle$, moves in phase space as Δ is changed. Because α is relatively large and the final atomic state is not considered, no interference fringes appear. The Wigner functions in this figure were reconstructed with the FBP, because it is better suited for states with large amplitudes than the ML technique. (from [137])

5.10.3. Quantum Gate between an Atom and a Cat State

The reflection mechanism (Eq. (5.17)) that has so far been used to produce cat states, is essentially a quantum-logic gate between an atom and the light field. Here, the coherent states $|\alpha\rangle$ and $|-\alpha\rangle$ form an orthogonal qubit basis (Fig. 2.1(c)) as long as α is reasonably large. For $\alpha = 1.4$, the overlap of these basis states is $|\langle -\alpha|\alpha\rangle|^2 = \exp(-4|\alpha|^2) = 3.9 \cdot 10^{-4}$, small enough for a good qubit. To probe the mechanism as a gate, we employ a basis set of input states $|\uparrow, \alpha\rangle, |\uparrow, -\alpha\rangle, |\downarrow, \alpha\rangle, |\downarrow, -\alpha\rangle$. In this basis, the gate acts as a CNOT with truth table

$$\begin{aligned} |\uparrow, +\alpha\rangle &\rightarrow |\uparrow, +\alpha\rangle \\ |\uparrow, -\alpha\rangle &\rightarrow |\uparrow, -\alpha\rangle \\ |\downarrow, +\alpha\rangle &\rightarrow |\downarrow, -\alpha\rangle \\ |\downarrow, -\alpha\rangle &\rightarrow |\downarrow, +\alpha\rangle \ . \end{aligned} \tag{5.84}$$

Here the atom serves as the control qubit that can flip the optical target qubit. This gate is characterized with coherent pulses of $\alpha = 1.4$, the same value for which entanglement will be shown between the atom and the light field in Sec. 5.10.4 to prove the quantum nature of the gate. The classical truth table is shown in Fig. 5.30 and exhibits the expected CNOT behavior. Optical losses change the input states $|\pm\alpha\rangle$ to output states $|\pm\alpha_{\mathrm{det}}\rangle$ with $\alpha_{\mathrm{det}} = \alpha\sqrt{1 - L_{\mathrm{det}}} = 1.0$. This change is well-characterized and therefore predictable, and the overlap between the two output states is still small $(1.8 \cdot 10^{-2})$. For the mean fidelity of the observed output states with the expected output states, values around 86% are found (Fig. 5.30(a)). The reduction from 100% comes mainly from phase noise due to cavity and laser frequency fluctuations that broaden the coherent-state Wigner function of the reflected field in the azimuthal direction (Sec. 5.9.5). If we discriminate the coherent-state

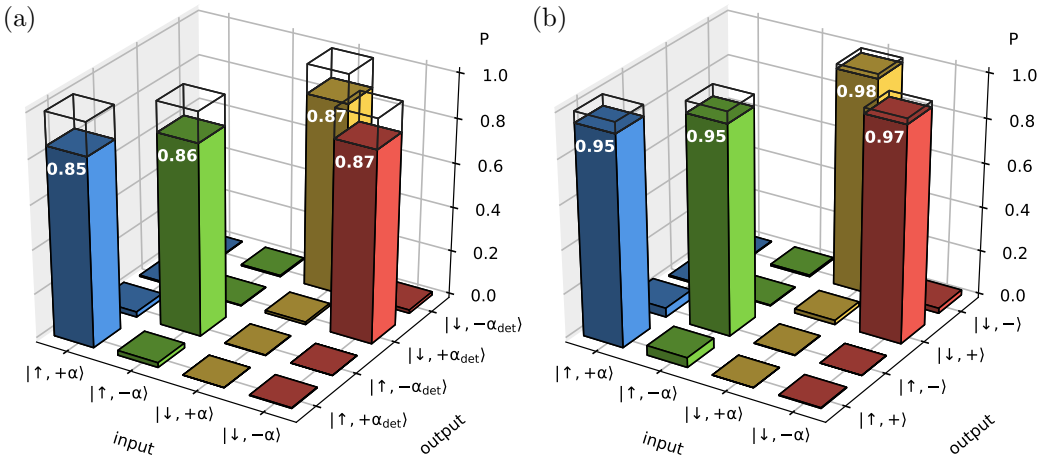

Figure 5.30.: Truth table of the atom-cat gate. For the choice of basis states $|\uparrow\rangle/|\downarrow\rangle \otimes |\alpha\rangle/|-\alpha\rangle$, the gate operates as a CNOT where the atom controls the optical target qubit. With the atom in $|\uparrow\rangle$, the optical state is unaffected (bars on the diagonal), whereas the atom in $|\downarrow\rangle$ causes the coherent state to flip phase (off-diagonal bars) as predicted by Eq. (5.17). The open bars show an ideal CNOT. The optical input states were coherent with $\alpha = \pm 1.4$. (a) shows overlaps of the reconstructed output states with the expected ideal output states with $\alpha_{\mathrm{det}} = 1.0$. The bars in each row do not need to sum up to 1, because the two states α_{det} and $-\alpha_{\mathrm{det}}$ only cover a fraction of the whole phase space and the measured state may lie outside. Infidelities are mainly due to broadened phase space distributions. In (b) the optical output is discriminated between $q > 0$ and $q < 0$. Here the overall phase flip – unrestricted to certain coherent modes – achieves a large fidelity of 96%. (from [137])

qubits simply between negative and positive q-quadratures (Fig. 5.30(b)), the fidelity of the truth table becomes 96%.

Note that the gate acts as a CPHASE in the $|\uparrow\rangle/|\downarrow\rangle \otimes |\mathrm{cat}_{\mathrm{even/odd}}\rangle$ basis:

$$\begin{aligned} |\uparrow, \mathrm{cat}_{\mathrm{even}}\rangle &\rightarrow +|\uparrow, \mathrm{cat}_{\mathrm{even}}\rangle \\ |\uparrow, \mathrm{cat}_{\mathrm{odd}}\rangle &\rightarrow +|\uparrow, \mathrm{cat}_{\mathrm{odd}}\rangle \\ |\downarrow, \mathrm{cat}_{\mathrm{even}}\rangle &\rightarrow +|\downarrow, \mathrm{cat}_{\mathrm{even}}\rangle \\ |\downarrow, \mathrm{cat}_{\mathrm{odd}}\rangle &\rightarrow -|\downarrow, \mathrm{cat}_{\mathrm{odd}}\rangle \ . \end{aligned} \tag{5.85}$$

The atom-cat gate is fundamentally different from a previous atom-photon gate Eq. (2.39) realized in the same setup [70] that was employed in Ch. 4. Here, the photonic qubit was encoded in the coherent phase, whereas in [70] it is encoded in the polarization. The two encodings are not trivially interconvertible.

5.10.4. Entanglement between the Atom and the Optical Field

An incoming coherent pulse that is reflected from the cavity creates an entangled state between the atom and the light field (Eq. (5.18))

$$|\psi_{ac}\rangle = \frac{1}{\sqrt{2}} \left(|\uparrow\rangle|\alpha\rangle + |\downarrow\rangle|-\alpha\rangle \right) \ , \tag{5.86}$$

the Schrödinger-cat state. This is a maximally entangled state for $\alpha \gg 1$, when the overlap $|\langle -\alpha|\alpha\rangle|^2$ is vanishing and the photonic state encodes a qubit. In the previously presented results, the optical state is conditioned on the measurement outcome of the atom, which is recorded a few microseconds after the homodyne measurement. In that case, the state of the

optical field is a cat state. However, up until the measurement of any of the two systems, they are in an entangled state [5], that is, a state in which the properties of the two systems, atom and light field, cannot be described independently.

The experiment creates the state of Eq. (5.86) with some imperfections, which is fully described by the atom-light density matrix ρ_{ac}. This density matrix allows predictions about both subsystems in any measurement basis, as well as the determination of properties of the combined system, in particular the amount of entanglement.

The determination of ρ_{ac} requires tomography [50] that combines measurements in different bases. In this particular case of a discrete-continuous hybrid state, the representation with so-called joint Wigner functions, pioneered recently in [156], is well suited (but other representations [172, 173] are available as well). Here, the atomic qubit is written in terms of the well-known Pauli matrices $\sigma_i \in \{\sigma_I, \sigma_x, \sigma_y, \sigma_z\}$. The combined state is then expressed as $\rho_{ac} = \frac{1}{2}\sum_i \sigma_i \otimes W_i$, where $W_i \in \{W_I, W_x, W_y, W_z\}$ are the joint Wigner functions. In case of a one-qubit tomography, W_i would be the Stokes parameters [50]. In this experiment, however, each W_i has the shape of a (non-normalized) Wigner function instead of a scalar. W_I is the average photonic density matrix with the atomic state traced out, that is in this case an incoherent mixture of two coherent states. $W_{x,y,z}$ are sums of photonic density matrices weighted with the outcome of the atomic spin measurement of ± 1 for outcomes $|\uparrow\rangle$ and $|\downarrow\rangle$, respectively, in the measurement bases x, y and z. In the ideal case, that is

$$W_I = \tfrac{1}{2}|\alpha\rangle\langle\alpha| + \tfrac{1}{2}|-\alpha\rangle\langle-\alpha| \tag{5.87}$$

$$W_x = P(|\uparrow_x\rangle)\rho_{\text{even cat}} - P(|\downarrow_x\rangle)\rho_{\text{odd cat}} \tag{5.88}$$

$$W_y = \tfrac{1}{2}\rho_{i\text{ cat}} - \tfrac{1}{2}\rho_{-i\text{ cat}} \tag{5.89}$$

$$W_z = \tfrac{1}{2}|\alpha\rangle\langle\alpha| - \tfrac{1}{2}|-\alpha\rangle\langle-\alpha| \tag{5.90}$$

where $P(|\uparrow_x\rangle)$ and $P(|\downarrow_x\rangle)$ deviate from 1/2 when α is small (Eq. (5.24)). The Wigner functions of measured even and odd cat states for W_x are shown in Fig. 5.15, the "Yurke-Stoler" i and $-i$ cat states [147] for W_y are those depicted in Fig. 5.28 for $\theta = \pi/2$ and the coherent states for W_z are obtained when the atom is measured in the z-basis without rotation ($\xi = 0$ in Fig. 5.27).

The resulting joint Wigner functions are presented in Fig. 5.31. Here, W_I and W_z are not affected by loss-induced decoherence and exhibit near-ideal peak amplitudes of $\pm 1/(2\pi) \approx \pm 0.16$. In W_x and W_y the coherent peaks cancel and only the central coherence fringes remain, thus offering a very clear view of the fringe structure. The visible fringe amplitude is significantly reduced from the ideal value of $1/\pi$ due to losses by the damping factor $\exp(-2L\alpha^2)$, as predicted in Sec. 5.4.1. The elements of ρ_{ac} in the Fock basis up to $n = 3$ are

	$\langle\uparrow\|\langle 0\|$	$\langle\uparrow\|\langle 1\|$	$\langle\uparrow\|\langle 2\|$	$\langle\uparrow\|\langle 3\|$	$\langle\downarrow\|\langle 0\|$	$\langle\downarrow\|\langle 1\|$	$\langle\downarrow\|\langle 2\|$	$\langle\downarrow\|\langle 3\|$
$\|\uparrow\rangle\|0\rangle$	0.183	0.183	0.133	0.070	0.017	−0.014	0.015	−0.009
$\|\uparrow\rangle\|1\rangle$	$-0.004i$	0.205	0.135	0.076	0.021	−0.035	0.016	−0.016
$\|\uparrow\rangle\|2\rangle$	$0.002i$	$0.001i$	0.103	0.052	0.017	−0.011	0.015	−0.006
$\|\uparrow\rangle\|3\rangle$	$0.002i$	$0.000i$	$0.001i$	0.029	0.010	−0.015	0.008	−0.006
$\|\downarrow\rangle\|0\rangle$	$0.002i$	$-0.005i$	$0.001i$	$-0.004i$	0.151	−0.162	0.119	−0.069
$\|\downarrow\rangle\|1\rangle$	$0.000i$	$0.003i$	$0.000i$	$0.005i$	$-0.001i$	0.182	−0.129	0.078
$\|\downarrow\rangle\|2\rangle$	$0.003i$	$0.000i$	$0.002i$	$0.000i$	$0.004i$	$-0.003i$	0.096	−0.055
$\|\downarrow\rangle\|3\rangle$	$0.001i$	$-0.003i$	$0.001i$	$0.001i$	$-0.003i$	$0.004i$	$0.000i$	0.034

(5.91)

where the upper diagonal shows only the real parts and the lower diagonal only the imaginary parts for compactness. Of course, ρ_{ac} is Hermitian, that is $\rho_{ac} = \rho_{ac}^\dagger$.

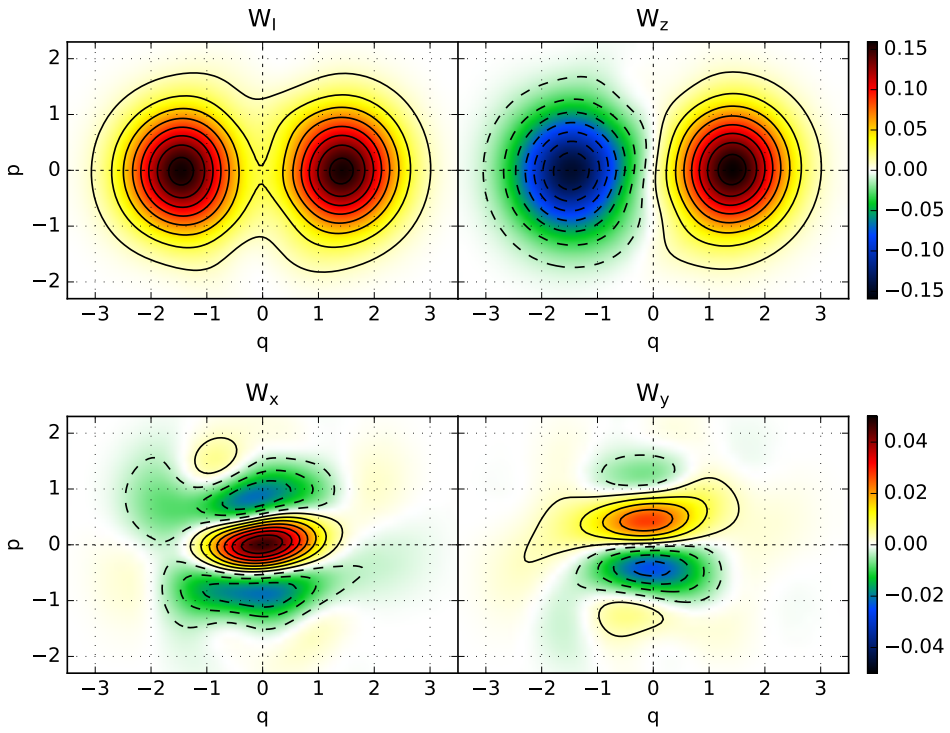

Figure 5.31.: Joint Wigner functions W_I, W_z, W_x and W_y of an experimentally prepared entangled atom-light Schrödinger-cat state of $\alpha = 1.4$. Each of the underlying Wigner functions was reconstructed from around $2 \cdot 10^4$ quadrature measurements. No loss-correction was applied. The noise level can be estimated from the light yellow and green structures in W_x and W_y apart from the center. Together, the joint Wigner functions fully represent ρ_{ac}. (from [137])

The amount of entanglement is quantified by an entanglement measure that is computable and able to handle mixed states of systems larger than qubits, such as the so-called "negativity" [130]. Other than in previous sections, negativity does not refer to values of the Wigner function here, but instead to eigenvalues of a matrix. The negativity is defined as

$$\mathcal{N}(\rho) = \frac{||\rho^{T_A}||_1 - 1}{2} \tag{5.92}$$

where ρ^{T_a} is the partial transpose with respect to one of the two subsystems, spin or light field, and $||A||_1$ is the "trace norm" of A, which is equal to the sum of the absolute values of the eigenvalues of A. Hence, $\mathcal{N}$ equals the absolute sum of all negative eigenvalues of ρ^{T_a}. The negativity is zero for any separable state and reaches values up to $1/2$ for maximally entangled states.

Applying the definition to the reconstructed state gives

$$\mathcal{N}(\rho_{ac}) = 0.057 \pm 0.005 \; . \tag{5.93}$$

The negativity results mostly from one eigenvalue $\lambda_{\min} = -0.055$, while the second smallest eigenvalue is only -0.001. The standard error is determined through a Monte-Carlo simulation, which samples random measurement data according to the reconstructed ρ_{ac} and applies the same reconstruction to each of these data sets. The standard deviation of the negativities from sampled data sets is an estimator for the statistical standard deviation in $\mathcal{N}$. With a significance of around 11 standard deviations, the atom-light entanglement is very certain.

The atomic qubit could also be mapped to the polarization of a single photon through the readout process reported in [126]. This would extend the atom-light entanglement towards purely optical photon-light entanglement [217], a hybrid entanglement between discrete and continuous-variables states of light.

5.10.5. Cat States for Bell Tests

Entangled states, such as the Schrödinger-cat state produce measurement outcomes that cannot be fully explained by any *local realistic* theory, that is a theory that assumes physical objects exist independently of an observer and cannot share information faster than the speed of light. That quantum mechanics allows for entanglement, in which two physical properties may not both have a defined "realistic" value, was first pointed out by Einstein, Podolski and Rosen [6] in 1935, the very same year that Erwin Schrödinger came up with his famous cat gedankenexperiment. Later, in 1964, John Bell proved that no local realistic theory can ever explain the predictions of quantum mechanics [218].

An entangled state in the laboratory can be employed to test the hypothesis that the universe is indeed not local realistic, but rather follows the laws of quantum mechanics. Starting in 1972 [219], many such "Bell test" experiments have been performed, all in agreement with quantum mechanics. Later implementations have focused on the elimination of so-called loopholes [220], imperfections in the experiment that would make the measured data agree with quantum mechanics even if the universe was local realistic. Most notable and experimentally addressable are the following three:

- The fair sampling (detection) loophole opens if some of the states are lost before they get measured. Then, the ensemble of recorded states may contradict local realism, whereas the complete sample would not.
- The locality loophole opens when the two systems are not space-like separated, that is, separated far enough that a (hypothetical) signal could be exchanged below the speed of light within the time frame of each measurement.
- The memory loophole is the possibility that subsequent measurements are not independent, as assumed, but rather that earlier measurements influence the following ones.

Optical Schrödinger-cat states are natural candidates for a Bell test, because they allow to close these loopholes. The fair sampling loophole requires high detection efficiency on both parts of the entangled state. This is already the case for the atom, where the state is long-lived (usually limited by the coherence time) and the state detection gives a definite result in each attempt. The photonic part can be measured with homodyne detectors, which have reached efficiencies far beyond 90%, rivaled by single-photon detectors (based on superconducting nanowires) only recently. A challenge is propagation loss in long optical fibers, which has the same effect as detector inefficiency.

Closure of the locality loophole requires some distance between the atom and the optical state during the time of measurement. At measurement timescales of microseconds, the required distance amounts to several hundred meters. While the atom cannot propagate fast in this experiment, the optical state naturally does. It can be sent to a distant laboratory through a fiber or free space and be detected there.

There is a variety of ways to perform Bell tests with cat states because of the free choice of dichotomic measurement bases for continuous-variable states. For hybrid entangled atom-cat states, there are proposals for photon-counting measurements [221] as well as mixed photon-counting and homodyning schemes [222, 223]. In a circuit QED system, such a Bell

test was recently realized [156], although without closing the locality loophole. A second type of Bell test uses pure cat states which are disentangled from the atom. When divided on a beam splitter, they turn into a two-mode entangled state of the type $(|\alpha\rangle|\alpha\rangle \pm |-\alpha\rangle|-\alpha\rangle)/N$ (similar to Sec. 5.6.9). Bell tests on such entangled states were considered for symmetric [224] and asymmetric coherent amplitudes [225]. All of those schemes have the benefit of being quite resilient to losses, which makes a future implementation of an optical cat-state based Bell test in existing cavity setups a realistic option.

5.11. Conclusion

The experiment has demonstrated unprecedented control over all relevant parameters of optical cat states, making them a resource for continuous-variable quantum information processing with coherent-state superpositions as qubits [179, 180]. The useful size of these qubits depends on the optical losses, elimination of which is the key challenge for future improvements. Optical losses in the cavity (Sec. 5.7) can be reduced with improved cavity parameters. For example, parasitic losses $\kappa - \kappa_r$ could be lowered by reducing mirror surface scattering and absorption. Likewise, the atom-cavity coupling rate g could be increased through a smaller mode volume, either by reducing the mirror distance or by decreasing the mirror radius of curvature. Here, microscopic fiber cavities [226] offer improvements by more than an order of magnitude. Propagation losses can be mitigated by loss-correction codes that are specifically available for cat states [187]. Optical cat states as qubits could therefore be a promising alternative to single photons for quantum communication in a future quantum internet [10, 36, 37], at least when losses are not too severe. In contrast to all protocols so far realized with single optical photons as qubits [35] and with entangled Schrödinger-cat states [171–176], the creation and detection of Schrödinger-cat states as implemented here prepares and verifies an entangled light-matter state in each trial, without any postselection, making it deterministic in theory and in practice.

6. Summary and Outlook

In this work, two novel photonic quantum-information-processing experiments were performed, both based on a single atom trapped in a high-finesse optical cavity. The strong coupling between the atom and the light field provided by the cavity enables the deterministic manipulation of light on the single-photon level, which is otherwise very difficult to achieve.

The first experiment was the implementation of a universal quantum logic gate between two photons [96, 227]. In that experiment, two independent photons, each carrying a polarization qubit, are brought to a mutual interaction, in which each photon can completely change the other one's output state. The gate accepts any combination of input polarization states and is able to entangle the two photons. The gate was shown to produce significantly entangled states, which cannot be achieved by any classical (non-quantum) device. The type of operation, a controlled-NOT, in combination with arbitrary single qubit rotations, performed by optical wave plates, is universal in the sense that it can in principle be used to assemble any possible quantum circuit without requiring additional types of gates.

The decisive novelty of the two-photon gate compared to previous implementations is the deterministic nature of its protocol. While implementations based on linear optics use intrinsically probabilistic single-photon measurements to create an interaction, the protocol used in this work [72] can perform a successful gate operation in each trial. This is crucial for future applications, when large numbers of gates are cascaded and each one relies on the success of the previous one. In the presented experiment, technical losses do still limit the success rate to around 4%, already decent in comparison with existing gates, but still subject to significant improvements in future implementations. The protocol has the appealing property that both photons stay in temporally well-separated independent modes. Therefore photons may have different and to some extent arbitrary temporal shapes, the gate is resilient to timing jitter of the input and does not require interferometric stability. Unlike in some other protocols where the photons are temporarily converted (e.g. to spin waves in atomic vapor) in order to interact, in this implementation the photons always stay photons during the whole gate execution.

The second experiment demonstrates the creation of optical Schrödinger-cat states [137, 228, 229], states of light with two opposite oscillation amplitudes at the same time. Named after Erwin Schrödinger's famous fictitious cat (Fig. 6.1), such states explore coherent quantum superpositions of two macroscopically distinct states. Cat states that are superpositions of coherent states have been realized in several different systems, starting in the mid-1990s. After several deterministic implementations in the microwave domain, and many probabilistic implementations in the optical domain, this experiment has shown the first deterministic implementation in the optical domain, following a proposal from 2005 [189]. In each trial that the experiment is executed, the atom gets entangled to a coherent state of light. Such an entangled state is what Schrödinger had in mind, when he imagined coupling a cat to a radioactive atom. In the entangled state the cat is both dead and alive, while the total state of the system is still pure, and not a random mixture. The present experiment has gone one step further. As the spin state of the atom is coherently controlled and may be measured in an arbitrary basis, the optical "cat" can be projected into a superposition state on its own, that continues to exist independently of the atom. The large degree of control

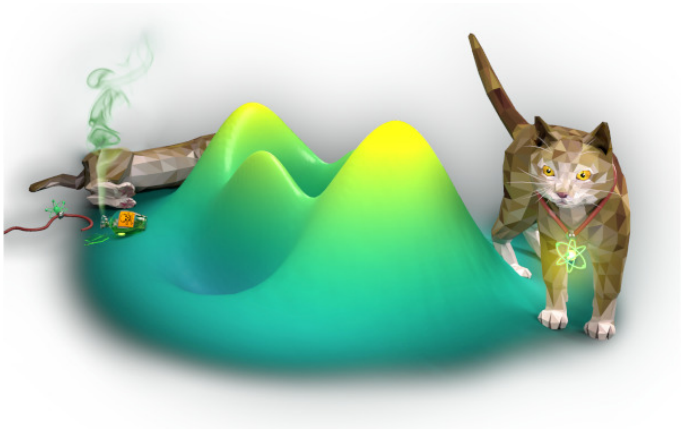

Figure 6.1.: Schrödinger's cat and its optical representation. Courtesy of C. Hohmann, Nanosystems Initiative Munich (NIM)

also has enabled the production of a plethora of different cat states and the control over all their degrees of freedom. Tomographic methods have allowed for the reconstruction of the optical states as well as the total entangled atom-cat state in full detail. An analytic description of the states was derived, from which a number of properties were predicted, to which the experimental data show remarkable agreement. It was discovered that optical losses in the cavity, which pose the most fundamental limitation to the cat state size, contribute only partially to the decoherence. This has allowed for the measurement of much more pronounced cat states than one could initially have hoped for. All in all the theoretical proposal was unequivocally confirmed and the experiment lays groundwork for cavity-based continuous-variable experiments.

The two experiments highlight two aspects of light, which both follow from the quantum-mechanical description: The particle- and the wave-nature. The two-photon gate relies on the use of distinct single photons. Their existence in each mode is verified by a single-photon detector. Any additional photon in the optical pulse would immediately revert the action of the gate by flipping the decisive superposition phase back to its original value. If on the other hand a photon gets absorbed, its information is irreversibly lost and the quantum computation ends without result. Heralded single-photon experiments can trade a limited success probability (efficiency) for an enhanced fidelity. In contrast, continuous-variable wave experiments like the creation of cat states can always (deterministically) succeed, both in the protocol and in practice, but at the price of increased loss sensitivity. States are immediately affected by losses and the fidelity decreases gradually. Cat states are prime examples of continuous-variable states. They consist of coherent waves, most equivalent to classical electromagnetic waves, and have a continuously tunable amplitude, which is recorded in the detection setup. Optical phase shifts, produced by the cavity can be directly observed as a phase in phase space. The combination of particle and wave experiments shows the full picture and provides a very broad and vivid understanding of the system.

The requirement for both experiments was a single quantum emitter that is strongly coupled to the light field. In the specific setting of a single-sided cavity the key parameters are single-sidedness $\eta_\mathrm{r} = \kappa_r/\kappa$ and cooperativity C. The photon-photon gate requires an optical phase flip on resonance when the emitter is coupled, given when $1/2 < \eta_\mathrm{r} < C + 1/2$. The creation of cat states requires low losses, achieved when $\eta_\mathrm{r} C/(C + 1/2)$ is close to 1. These conditions are fulfilled in the experiment by the use of low-loss cavity mirrors and an atom that is continuously trapped inside the cavity mode with a small mode volume. A second requirement was the active control of the atomic spin state to create arbitrary

superposition states, provided by a Raman laser pair. To obtain reproducible results of good quality, several automatic stabilizations had to be implemented: A temperature stabilization of the optical setup for stable beam pointings and optical mode coupling, optical power stabilizations of all relevant laser beams and a stabilization of the differential cavity drift between the locking laser and the signal laser. Other experimental parameters were manually stabilized, such as fiber polarization drifts, drifts of the local magnetic field and drifts of the effective optical trap depth at the position of the atom.

Significant improvements in future experiments require cavities with higher cooperativities, achievable with even smaller mode volumes. However, several enhancements are possible without changing the core of the setup. First, the optical mode matching, which has been limited to around 92% so far, can be increased substantially using additional optics. Losses at the cavity input due to an asymmetric beam splitter, which were not relevant in this work, but may become so in future experiments, can be avoided by the use of an optical circulator that routes cavity input and output to distinguishable modes. Current off-the-shelf fiber-based circulators for 780 nm are available with 83% transmission and likely to improve. Further technical improvements are possible in the stability of the cavity lock, by using a new generation of narrow-line lasers and digital locking electronics with a tailored response to the cavity transfer function. The single-photon detection efficiencies can be improved from 50% with current avalanche photodiodes to above 90% using superconducting nanowire single-photon detectors.

The proof-of-principle implementations of a two-photon gate and the creation of cat states lay groundwork for a wide range of optical quantum information processing experiments, in particular in the context of quantum networks. The photonic states readily exist inside well-defined optical modes that can be connected to additional nearby and distant quantum network nodes [34]. The presented universal quantum gate can act as a central processing unit of a distributed quantum computer, where pairs of photons are sequentially routed to and processed. In principle, one processing unit is already enough, but the challenge lies in the large fidelities and efficiencies required to scale up the system. Therefore, intermediate applications are protocols with a smaller number of processing steps, such as a quantum repeater station [134] for optical quantum key distribution [9].

Transmission of light through fibers and other components is always lossy, so one of the key techniques will be loss-correction codes. One such code, based on multi-component cat states [183, 184], would be a promising next step of the continuous-variable experiment. A cat-code with four coherent components can be generated by two subsequent cavity reflections, either from two different cavities or from the same cavity with atomic state detection and preparation between the reflections. Another possible scheme is to reflect subsequent light pulses from one cavity and thereby create two spatially separated cat states entangled to each other [189]. Finally, discrete (single photon) and continuous-variable states may also be combined in one experiment. In that sense, hybrid experiments may be performed, that utilize the best of both worlds [217].

The protocols and experiments explored in this work are not limited to single atoms in macroscopic cavities. Although this setting provides a very pure and ideal physical system, the experimental requirements of an ultra-high vacuum, narrow-line lasers and high-precision optics are rather challenging. There is a range of platforms which may implement the same physics [35]. This includes resonators between optical fibers [226, 230], inside optical fibers, tapered fibers, bottle- [116] and microsphere resonators [231], photonic crystals as well as microresonators in solid state systems [52, 66, 232]. Emitters may be isolated atoms or ions [233] as well as various types of artificial atoms, such as quantum dots [66], crystal defects, embedded rare-earth atoms or mesoscopic superconducting devices [40]. Each of these systems faces its own challenges, such as required cryogenic temperatures, short coherence

times or limited long-term stability. However, with the tremendous amount of research effort presently invested, there is a good chance that the protocols pioneered in this work may be implemented with very high fidelity in an economically scalable fashion.

Optical cavities provide the crucial interface between light and matter for a photonic quantum-network node. They have now proven the functionality to store photons, emit photons and also to process photons in a highly coherent fashion. These processes are indispensible for full-fledged quantum networks. The next few years are expected to bring a number of novel quantum network applications, such as quantum error correction, distributed quantum computing and a quantum repeater for long distance quantum communication. These are exciting times for quantum information science.

A. Full Experimental Setup

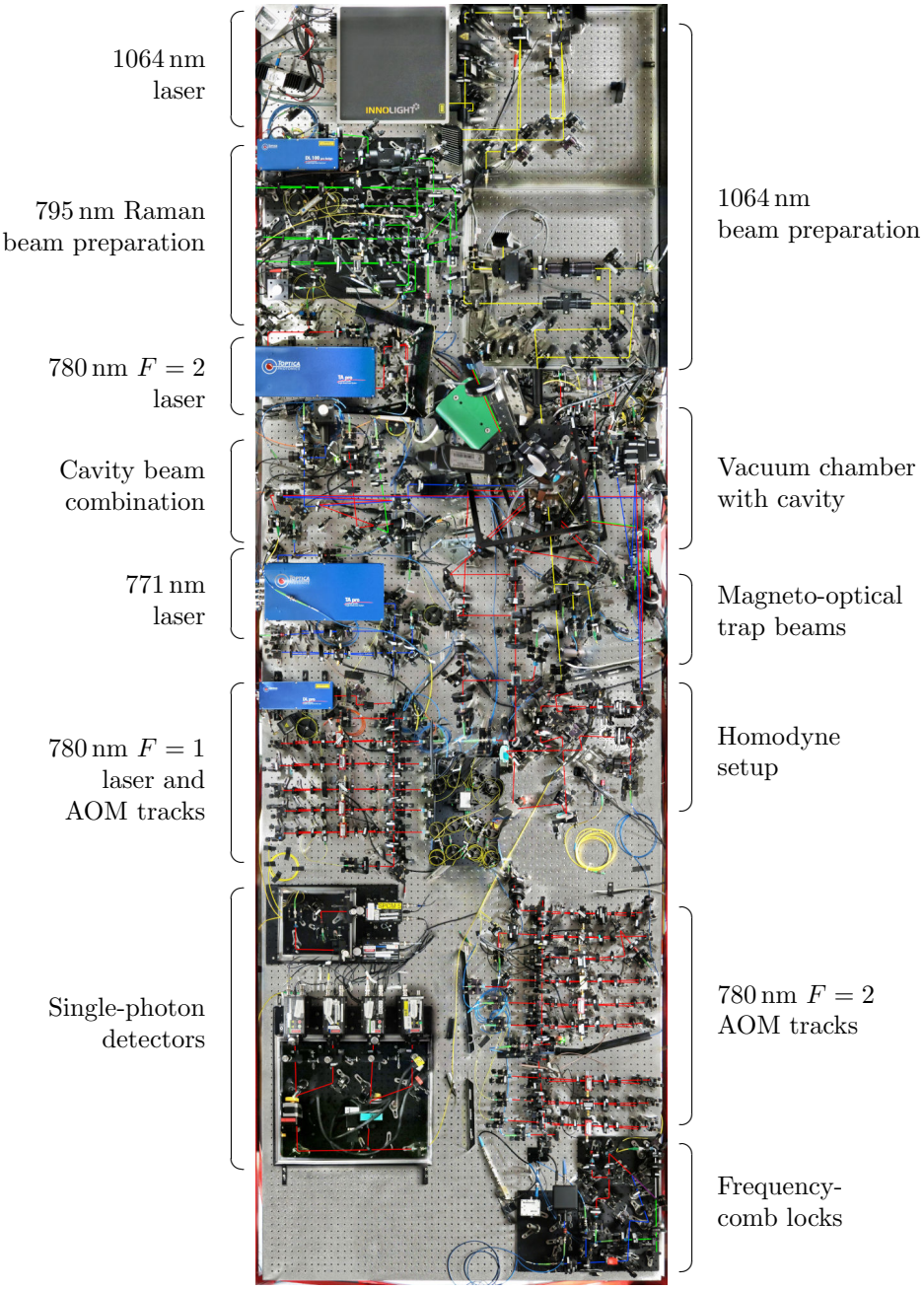

Figure A.1.: Stitched photograph of the complete optical setup of the Qgate experiment. Laser beams of different wavelengths are drawn in different colors: 771 nm (blue), 780 nm (red), 795 nm (green) and 1064 nm (yellow). The setup measures 1.5 m × 4.8 m with mounting holes every 2.54 cm.

B. Glossary

AOD acousto-optic deflector

AOM acousto-optic modulator

CNOT controlled-NOT

CPHASE controlled-phase

EOM electro-optic modulator

EP entanglement potential

FBP filtered back projection

FPGA field-programmable gate array

FWHM full width at half maximum

LO local oscillator

LOQC linear optics quantum computing

ML maximum likelihood

MOT magneto-optical trap

NPBS non-polarizing beam splitter

OHT optical homodyne tomography

PM polarization-maintaining

QED quantum electrodynamics

RMS root mean square

SPD single-photon detector

Bibliography

[1] J. C. Maxwell. "VIII. A dynamical theory of the electromagnetic field". *Philosophical Transactions of the Royal Society of London* **155**, 459 (1865).

[2] G. R. Fowles. *Introduction to modern optics*. 2. ed., repr. Dover Publications, 1989. ISBN: 978-0-486-65957-2.

[3] A. Einstein. "Über einen die Erzeugung und Verwandlung des Lichtes betreffenden heuristischen Gesichtspunkt". *Annalen der Physik* **322**, 132 (1905).

[4] H. Paul. *Introduction to quantum optics: from light quanta to quantum teleportation*. Cambridge University Press, 2004. ISBN: 978-0-521-83563-3.

[5] R. Horodecki, P. Horodecki, M. Horodecki, and K. Horodecki. "Quantum entanglement". *Reviews of Modern Physics* **81**, 865 (2009).

[6] A. Einstein, B. Podolsky, and N. Rosen. "Can Quantum-Mechanical Description of Physical Reality Be Considered Complete?" *Physical Review* **47**, 777 (1935).

[7] M. D. Reid, P. D. Drummond, W. P. Bowen, E. G. Cavalcanti, et al. "*Colloquium*: The Einstein-Podolsky-Rosen paradox: From concepts to applications". *Reviews of Modern Physics* **81**, 1727 (2009).

[8] R. P. Feynman. "Simulating Physics with Computers". *International Journal of Theoretical Physics* **21**, 467 (1982).

[9] N. Gisin, G. Ribordy, W. Tittel, and H. Zbinden. "Quantum cryptography". *Reviews of Modern Physics* **74**, 145 (2002).

[10] M. A. Nielsen and I. L. Chuang. *Quantum Computation and Quantum Information*. Cambridge University Press, 2000. ISBN: 978-0-521-63503-5.

[11] E. Schrödinger. "Are there quantum jumps?" *The British Journal for the Philosophy of Science* **III**, 233 (1952).

[12] W. Neuhauser, M. Hohenstatt, P. E. Toschek, and H. Dehmelt. "Localized visible Ba^+ mono-ion oscillator". *Physical Review A* **22**, 1137 (1980).

[13] J. I. Cirac and P. Zoller. "Quantum Computations with Cold Trapped Ions". *Physical Review Letters* **74**, 4091 (1995).

[14] K. Mølmer and A. Sørensen. "Multiparticle Entanglement of Hot Trapped Ions". *Physical Review Letters* **82**, 1835 (1999).

[15] H. Haffner, C. Roos, and R. Blatt. "Quantum computing with trapped ions". *Physics Reports* **469**, 155 (2008).

[16] A. L. Migdall, J. V. Prodan, W. D. Phillips, T. H. Bergeman, and H. J. Metcalf. "First Observation of Magnetically Trapped Neutral Atoms". *Physical Review Letters* **54**, 2596 (1985).

[17] S. Chu. "Nobel Lecture: The manipulation of neutral particles". *Reviews of Modern Physics* **70**, 685 (1998).

[18] C. N. Cohen-Tannoudji. "Nobel Lecture: Manipulating atoms with photons". *Reviews of Modern Physics* **70**, 707 (1998).

[19] W. D. Phillips. "Nobel Lecture: Laser cooling and trapping of neutral atoms". *Reviews of Modern Physics* **70**, 721 (1998).

[20] N. Gisin and R. Thew. "Quantum communication". *Nature Photonics* **1**, 165 (2007).

[21] E. Knill, R. Laflamme, and G. J. Milburn. "A scheme for efficient quantum computation with linear optics". *Nature* **409**, 46 (2001).

[22] P. Kok, W. J. Munro, K. Nemoto, T. C. Ralph, J. P. Dowling, and G. J. Milburn. "Linear optical quantum computing with photonic qubits". *Reviews of Modern Physics* **79**, 135 (2007).

[23] J.-W. Pan, Z.-B. Chen, C.-Y. Lu, H. Weinfurter, A. Zeilinger, and M. Żukowski. "Multiphoton entanglement and interferometry". *Reviews of Modern Physics* **84**, 777 (2012).

[24] F. Flamini, N. Spagnolo, and F. Sciarrino. "Photonic quantum information processing: a review". *Reports on Progress in Physics* **82**, 016001 (2018).

[25] D. Meschede, H. Walther, and G. Müller. "One-Atom Maser". *Physical Review Letters* **54**, 551 (1985).

[26] G. Rempe, H. Walther, and N. Klein. "Observation of quantum collapse and revival in a one-atom maser". *Physical Review Letters* **58**, 353 (1987).

[27] S. Haroche. "Nobel Lecture: Controlling photons in a box and exploring the quantum to classical boundary". *Reviews of Modern Physics* **85**, 1083 (2013).

[28] G. Nogues, A. Rauschenbeutel, S. Osnaghi, M. Brune, J. M. Raimond, and S. Haroche. "Seeing a single photon without destroying it". *Nature* **400**, 239 (1999).

[29] G. Rempe, R. Lalezari, R. J. Thompson, and H. J. Kimble. "Measurement of ultralow losses in an optical interferometer". *Optics Letters* **17**, 363 (1992).

[30] J.-M. Raimond and G. Rempe. "Cavity Quantum Electrodynamics: Quantum Information Processing with Atoms and Photons". In: *Lectures on Quantum Information*. Ed. by D. Bruß and G. Leuchs. Wiley-VCH Verlag GmbH, 2006, pp. 537–554. ISBN: 978-3-527-40527-5.

[31] R. J. Thompson, G. Rempe, and H. J. Kimble. "Observation of normal-mode splitting for an atom in an optical cavity". *Physical Review Letters* **68**, 1132 (1992).

[32] P. Maunz, T. Puppe, I. Schuster, N. Syassen, P. W. H. Pinkse, and G. Rempe. "Normal-Mode Spectroscopy of a Single-Bound-Atom–Cavity System". *Physical Review Letters* **94**, 033002 (2005).

[33] G. Kurizki, P. Bertet, Y. Kubo, K. Mølmer, D. Petrosyan, P. Rabl, and J. Schmiedmayer. "Quantum technologies with hybrid systems". *Proceedings of the National Academy of Sciences* **112**, 3866 (2015).

[34] S. Ritter, C. Nölleke, C. Hahn, A. Reiserer, et al. "An elementary quantum network of single atoms in optical cavities". *Nature* **484**, 195 (2012).

[35] A. Reiserer and G. Rempe. "Cavity-based quantum networks with single atoms and optical photons". *Reviews of Modern Physics* **87**, 1379 (2015).

[36] H. J. Kimble. "The quantum internet". *Nature* **453**, 1023 (2008).

[37] S. Wehner, D. Elkouss, and R. Hanson. "Quantum internet: A vision for the road ahead". *Science* **362**, 1 (2018).

[38] H. Takahashi, E. Kassa, C. Christoforou, and M. Keller. "Cavity-induced anticorrelated photon-emission rates of a single ion". *Physical Review A* **96**, 023824 (2017).

[39] R. J. Schoelkopf and S. M. Girvin. "Wiring up quantum systems". *Nature* **451**, 664 (2008).

[40] A. Blais, R.-S. Huang, A. Wallraff, S. M. Girvin, and R. J. Schoelkopf. "Cavity quantum electrodynamics for superconducting electrical circuits: An architecture for quantum computation". *Physical Review A* **69**, 062320 (2004).

[41] C. Neill, P. Roushan, K. Kechedzhi, S. Boixo, et al. "A blueprint for demonstrating quantum supremacy with superconducting qubits". *Science* **360**, 195 (2018).

[42] J. P. Dowling and G. J. Milburn. "Quantum technology: the second quantum revolution". *Philosophical Transactions of the Royal Society of London. Series A: Mathematical, Physical and Engineering Sciences* **361**, 1655 (2003).

[43] J.-G. Ren, P. Xu, H.-L. Yong, L. Zhang, et al. "Ground-to-satellite quantum teleportation". *Nature* **549**, 70 (2017).

[44] J. L. O'Brien, A. Furusawa, and J. Vučković. "Photonic quantum technologies". *Nature Photonics* **3**, 687 (2009).

[45] I. A. Walmsley. "Quantum optics: Science and technology in a new light". *Science* **348**, 525 (2015).

[46] M. Riedel, M. Kovacs, P. Zoller, J. Mlynek, and T. Calarco. "Europe's Quantum Flagship initiative". *Quantum Science and Technology* **4**, 020501 (2019).

[47] F. Sun, "Topics in Quantum Networking". arXiv: 1903.02910 (2019).

[48] P. A. M. Dirac. "A new notation for quantum mechanics". *Mathematical Proceedings of the Cambridge Philosophical Society* **35**, 416 (1939).

[49] D. P. DiVincenzo. "The Physical Implementation of Quantum Computation". *Fortschritte der Physik* **48**, 771 (2000).

[50] J. Altepeter, E. Jeffrey, and P. Kwiat. "Photonic State Tomography". In: *Advances In Atomic, Molecular, and Optical Physics*. Vol. 52. Elsevier, 2005, pp. 105–159. ISBN: 978-0-12-003852-7.

[51] A. Predojević and M. W. Mitchell, eds. *Engineering the Atom-Photon Interaction*. Nano-Optics and Nanophotonics. Springer International Publishing, 2015. ISBN: 978-3-319-19230-7.

[52] D. E. Chang, V. Vuletić, and M. D. Lukin. "Quantum nonlinear optics — photon by photon". *Nature Photonics* **8**, 685 (2014).

[53] G. Leuchs and M. Sondermann. "Light–matter interaction in free space". *Journal of Modern Optics* **60**, 36 (2013).

[54] Y.-S. Chin, M. Steiner, and C. Kurtsiefer. "Nonlinear photon-atom coupling with 4Pi microscopy". *Nature Communications* **8**, 1200 (2017).

[55] R. Maiwald, A. Golla, M. Fischer, M. Bader, et al. "Collecting more than half the fluorescence photons from a single ion". *Physical Review A* **86**, 043431 (2012).

[56] K. Hammerer, A. S. Sørensen, and E. S. Polzik. "Quantum interface between light and atomic ensembles". *Reviews of Modern Physics* **82**, 1041 (2010).

[57] S. Haroche and J.-M. Raimond. *Exploring the quantum: atoms, cavities, and photons*. Oxford university press, 2006. ISBN: 978-0-19-850914-1.

[58] E. T. Jaynes and F. W. Cummings. "Comparison of quantum and semiclassical radiation theories with application to the beam maser". *Proceedings of the IEEE* **51**, 89 (1963).

[59] B. W. Shore and P. L. Knight. "The Jaynes-Cummings Model". *Journal of Modern Optics* **40**, 1195 (1993).

[60] H. J. Kimble. "Strong Interactions of Single Atoms and Photons in CavityQED". *Physica Scripta* **T76**, 127 (1998).

[61] C. W. Gardiner and M. J. Collett. "Input and output in damped quantum systems: Quantum stochastic differential equations and the master equation". *Physical Review A* **31**, 3761 (1985).

[62] D. F. Walls and G. J. Milburn. *Quantum optics*. Springer Science & Business Media, 2007. ISBN: 978-3-540-28573-1.

[63] A. Kuhn. "Cavity Induced Interfacing of Atoms and Light". In: *Engineering the Atom-Photon Interaction*. Ed. by A. Predojević and M. W. Mitchell. Springer, Cham, 2015, pp. 3–38. ISBN: 978-3-319-19230-7.

[64] C. Y. Hu, A. Young, J. L. O'Brien, W. J. Munro, and J. G. Rarity. "Giant optical Faraday rotation induced by a single-electron spin in a quantum dot: Applications to entangling remote spins via a single photon". *Physical Review B* **78**, 085307 (2008).

[65] J.-H. An, M. Feng, and C. H. Oh. "Quantum-information processing with a single photon by an input-output process with respect to low-Q cavities". *Physical Review A* **79**, 032303 (2009).

[66] H. Kim, R. Bose, T. C. Shen, G. S. Solomon, and E. Waks. "A quantum logic gate between a solid-state quantum bit and a photon". *Nature Photonics* **7**, 373 (2013).

[67] A. Reiserer, S. Ritter, and G. Rempe. "Nondestructive Detection of an Optical Photon". *Science* **342**, 1349 (2013).

[68] U. Leonhardt and H. Paul. *Measuring the quantum state of light*. Vol. 19. Cambridge University Press, 1997. ISBN: 978-0-521-49730-5.

[69] R. J. Glauber. "Coherent and Incoherent States of the Radiation Field". *Physical Review* **131**, 2766 (1963).

[70] A. Reiserer, N. Kalb, G. Rempe, and S. Ritter. "A quantum gate between a flying optical photon and a single trapped atom". *Nature* **508**, 237 (2014).

[71] A. Reiserer. "A controlled phase gate between a single atom and an optical photon". Dissertation. Technische Universität München, 2014.

[72] L.-M. Duan and H. J. Kimble. "Scalable Photonic Quantum Computation through Cavity-Assisted Interactions". *Physical Review Letters* **92**, 127902 (2004).

[73] S. Nußmann. "Kühlen und Positionieren eines Atoms in einem optischen Resonator". Dissertation. Technische Universität München, 2006.

[74] B. Weber. "Transport von Atomen in einer optischen Dipolfalle". Diploma thesis. Technische Universität München, 2002.

[75] F. Rohde. "Ein optischer Resonator hoher Finesse als Atomdetektor". Diploma thesis. Technische Universität München, 2003.

[76] T. Müller. "Abbildung einzelner Atome in einem optischen Resonator höchster Finesse". Diploma thesis. Technische Universität München, 2007.

[77] A. Neuzner. "Resonance Fluorescence of an Atom Pair in an Optical Resonator". Dissertation. Technische Universität München, 2016.

[78] M. Hijlkema. "Single photons from a single atom trapped in a high-finesse optical cavity". Dissertation. Technische Universität München, 2007.

[79] B. Weber. "Distribution of quantum information between an atom and two photons". Dissertation. Technische Universität München, 2008.

[80] H. Specht. "Einzelatom-Quantenspeicher für Polarisations-Qubits". Dissertation. Technische Universität München, 2010.

[81] M. Uphoff. "State manipulation of single atoms in an optical cavity". Diploma thesis. Technische Universität München, 2010.

[82] J. Bochmann. "Coherent dynamics and state detection of single atoms in a cavity". Dissertation. Technische Universität München, 2010.

[83] C. Nölleke. "Quantum state transfer between remote single atoms". Dissertation. Technische Universität München, 2013.

[84] A. Reiserer, C. Nölleke, S. Ritter, and G. Rempe. "Ground-State Cooling of a Single Atom at the Center of an Optical Cavity". *Physical Review Letters* **110**, 223003 (2013).

[85] N. Kalb. "Heralded storage of photonic polarization in a single atom". Master's thesis. Technische Universität München, 2014.

[86] A. Shaukat. "Homodyn-Tomographie nichtklassischer Zustände optischer Pulse". Master's thesis. Ludwig Maximilians Universität München, 2016.

[87] S. Welte, B. Hacker, S. Daiss, S. Ritter, and G. Rempe. "Cavity Carving of Atomic Bell States". *Physical Review Letters* **118**, 210503 (2017).

[88] S. Welte, B. Hacker, S. Daiss, S. Ritter, and G. Rempe. "Photon-Mediated Quantum Gate between Two Neutral Atoms in an Optical Cavity". *Physical Review X* **8**, 011018 (2018).

[89] S. Welte. "Photon-Mediated Quantum Information Processing with Neutral Atoms in an Optical Cavity". Dissertation. Technische Universität München, 2019.

[90] D. A. Steck, "Rubidium 87 D Line Data". (2001).

[91] H. J. Metcalf and P. van der Straten. *Laser Cooling and Trapping*. Graduate Texts in Contemporary Physics. Springer New York, 1999. ISBN: 978-0-387-98728-6.

[92] M. Körber, O. Morin, S. Langenfeld, A. Neuzner, S. Ritter, and G. Rempe. "Decoherence-protected memory for a single-photon qubit". *Nature Photonics* **12**, 18 (2018).

[93] W. Rosenfeld, J. Volz, M. Weber, and H. Weinfurter. "Coherence of a qubit stored in Zeeman levels of a single optically trapped atom". *Physical Review A* **84**, 022343 (2011).

[94] E. D. Black. "An introduction to Pound–Drever–Hall laser frequency stabilization". *American Journal of Physics* **69**, 79 (2001).

[95] J. L. Hall, J. Ye, and L.-S. Ma. "Measurement of mirror birefringence at the sub-ppm level: Proposed application to a test of QED". *Physical Review A* **62**, 013815 (2000).

[96] B. Hacker, S. Welte, G. Rempe, and S. Ritter. "A photon-photon quantum gate based on a single atom in an optical resonator". *Nature* **536**, 193 (2016).

[97] P. Kok and B. W. Lovett. *Introduction to Optical Quantum Information Processing*. Cambridge University Press, 2010. ISBN: 978-1-139-19365-8.

[98] J. L. O'Brien, G. J. Pryde, A. G. White, T. C. Ralph, and D. Branning. "Demonstration of an all-optical quantum controlled-NOT gate". *Nature* **426**, 264 (2003).

[99] J. L. O'Brien. "Optical Quantum Computing". *Science* **318**, 1567 (2007).

[100] T. B. Pittman, M. J. Fitch, B. C. Jacobs, and J. D. Franson. "Experimental controlled-NOT logic gate for single photons in the coincidence basis". *Physical Review A* **68**, 032316 (2003).

[101] K. Sanaka, T. Jennewein, J.-W. Pan, K. Resch, and A. Zeilinger. "Experimental Nonlinear Sign Shift for Linear Optics Quantum Computation". *Physical Review Letters* **92**, 017902 (2004).

[102] S. Gasparoni, J.-W. Pan, P. Walther, T. Rudolph, and A. Zeilinger. "Realization of a Photonic Controlled-NOT Gate Sufficient for Quantum Computation". *Physical Review Letters* **93**, 020504 (2004).

[103] Z. Zhao, A.-N. Zhang, Y.-A. Chen, H. Zhang, J.-F. Du, T. Yang, and J.-W. Pan. "Experimental Demonstration of a Nondestructive Controlled-NOT Quantum Gate for Two Independent Photon Qubits". *Physical Review Letters* **94**, 030501 (2005).

[104] R. Okamoto, H. F. Hofmann, S. Takeuchi, and K. Sasaki. "Demonstration of an Optical Quantum Controlled-NOT Gate without Path Interference". *Physical Review Letters* **95**, 210506 (2005).

[105] N. K. Langford, T. J. Weinhold, R. Prevedel, K. J. Resch, et al. "Demonstration of a Simple Entangling Optical Gate and Its Use in Bell-State Analysis". *Physical Review Letters* **95**, 210504 (2005).

[106] N. Kiesel, C. Schmid, U. Weber, R. Ursin, and H. Weinfurter. "Linear Optics Controlled-Phase Gate Made Simple". *Physical Review Letters* **95**, 210505 (2005).

[107] A. V. Gorshkov, J. Otterbach, M. Fleischhauer, T. Pohl, and M. D. Lukin. "Photon-photon interactions via Rydberg blockade". *Physical Review Letters* **107**, 133602 (2011).

[108] S. Baur, D. Tiarks, G. Rempe, and S. Dürr. "Single-Photon Switch Based on Rydberg Blockade". *Physical Review Letters* **112**, 073901 (2014).

[109] D. Tiarks, S. Baur, K. Schneider, S. Dürr, and G. Rempe. "Single-photon transistor using a Förster resonance". *Physical Review Letters* **113**, 053602 (2014).

[110] H. Gorniaczyk, C. Tresp, J. Schmidt, H. Fedder, and S. Hofferberth. "Single-Photon Transistor Mediated by Interstate Rydberg Interactions". *Physical Review Letters* **113**, 053601 (2014).

[111] S. Rosenblum, O. Bechler, I. Shomroni, Y. Lovsky, G. Guendelman, and B. Dayan. "Extraction of a single photon from an optical pulse". *Nature Photonics* **10**, 19 (2016).

[112] A. Kubanek, A. Ourjoumtsev, I. Schuster, M. Koch, P. Pinkse, K. Murr, and G. Rempe. "Two-Photon Gateway in One-Atom Cavity Quantum Electrodynamics". *Physical Review Letters* **101**, 203602 (2008).

[113] I. Shomroni, S. Rosenblum, Y. Lovsky, O. Bechler, G. Guendelman, and B. Dayan. "All-optical routing of single photons by a one-atom switch controlled by a single photon". *Science* **903**, 903 (2014).

[114] Q. A. Turchette, C. J. Hood, W. Lange, H. Mabuchi, and H. J. Kimble. "Measurement of Conditional Phase Shifts for Quantum Logic". *Physical Review Letters* **75**, 4710 (1995).

[115] T. G. Tiecke, J. D. Thompson, N. P. de Leon, L. R. Liu, V. Vuletić, and M. D. Lukin. "Nanophotonic quantum phase switch with a single atom". *Nature* **508**, 241 (2014).

[116] J. Volz, M. Scheucher, C. Junge, and A. Rauschenbeutel. "Nonlinear π phase shift for single fibre-guided photons interacting with a single resonator-enhanced atom". *Nature Photonics* **8**, 965 (2014).

[117] K. M. Beck, M. Hosseini, Y. Duan, and V. Vuletić. "Large conditional single-photon cross-phase modulation". *Proceedings of the National Academy of Sciences* **113**, 9740 (2016).

[118] D. Tiarks, S. Schmidt, G. Rempe, and S. Dürr. "Optical π phase shift created with a single-photon pulse". *Science Advances* **2**, e1600036 (2016).

[119] D. Tiarks, S. Schmidt-Eberle, T. Stolz, G. Rempe, and S. Dürr. "A photon–photon quantum gate based on Rydberg interactions". *Nature Physics* **15**, 124 (2019).

[120] K. Koshino, S. Ishizaka, and Y. Nakamura. "Deterministic photon-photon SWAP gate using a Λ system". *Physical Review A* **82**, 010301 (2010).

[121] J. H. Shapiro. "Single-photon Kerr nonlinearities do not help quantum computation". *Physical Review A* **73**, 062305 (2006).

[122] J. Gea-Banacloche. "Impossibility of large phase shifts via the giant Kerr effect with single-photon wave packets". *Physical Review A* **81**, 043823 (2010).

[123] L.-M. Duan, B. Wang, and H. J. Kimble. "Robust quantum gates on neutral atoms with cavity-assisted photon scattering". *Physical Review A* **72**, 032333 (2005).

[124] A. I. Lvovsky, B. C. Sanders, and W. Tittel. "Optical quantum memory". *Nature Photonics* **3**, 706 (2009).

[125] M. Afzelius, N. Gisin, and H. de Riedmatten. "Quantum memory for photons". *Physics Today* **68**, 42 (2015).

[126] N. Kalb, A. Reiserer, S. Ritter, and G. Rempe. "Heralded Storage of a Photonic Quantum Bit in a Single Atom". *Physical Review Letters* **114**, 220501 (2015).

[127] Z. Hradil, J. Řeháček, J. Fiurášek, and M. Ježek. "Maximum-Likelihood Methods in Quantum Mechanics". In: *Quantum State Estimation*. Ed. by M. Paris and J. Řeháček. Springer Berlin Heidelberg, 2004, pp. 59–112. ISBN: 978-3-540-44481-7.

[128] R. J. Barlow. *Statistics: A Guide to the Use of Statistical Methods in the Physical Sciences*. Vol. 29. John Wiley & Sons, 1999. ISBN: 978-0-471-92295-7.

[129] C. Schwemmer, L. Knips, D. Richart, H. Weinfurter, T. Moroder, M. Kleinmann, and O. Gühne. "Systematic Errors in Current Quantum State Tomography Tools". *Physical Review Letters* **114**, 080403 (2015).

[130] G. Vidal and R. F. Werner. "Computable measure of entanglement". *Physical Review A* **65**, 032314 (2002).

[131] J. F. Poyatos, J. I. Cirac, and P. Zoller. "Complete Characterization of a Quantum Process: The Two-Bit Quantum Gate". *Physical Review Letters* **78**, 390 (1997).

[132] E. Bagan, M. Baig, and R. Muñoz-Tapia. "Minimal measurements of the gate fidelity of a qudit map". *Physical Review A* **67**, 014303 (2003).

[133] J. R. Johansson, P. D. Nation, and F. Nori. "QuTiP 2: A Python framework for the dynamics of open quantum systems". *Computer Physics Communications* **184**, 1234 (2013).

[134] H.-J. Briegel, W. Dür, J. I. Cirac, and P. Zoller. "Quantum Repeaters: The Role of Imperfect Local Operations in Quantum Communication". *Physical Review Letters* **81**, 5932 (1998).

[135] R. Raussendorf and H. J. Briegel. "A One-Way Quantum Computer". *Physical Review Letters* **86**, 5188 (2001).

[136] T. D. Ladd, F. Jelezko, R. Laflamme, Y. Nakamura, C. Monroe, and J. L. O'Brien. "Quantum computers". *Nature* **464**, 45 (2010).

[137] B. Hacker, S. Welte, S. Daiss, A. Shaukat, S. Ritter, L. Li, and G. Rempe. "Deterministic creation of entangled atom–light Schrödinger-cat states". *Nature Photonics* **13**, 110 (2019).

[138] S. L. Braunstein and P. van Loock. "Quantum information with continuous variables". *Reviews of Modern Physics* **77**, 513 (2005).

[139] E. Wigner. "On the Quantum Correction For Thermodynamic Equilibrium". *Physical Review* **40**, 749 (1932).

[140] T. Curtright, D. Fairlie, and C. Zachos. *A concise treatise on quantum mechanics in phase space*. World Scientific, 2014. ISBN: 978-981-4520-43-0.

[141] H. J. Groenewold. "On the principles of elementary quantum mechanics". *Physica* **12**, 405 (1946).

[142] R. L. Hudson. "When is the wigner quasi-probability density non-negative?" *Reports on Mathematical Physics* **6**, 249 (1974).

[143] D. Leibfried, D. M. Meekhof, B. E. King, C. Monroe, W. M. Itano, and D. J. Wineland. "Experimental Determination of the Motional Quantum State of a Trapped Atom". *Physical Review Letters* **77**, 4281 (1996).

[144] J. Li, G. Li, J.-M. Wang, S.-Y. Zhu, and T.-C. Zhang. "A comparison of two nonclassical measures, entanglement potential and the negativity of the Wigner function". *Journal of Physics B: Atomic, Molecular and Optical Physics* **43**, 085504 (2010).

[145] W. Schleich, M. Pernigo, and F. L. Kien. "Nonclassical state from two pseudoclassical states". *Physical Review A* **44**, 2172 (1991).

[146] E. Schrödinger. "Die gegenwärtige Situation in der Quantenmechanik". *Naturwissenschaften* **23**, 807 (1935).

[147] B. Yurke and D. Stoler. "Generating Quantum Mechanical Superpositions of Macroscopically Distinguishable States via Amplitude Dispersion". *Physical Review Letters* **57**, 13 (1986).

[148] C. C. Gerry and P. L. Knight. "Quantum superpositions and Schrödinger cat states in quantum optics". *American Journal of Physics* **65**, 964 (1997).

[149] C. Monroe, D. M. Meekhof, B. E. King, and D. J. Wineland. "A "Schrödinger Cat" Superposition State of an Atom". *Science* **272**, 1131 (1996).

[150] D. J. Wineland. "Nobel Lecture: Superposition, entanglement, and raising Schrödinger's cat". *Reviews of Modern Physics* **85**, 1103 (2013).

[151] D. Kienzler, C. Flühmann, V. Negnevitsky, H.-Y. Lo, M. Marinelli, D. Nadlinger, and J. P. Home. "Observation of Quantum Interference between Separated Mechanical Oscillator Wave Packets". *Physical Review Letters* **116**, 140402 (2016).

[152] M. Brune, E. Hagley, J. Dreyer, X. Maître, et al. "Observing the Progressive Decoherence of the "Meter" in a Quantum Measurement". *Physical Review Letters* **77**, 4887 (1996).

[153] S. Deléglise, I. Dotsenko, C. Sayrin, J. Bernu, M. Brune, J.-M. Raimond, and S. Haroche. "Reconstruction of non-classical cavity field states with snapshots of their decoherence". *Nature* **455**, 510 (2008).

[154] G. Kirchmair, B. Vlastakis, Z. Leghtas, S. E. Nigg, et al. "Observation of quantum state collapse and revival due to the single-photon Kerr effect". *Nature* **495**, 205 (2013).

[155] B. Vlastakis, G. Kirchmair, Z. Leghtas, S. E. Nigg, et al. "Deterministically Encoding Quantum Information Using 100-Photon Schrödinger Cat States". *Science* **342**, 607 (2013).

[156] B. Vlastakis, A. Petrenko, N. Ofek, L. Sun, et al. "Characterizing entanglement of an artificial atom and a cavity cat state with Bell's inequality". *Nature Communications* **6**, 8970 (2015).

[157] S. M. Girvin, "Schrödinger Cat States in Circuit QED". In: *Proceedings of the Les Houches Summer School*. Vol. Session CVII–Current Trends in Atomic Physics. arXiv: 1710.03179 (2017).

[158] S. Bose, K. Jacobs, and P. L. Knight. "Scheme to probe the decoherence of a macroscopic object". *Physical Review A* **59**, 3204 (1999).

[159] G. Agarwal, R. Puri, and R. Singh. "Atomic Schrödinger cat states". *Physical Review A* **56**, 2249 (1997).

[160] C. M. Savage, S. L. Braunstein, and D. F. Walls. "Macroscopic quantum superpositions by means of single-atom dispersion". *Optics Letters* **15**, 628 (1990).

[161] S. Glancy and H. M. d. Vasconcelos. "Methods for producing optical coherent state superpositions". *Journal of the Optical Society of America B* **25**, 712 (2008).

[162] M. Dakna, T. Anhut, T. Opatrný, L. Knöll, and D.-G. Welsch. "Generating Schrödinger-cat-like states by means of conditional measurements on a beam splitter". *Physical Review A* **55**, 3184 (1997).

[163] A. Ourjoumtsev. "Generating Optical Schrödinger Kittens for Quantum Information Processing". *Science* **312**, 83 (2006).

[164] A. Ourjoumtsev, H. Jeong, R. Tualle-Brouri, and P. Grangier. "Generation of optical 'Schrödinger cats' from photon number states". *Nature* **448**, 784 (2007).

[165] J. S. Neergaard-Nielsen, B. M. Nielsen, C. Hettich, K. Mølmer, and E. S. Polzik. "Generation of a Superposition of Odd Photon Number States for Quantum Information Networks". *Physical Review Letters* **97**, 083604 (2006).

[166] H. Takahashi, K. Wakui, S. Suzuki, M. Takeoka, K. Hayasaka, A. Furusawa, and M. Sasaki. "Generation of Large-Amplitude Coherent-State Superposition via Ancilla-Assisted Photon Subtraction". *Physical Review Letters* **101**, 233605 (2008).

[167] A. I. Lvovsky and M. G. Raymer. "Continuous-variable optical quantum-state tomography". *Reviews of Modern Physics* **81**, 299 (2009).

[168] N. Namekata, Y. Takahashi, G. Fujii, D. Fukuda, S. Kurimura, and S. Inoue. "Non-Gaussian operation based on photon subtraction using a photon-number-resolving detector at a telecommunications wavelength". *Nature Photonics* **4**, 655 (2010).

[169] T. Gerrits, S. Glancy, T. S. Clement, B. Calkins, et al. "Generation of optical coherent-state superpositions by number-resolved photon subtraction from the squeezed vacuum". *Physical Review A* **82**, 031802 (2010).

[170] J.-i. Yoshikawa, K. Makino, S. Kurata, P. van Loock, and A. Furusawa. "Creation, Storage, and On-Demand Release of Optical Quantum States with a Negative Wigner Function". *Physical Review X* **3**, 041028 (2013).

[171] A. Ourjoumtsev, F. Ferreyrol, R. Tualle-Brouri, and P. Grangier. "Preparation of non-local superpositions of quasi-classical light states". *Nature Physics* **5**, 189 (2009).

[172] O. Morin, K. Huang, J. Liu, H. Le Jeannic, C. Fabre, and J. Laurat. "Remote creation of hybrid entanglement between particle-like and wave-like optical qubits". *Nature Photonics* **8**, 570 (2014).

[173] H. Jeong, A. Zavatta, M. Kang, S.-W. Lee, et al. "Generation of hybrid entanglement of light". *Nature Photonics* **8**, 564 (2014).

[174] A. E. Ulanov, D. Sychev, A. A. Pushkina, I. A. Fedorov, and A. I. Lvovsky. "Quantum Teleportation Between Discrete and Continuous Encodings of an Optical Qubit". *Physical Review Letters* **118**, 160501 (2017).

[175] D. V. Sychev, V. A. Novikov, K. K. Pirov, E. S. Tiunov, C. Simon, and A. I. Lvovsky, "Entanglement of macroscopically distinct states of light". arXiv: 1811.01041 (2018).

[176] H. L. Jeannic, A. Cavaillès, J. Raskop, K. Huang, and J. Laurat. "Remote preparation of continuous-variable qubits using loss-tolerant hybrid entanglement of light". *Optica* **5**, 1012 (2018).

[177] W. Pfaff, C. J. Axline, L. D. Burkhart, U. Vool, et al. "Controlled release of multiphoton quantum states from a microwave cavity memory". *Nature Physics* **13**, 882 (2017).

[178] H. Jeong and M. S. Kim. "Efficient quantum computation using coherent states". *Physical Review A* **65**, 042305 (2002).

[179] T. C. Ralph, A. Gilchrist, G. J. Milburn, W. J. Munro, and S. Glancy. "Quantum computation with optical coherent states". *Physical Review A* **68**, 042319 (2003).

[180] A. Gilchrist, K. Nemoto, W. J. Munro, T. Ralph, S. Glancy, S. L. Braunstein, and G. Milburn. "Schrödinger cats and their power for quantum information processing". *Journal of Optics B: Quantum and Semiclassical Optics* **6**, S828 (2004).

[181] P. T. Cochrane, G. J. Milburn, and W. J. Munro. "Macroscopically distinct quantum-superposition states as a bosonic code for amplitude damping". *Physical Review A* **59**, 2631 (1999).

[182] A. P. Lund, T. C. Ralph, and H. L. Haselgrove. "Fault-Tolerant Linear Optical Quantum Computing with Small-Amplitude Coherent States". *Physical Review Letters* **100**, 030503 (2008).

[183] Z. Leghtas, G. Kirchmair, B. Vlastakis, R. J. Schoelkopf, M. H. Devoret, and M. Mirrahimi. "Hardware-Efficient Autonomous Quantum Memory Protection". *Physical Review Letters* **111**, 120501 (2013).

[184] M. Bergmann and P. van Loock. "Quantum error correction against photon loss using multicomponent cat states". *Physical Review A* **94**, 042332 (2016).

[185] N. Ofek, A. Petrenko, R. Heeres, P. Reinhold, et al. "Extending the lifetime of a quantum bit with error correction in superconducting circuits". *Nature* **536**, 441 (2016).

[186] R. W. Heeres, P. Reinhold, N. Ofek, L. Frunzio, L. Jiang, M. H. Devoret, and R. J. Schoelkopf. "Implementing a universal gate set on a logical qubit encoded in an oscillator". *Nature Communications* **8**, 94 (2017).

[187] S. Glancy, H. M. Vasconcelos, and T. C. Ralph. "Transmission of optical coherent-state qubits". *Physical Review A* **70**, 022317 (2004).

[188] P. van Loock, T. D. Ladd, K. Sanaka, F. Yamaguchi, K. Nemoto, W. J. Munro, and Y. Yamamoto. "Hybrid Quantum Repeater Using Bright Coherent Light". *Physical Review Letters* **96**, 240501 (2006).

[189] B. Wang and L.-M. Duan. "Engineering superpositions of coherent states in coherent optical pulses through cavity-assisted interaction". *Physical Review A* **72**, 022320 (2005).

[190] H. Yuen and J. Shapiro. "Optical communication with two-photon coherent states–Part III: Quantum measurements realizable with photoemissive detectors". *IEEE Transactions on Information Theory* **26**, 78 (1980).

[191] Z. Y. Ou, C. K. Hong, and L. Mandel. "Relation between input and output states for a beam splitter". *Optics Communications* **63**, 118 (1987).

[192] N. Spagnolo, C. Vitelli, T. De Angelis, F. Sciarrino, and F. De Martini. "Wigner-function theory and decoherence of the quantum-injected optical parametric amplifier". *Physical Review A* **80**, 032318 (2009).

[193] J. Appel, D. Hoffman, E. Figueroa, and A. I. Lvovsky. "Electronic noise in optical homodyne tomography". *Physical Review A* **75**, 035802 (2007).

[194] V. Bužek, A. Vidiella-Barranco, and P. L. Knight. "Superpositions of coherent states: Squeezing and dissipation". *Physical Review A* **45**, 6570 (1992).

[195] U. Leonhardt. "Quantum statistics of a lossless beam splitter: SU(2) symmetry in phase space". *Physical Review A* **48**, 3265 (1993).

[196] V. Bužek and P. L. Knight. "I: Quantum Interference, Superposition States of Light, and Nonclassical Effects". In: *Progress in Optics*. Vol. 34. Elsevier, 1995, pp. 1–158. ISBN: 978-0-444-82140-9.

[197] L. Mandel. "Sub-Poissonian photon statistics in resonance fluorescence". *Optics Letters* **4**, 205 (1979).

[198] H. Jeong, M. Kang, and H. Kwon. "Characterizations and quantifications of macroscopic quantumness and its implementations using optical fields". *Optics Communications* **337**, 12 (2015).

[199] C.-W. Lee and H. Jeong. "Quantification of Macroscopic Quantum Superpositions within Phase Space". *Physical Review Letters* **106**, 220401 (2011).

[200] J. K. Asbóth, J. Calsamiglia, and H. Ritsch. "Computable Measure of Nonclassicality for Light". *Physical Review Letters* **94**, 173602 (2005).

[201] S. J. van Enk and O. Hirota. "Entangled coherent states: Teleportation and decoherence". *Physical Review A* **64**, 022313 (2001).

[202] A. H. Kiilerich and K. Mølmer, "Input-Output Theory with Quantum Pulses". arXiv: 1902.09833 (2019).

[203] H.-A. Bachor and T. C. Ralph. *A Guide to Experiments in Quantum Optics*. Wiley, 2004. ISBN: 978-3-527-40393-6.

[204] G. L. Abbas, V. W. S. Chan, and T. K. Yee. "Local-oscillator excess-noise suppression for homodyne and heterodyne detection". *Optics Letters* **8**, 419 (1983).

[205] D. T. Smithey, M. Beck, M. G. Raymer, and A. Faridani. "Measurement of the Wigner distribution and the density matrix of a light mode using optical homodyne tomography: Application to squeezed states and the vacuum". *Physical Review Letters* **70**, 1244 (1993).

[206] U. Leonhardt and H. Paul. "Measuring the quantum state of light". *Progress in Quantum Electronics* **19**, 89 (1995).

[207] A. V. Masalov, A. Kuzhamuratov, and A. I. Lvovsky. "Noise spectra in balanced optical detectors based on transimpedance amplifiers". *Review of Scientific Instruments* **88**, 113109 (2017).

[208] O. Morin, C. Fabre, and J. Laurat. "Experimentally Accessing the Optimal Temporal Mode of Traveling Quantum Light States". *Physical Review Letters* **111**, 213602 (2013).

[209] T. M. Buzug. *Computed Tomography*. Springer Berlin Heidelberg, 2008. ISBN: 978-3-540-39407-5.

[210] F. Natterer. *The mathematics of computerized tomography*. Vol. 32. Wiley, Teubner, 1986. ISBN: 978-3-519-02103-2.

[211] A. I. Lvovsky. "Iterative maximum-likelihood reconstruction in quantum homodyne tomography". *Journal of Optics B: Quantum and Semiclassical Optics* **6**, S556 (2004).

[212] K. Banaszek, G. M. D'Ariano, M. G. A. Paris, and M. F. Sacchi. "Maximum-likelihood estimation of the density matrix". *Physical Review A* **61**, 010304 (1999).

[213] J. Řeháček, Z. Hradil, and M. Ježek. "Iterative algorithm for reconstruction of entangled states". *Physical Review A* **63**, 040303 (2001).

[214] G. M. D'Ariano, U. Leonhardt, and H. Paul. "Homodyne detection of the density matrix of the radiation field". *Physical Review A* **52**, R1801 (1995).

[215] M. Ban. "Photon statistics of conditional output states of lossless beam splitter". *Journal of Modern Optics* **43**, 1281 (1996).

[216] M. Paris and J. Řeháček, eds. *Quantum State Estimation*. Vol. 649. Lecture Notes in Physics. Springer Berlin Heidelberg, 2004. ISBN: 978-3-540-22329-0.

[217] U. L. Andersen, J. S. Neergaard-Nielsen, P. van Loock, and A. Furusawa. "Hybrid discrete- and continuous-variable quantum information". *Nature Physics* **11**, 713 (2015).

[218] J. S. Bell. "On the Einstein Podolsky Rosen paradox". *Physics* **1**, 195 (1964).

[219] S. J. Freedman and J. F. Clauser. "Experimental Test of Local Hidden-Variable Theories". *Physical Review Letters* **28**, 938 (1972).

[220] J.-Å. Larsson. "Loopholes in Bell inequality tests of local realism". *Journal of Physics A: Mathematical and Theoretical* **47**, 424003 (2014).

[221] H. Kwon and H. Jeong. "Violation of the Bell–Clauser-Horne-Shimony-Holt inequality using imperfect photodetectors with optical hybrid states". *Physical Review A* **88**, 052127 (2013).

[222] M. Araújo, M. T. Quintino, D. Cavalcanti, M. F. Santos, A. Cabello, and M. T. Cunha. "Tests of Bell inequality with arbitrarily low photodetection efficiency and homodyne measurements". *Physical Review A* **86**, 030101 (2012).

[223] C. Teo, M. Araújo, M. T. Quintino, J. Minář, et al. "Realistic loophole-free Bell test with atom–photon entanglement". *Nature Communications* **4**, 2104 (2013).

[224] M. Stobińska, H. Jeong, and T. C. Ralph. "Violation of Bell's inequality using classical measurements and nonlinear local operations". *Physical Review A* **75**, 052105 (2007).

[225] C.-Y. Park and H. Jeong. "Bell-inequality tests using asymmetric entangled coherent states in asymmetric lossy environments". *Physical Review A* **91**, 042328 (2015).

[226] D. Hunger, T. Steinmetz, Y. Colombe, C. Deutsch, T. W. Hänsch, and J. Reichel. "A fiber Fabry–Perot cavity with high finesse". *New Journal of Physics* **12**, 065038 (2010).

[227] S. Ritter, B. Hacker, S. Welte, and G. Rempe. "Recheneinheit für zwei Photonen". *Physik in unserer Zeit* **47**, 268 (2016).

[228] L. Duan. "Creating Schrödinger-cat states". *Nature Photonics* **13**, 73 (2019).

[229] P. van Loock. "Optische Katzen auf Knopfdruck". *Physik Journal* **18**, 22 (2019).

[230] J. Gallego, W. Alt, T. Macha, M. Martinez-Dorantes, D. Pandey, and D. Meschede. "Strong Purcell Effect on a Neutral Atom Trapped in an Open Fiber Cavity". *Physical Review Letters* **121**, 173603 (2018).

[231] O. Bechler, A. Borne, S. Rosenblum, G. Guendelman, et al. "A passive photon–atom qubit swap operation". *Nature Physics* **14**, 996 (2018).

[232] J. D. Thompson, T. G. Tiecke, N. P. de Leon, J. Feist, et al. "Coupling a Single Trapped Atom to a Nanoscale Optical Cavity". *Science* **340**, 1202 (2013).

[233] B. Casabone, K. Friebe, B. Brandstätter, K. Schüppert, R. Blatt, and T. E. Northup. "Enhanced Quantum Interface with Collective Ion-Cavity Coupling". *Physical Review Letters* **114**, 023602 (2015).